MOLECULAR SIMULATION OF POLYACRYLIC ACID PHASE BEHAVIOUR IN PHYSIOLOGICAL CONDITIONS AND ITS PERFORMANCE AS DOXORUBICIN CARRIER

Ph.D. THESIS

by

RATNA SANDEEP KATIYAR

DEPARTMENT OF CHEMICAL ENGINEERING
INDIAN INSTITUTE OF TECHNOLOGY ROORKEE
ROORKEE-247667 (INDIA)
JANUARY, 2019

भारतीय प्रौद्योगिकी संस्थान रुड़की
INDIAN INSTITUTE OF TECHNOLOGY ROORKEE

MOLECULAR SIMULATION OF POLYACRYLIC ACID PHASE BEHAVIOUR IN PHYSIOLOGICAL CONDITIONS AND ITS PERFORMANCE AS DOXORUBICIN CARRIER

A THESIS

Submitted in partial fulfilment of the
requirements for the award of the degree

of

DOCTOR OF PHILOSOPHY

in

CHEMICAL ENGINEERING

by

RATNA SANDEEP KATIYAR

DEPARTMENT OF CHEMICAL ENGINEERING
INDIAN INSTITUTE OF TECHNOLOGY ROORKEE
ROORKEE-247667 (INDIA)
JANUARY, 2019

©INDIAN INSTITUTE OF TECHNOLOGY ROORKEE, ROORKEE-2019
ALL RIGHTS RESERVED

INDIAN INSTITUTE OF TECHNOLOGY
ROORKEE

CANDIDATE'S DECLARATION

I hereby certify that the work which is being presented in the thesis entitled **"MOLECULAR SIMULATION OF POLYACRYLIC ACID PHASE BEHAVIOUR IN PHYSIOLOGICAL CONDITIONS AND ITS PERFORMANCE AS DOXORUBICIN CARRIER"** in partial fulfilment of the requirements for the award of the Degree of Doctor of Philosophy and submitted in the Department of Chemical Engineering of the Indian Institute of Technology Roorkee is an authentic record of my own work carried out during a period from July, 2014 to January, 2019 under the supervision of Prof. Prateek Kumar Jha, Department of Chemical Engineering, Indian Institute of Technology Roorkee.

The matter presented in the thesis has not been submitted by me for the award of any other degree of this or any other Institute.

(Ratna Sandeep Katiyar)

This is to certify that the above statement made by the candidate is correct to the best of my (our) knowledge.

(Prateek Kumar Jha)
Supervisor

The Ph.D. Viva-Voce Examination of Ratna Sandeep Katiyar, Research Scholar, has been held on ……………………..

Chairperson, SRC **Signature of External Examiner**

This is to certify that the student has made all the corrections in the thesis.

Signature of Supervisor(s) **Head of the Department**
Dated:______________

भारतीय प्रौद्योगिकी संस्थान रुड़की
INDIAN INSTITUTE OF TECHNOLOGY ROORKEE

ACKNOWLEDGEMENT

My profound appreciation goes to my mother and wife who has helped me tremendously in all my academic endeavors. I express my heartiest gratitude to my respected supervisor Prof. Prateek Kumar Jha for his guidance, wisdom, relentless help, and endless patience, and have thoroughly enjoyed research work with him throughout my PhD. I have learned a great deal from Dr. Jha, not least about the subject of my PhD, but also about research methodology, and as such I am thankful to him for raising the quality of my research and the standard of my technical writing.

I am also very thankful to Dr. Amit Kumar Dhiman and Dr. Krishnan Murugesan for their invaluable help and suggestions and for serving on the research examining committee. I am profoundly thankful to all the faculty members of the Chemical Engineering Department at IIT Roorkee, and in particular Prof. Shishir Sinha Chairperson, SRC and Head, Department of Chemical Engineering, Indian Institute of Technology, Roorkee, India who is a constant source of motivation. I would even remain thankful to all faculty members for their kind help and suggestion toward the successful completion of my PhD journey. I also like to extend my gratitude to all the other respectful faculty members of Chemical Engineering Department, IIT Roorkee, who, from behind the curtain, furnished me with their valuable assistance towards my lessons during my PhD. I wish to acknowledge all the staff of the Department of Chemical Engineering for their help and assistance during my work.

I would like to express my heartfelt thanks to all my dear lab mates Alok Ranjan, Ram Singh and Yellam Kiranmai and juniors for their moral support. I am greatly indebted to all my colleagues and friends beyond words. My sincere thanks to Mr. R. Bhatnagar for helping me during my research work.

My deepest gratitude goes also to my family for their indefatigable love and support throughout my life. To all of them I dedicate this thesis.
Thanks to **Almighty** for the beatitude throughout this journey.

(Ratna Sandeep Katiyar)

भारतीय प्रौद्योगिकी संस्थान रुड़की
INDIAN INSTITUTE OF TECHNOLOGY ROORKEE

ABSTRACT

Molecular simulations are capable tools for the design of polymeric drug carriers, as it provides a detailed molecular understanding of drug encapsulation and release in such systems. Unlike conventional pharmacokinetic modeling tools that require the experimental results to obtain model parameters, atomistic simulations only require inputs of chemical structures and therefore can minimize the need for in vitro/in vivo experimentation. The detailed molecular insight obtained by these simulations is precious and often beyond the reach of sophisticated experimental facilities. Although initially limited to the prediction of single-molecule behavior (e.g., polymer and drug orientation in a bilayer), gradual advances in computing speed and efficient simulation approaches have made it feasible to employ these methods for phenomena occurring at substantially large length and time scales (e.g., carrier-drug complexation) with modest computational cost and resources. In the present context, the design of polymeric drug carriers for controlled release, pH-responsive drug formulations require a molecular understanding of the changes in physical interactions between the excipient and drug molecules during the dissolution process inside the body. In this study, we study the molecular design of weak pH-responsive polyacrylic acid (PAA) carriers for the delivery of anticancer drug, Doxorubicin (DOX) using four sets of simulations.

In the first set of simulations, we performed MD simulations of aqueous PAA solutions. Model oligomers of PAA of different tacticities, molecular weights, degrees of deprotonation, and deprotonation patterns are simulated with water molecules. Deprotonation of PAA chains that occurs with an increase in pH results in an increase in Coulomb repulsion between chain segments on one hand, and a non-monotonic change in the hydrogen bonding between chain segments on the other hand. Therefore, at the single chain level, PAA chains are stretched at higher pH values, where the amount of stretching varies with chain tacticity and salt concentration. While the PAA chains are always more stretched for the fully deprotonated case than compared to the neutral case, radius of gyration (R_g) for a given f varies with tacticity in the order syndiotactic > atactic > isotactic. One explanation for larger stretching in the syndiotactic case compared to the isotactic case is the difference in the magnitudes of counterion condensation in the two cases. Since the fraction of condensed counterions in the isotactic case is significantly higher than that in the syndiotactic case, it would have relatively lower electrostatic repulsion between chain segments due to the charge screening effect of counterions.

For the multiple chains simulation, aggregation increases with increase in PAA concentration. Although the counterions have higher mobility than compared to PAA, they mostly reside within the PAA aggregate, thus neutralizing its overall charge. The average R_g of individual chains increases with increase in PAA concentration, implying an increase in the stretching of individual chains. Three competing changes occur with an increase in solution pH (or equivalently, an increase in f): (1) electrostatic repulsion between PAA segments increases, (2) $COOH - COOH$ hydrogen bonding decreases, and (3) $COO^- - COOH$ hydrogen bonding first increases and then decreases. Further insight into the intermolecular interactions can be obtained by a closer inspection of two nearby PAA chains in the concentrated system. The likelihood of counterion bridging increases with increasing either the concentration or the degree of deprotonation of PAA, as the fraction of condensed ions (f_c) increases both with increasing concentration and with increase in f. PAA forms aggregates at higher concentrations, which are relatively denser and contain lesser water (solid-like) at lower pH than compared to higher pH (liquid-like). Apparently, a micelle-like formation (appearance of a dense core of hydrophobic segments) is formed in the end deprotonation case due to the hydrogen bonding between the protonated ends of chains. On the other hand, a network-like formation with no such dense core appears to form in the random deprotonation case, as the protonated groups are randomly distributed along the chains.

In the second set of simulations, we simulated multiple oligomers of PAA in model gastric and intestinal fluids, where the degree of deprotonation of PAA oligomers is varied with pH of the medium. Since the gastric fluid has a pH substantially lower than intestinal fluid, PAA oligomers are relatively lesser ionized in gastric fluid in comparison to intestinal fluid and forms aggregates. The effect of pH (or f) on PAA aggregation behavior is that the compaction of PAA aggregate decreases with increase in pH.

In the third set of simulations, multiple PAA oligomers with multiple molecules of cationic anticancer drug, doxorubicin (DOX) are simulated for pH values corresponding to various physiological conditions in aqueous phase. The diffusion coefficient of DOX decreases with an increase in pH due to an increase in the ionic complexation of PAA with DOX, despite a decrease in PAA aggregation. Note that since a purely geometric criteria is used to determine "hydrogen bonding" between COO^- group of PAA and NH_3^+ groups of DOX, the extent of this "ionic complexation" may also be considered as a extent of "hydrogen bonding" between these groups.

Our observation that the DOX diffusion coefficient decreases with an increase in pH is in close agreement with the experimental studies of similar systems.

In the fourth set of simulations, we mimic the dissolution behaviour of PAA-DOX formulations in atomistic MD simulations. Sequential water removal is performed during the MD simulations, followed by re-equilibration, until an amorphous state devoid of water is achieved. This, therefore mimics the reverse of dissolution behavior of amorphous solid dispersions. We study the changes in PAA-DOX interactions and DOX diffusion coefficient as a function of water content, at pH values representative of gastric and intestinal fluids. The results of atomistic simulations can be coupled with a water uptake model to predict the drug release behavior. Diffusion coefficient of DOX decreases with increase in pH of the solution, as the hydrogen bonding between PAA (COOH and $\mathrm{COO^-}$) and DOX ($\mathrm{NH_3^+}$) increases. On removing the water between PAA and DOX, the hydrogen bonding between PAA-DOX increases and PAA-water hydrogen bonding decreases. Thus, both the solubility and diffusivity of DOX reduces. Afterward we study diffusion of DOX by changing the PAA concentration to understand erosion effect on polyacrylic acid (PAA)-doxorubicin (DOX) formulation. Then PAA observe as a fixed carrier by changing DOX concentration with fix PAA concentration with effect on diffusion of DOX. Finally, last consideration chain length variation of PAA with fix PAA and DOX concentration. Our findings are in agreement with recent experimental reports on pH-triggered targeting of tumor cells by PAA-DOX system. Using the results of these four sets of simulations, we devise molecular design principles of pH-responsive polymeric carriers.

भारतीय प्रौद्योगिकी संस्थान रुड़की
INDIAN INSTITUTE OF TECHNOLOGY ROORKEE

Publications From Dissertations

- **Refereed Journals**

1. **Ratna S. Katiyar** and Prateek K. Jha; Phase Behavior of Aqueous Polyacrylic Acid Solutions Using Atomistic Molecular Dynamics Simulations of Model Oligomers. Polymer 2017, 114, 266−276.

2. **Ratna S. Katiyar** and Prateek K. Jha; Molecular Simulations in Drug Delivery: Opportunities and Challenges. WIREs Computational Molecular Science 2018, e1358.

3. **Ratna S. Katiyar** and Prateek K. Jha; Molecular Insights into the Effects of Media−Drug and Carrier−Drug Interactions on pH-Responsive Drug Carriers. Molecular Pharmaceutics 2018, 15(6), 2479-2483.

4. **Ratna S. Katiyar** and Prateek K. Jha; Mimicking the Dissolution Mechanisms of pH-responsive Drug Release Formulations in Atomistic MD Simulations, Advanced Theory and Simulations, Accepted 2019.

- **Conferences/Workshop presentations**

1. **Ratna S. Katiyar** and Prateek K. Jha; Phase behavior of aqueous polyacrylic acid solutions using atomistic molecular dynamics simulations, Recent Trends in Chemical Sciences & Engineering (RTCSE 2017), NIT Hamirpur, October, 2017. (Best Paper Award for Oral presentation)

2. **Ratna S. Katiyar** and Prateek K. Jha; Atomistic Molecular Dynamics Simulation of pH-Responsive Polyelectrolytes, Statistical Physics of Soft Matter (SPSM), Department of Physics, Banaras Hindu University, Varanasi, November, 2015. (Poster presentation)

3. **Ratna S. Katiyar** and Prateek K. Jha; MOLECULAR SIMULATIONS OF pH-RESPONSIVE FORMULATIONS FOR ANTICANCER DRUG DELIVERY, 12th International Conference on Complex Fluids and Soft Matter (COMPFLU-2018), Department of Chemical Engineering, Indian Institute of Technology Roorkee, Roorkee 247667, India, Dec 6-9, 2018. (Poster presentation)

CONTENTS

ACKNOWLEDGEMENT

ABSTRACT

PUBLICATIONS FROM DISSERTATION

CONTENTS

LIST OF FIGURES

LIST OF TABLES

NOMENCLATURE

CHAPTER 1: INTRODUCTION

1.1. BACKGROUND AND MOTIVATION 1
1.2. OBJECTIVES 8
1.3. STRUCTURE OF THESIS 8

CHAPTER 2: LITERATURE REVIEW

2.1. BACKGROUND OF MOLECULAR SIMULATION 11
  2.1.1. MC and MD methods: State-of-the-art 14
  2.1.2. Comparison of molecular simulations with continuum approaches 16
2.2. SIMULATION SCHEME 19
  2.2.1. Difference between MC and MD methods 22
  2.2.2. System Size and Boundary Conditions 24
  2.2.3. Coarse-graining 26
  2.2.4. Free-energy calculation 28
  2.2.5. Force-fields 29
  2.2.6. Simulation software 31
2.3. APPLICATIONS IN DRUG DELIVERY 33
    2.3.1. Drug diffusion and permeation through lipid bilayer 41
    2.3.2. Drug solubility 42
    2.3.3. Carrier-drug miscibility 42
    2.3.4. Drug crystallization 43
    2.3.5. Drug loading and release 44

2.4. PERSPECTIVE 45

CHAPTER 3: PHASE BEHAVIOR OF POLYACRYLIC ACID (PAA) OLIGOMERS IN AQUEOUS SOLUTIONS

3.1. INTRODUCTION 47
3.2. SIMULATION METHODOLOGY 47
3.3. RESULTS AND DISCUSSION 49
3.3.1. Single-Chain Simulations 49
3.3.2. Multiple-Chain Simulations 53
3.4. SUMMARY 67

CHAPTER 4: THE EFFECTS OF MEDIA INTERACTIONS ON pH-RESPONSIVE DRUG CARRIERS

4.1. INTRODUCTION 69
4.2. SIMULATION METHODOLOGY 69
4.3. RESULTS AND DISCUSSION 73
4.4. SUMMARY 76

CHAPTER 5: THE EFFECTS OF MEDIA-DRUG AND CARRIER-DRUG INTERACTIONS ON pH-RESPONSIVE DRUG CARRIERS

5.1. INTRODUCTION 77
5.2. SIMULATION METHODOLOGY 77
5.3. RESULTS AND DISCUSSION 79
5.4. SUMMARY 82

CHAPTER 6: MIMICKING THE DISSOLUTION BEHAVIOR OF pH-RESPONSIVE DRUG FORMULATIONS

6.1. INTRODUCTION 83
6.2. SIMULATION METHODOLOGY 83
6.3. RESULTS AND DISCUSSION 84
6.3.1. Effect of water weight 84
6.3.2. PAA20 concentration effect on DOX 91
6.3.3. DOX concentration effect on PAA20 95
6.3.4. PAA20 chain length variations 97

6.4. SUMMARY 98

CHAPTER 7: CONCLUSIONS AND RECOMMENDATION

7.1. CONCLUSIONS 99
7.2. RECOMMENDATION 100

APPENDIX A

A.1. COMPUTATIONAL SIMULATION DETAILS 101
  A.1.1. Newton’s equation of motion 101
  A.1.2. The potential energy 101
  A.1.3. The integration algorithm 102
  A.1.4. Radius of gyration (Rg) 103
  A.1.5. Radial distribution function (RDF) 104
  A.1.6. Diffusion coefficient 104

APPENDIX B: Molecular Topology and Validation Simulations

B.1. PAA20 force-field 111
B.2. DOX force-field 115
B.3. Water (SPC216) force-field 121
B.4. Ions force-field 122
B.5. Acetate force-field 122
B.6. Acetic acid force-field 124
B.7. Maleic acid force-field 126
B.8. Oleate force-field 128
REFERENCES 133

LIST OF FIGURES

Figure 1.1 Swelling of weakly acidic pH-responsive polyelectrolytes with change in pH 3

Figure 1.2 PAA chains with same fraction of deprotonation, but different deprotonation patterns. 4

Figure 1.3 Extracellular pH differences between normal cell and cancer cell inside the human body. Bloodstream has a pH of 7.4. 6

Figure 1.4 Mimicking the dissolution behavior of pH-responsive polymer drug formulations 7

Figure 2.1 Basic steps of atomistic (MC/MD) simulations. 20

Figure 2.2 (a) and (b) shows the atomistic representation of a model polymeric drug carrier syndiotactic polyacrylic acid chain containing 20 repeat units (PAA20) and a model anti-cancer drug Doxorubicin (DOX), respectively. Here, carbon, hydrogen, oxygen, and nitrogen atoms are shown in grey, white, red, and blue colors, respectively. (c) and (d) shows initial simulation configuration of a single DOX molecule in water and a DOX molecule along with a PAA20 molecule in cubic simulation box of length 6 nm, respectively. Periodic Boundary Conditions (PBC) are used at all faces of the simulation box. (e) and (f) shows initial simulation configuration of multiple DOX molecules in water and multiple DOX molecule along with multiple PAA20 molecules, respectively. In Figure c-f, DOX, PAA20, and water molecules are shown in green, red, and cyan colors, respectively. Figure g shows a coarse-grained (CG) representation of PAA20 with the circles representing coarse-grained beads. 21

Figure 2.3 2D Representation of periodic boundary condition. The central cell (filled with yellow) represent the simulation box. Filled circles represent particles in the simulation box and open circles represent their periodic image in other cells. Bold and dashed lines shows movement of two particles near the boundary; as a particle leaves the simulation box, its image enters the box from the opposite end. 25

Figure 2.4 Thermodynamic cycle used in the calculation of binding free energy. 29

Figure 3.1 Typical single chain conformations of PAA for neutral and fully deprotonated cases for three types of tacticity: (a)-(b) isotactic, (c)-(d) syndiotactic, (e)-(f) atactic PAA chain. Carbon, oxygen, and hydrogen atoms in PAA are shown in grey, red, and white colors, respectively. Water molecules and counterions are not shown. 52

Figure 3.2 Number of oligomer-oligomer contacts with time for neutral syndiotactic PAA of concentration 3.689 M. Red dotted line indicate the convergence of oligomer-oligomer contacts around an average value. Simulation snapshots at the start of simulations (left) and after equilibration (right) are also shown. PAA chains are shown in red color; water molecules are not shown. 54

Figure 3.3 Intermolecular PAA-PAA RDF for neutral (f = 0) and fully deprotonated (f = 1) PAA of different tacticities at a concentration of 3.689 M. 55

Figure 3.4 Simulation snapshots (after equilibration) of syndiotactic PAA with f = 0.4 for different concentration with random deprotonation (Table B.4 in the Appendix B). PAA chains and counterions are shown in red and green colors, respectively; water molecules are not shown. 57

Figure 3.5 Simulation snapshots (after equilibration) for syndiotactic PAA of concentration 3.689 M for different values of f with random deprotonation (Table B.4 in the Appendix B). PAA chains and counterions are shown in red and green colors, respectively; water molecules are not shown. 59

Figure 3.6 Intermolecular PAA-PAA RDF for syndiotactic PAA of 3.689 M concentration for different values of f with random deprotonation. g(r) for small values of r are shown in the inset. 61

Figure 3.7 Zoomed view of simulation snapshot for syndiotactic PAA of 3.689 M concentration for different values of f with random deprotonation, showing the typical interactions between two nearby chains. Average distance between the center of mass of chains are 2.31 ± 0.02 nm, 2.60 ± 0.02 nm and 3.20 ± 0.01 nm for f = 0, 0.4, and 1, respectively. Carbon, oxygen, and hydrogen atoms in PAA are shown in grey, red, and white colors, respectively. Counterions are shown in green color. Water molecules are not shown. 63

Figure 3.8 Simulation snapshot of syndiotactic PAA of 3.689 M concentration for (a) random deprotonation (Table B.4 in the Appendix B) and (b) end deprotonation (Table B.5 in the Appendix B , at fixed f = 0.4, Water molecules and counterions are not shown here; aliphatic backbone carbon, COO- group, and COOH group are shown in red, blue, and green color, respectively. (c) Intermolecular PAA-PAA RDF for random (dashed line) and end deprotonation (bold line). 65

Figure 3.9 Solvent accessible surface area (SASA) divided by its value at f = 0 against f for random deprotonation and end deprotonation cases for syndiotactic PAA of 3.689 M concentration. 67

Figure 4.1 Chemical structures of compounds simulated in this study. 70

Figure 4.2 Profiles of normalized number of PAA20-PAA20 contacts against time. All the simulations details are in Table 4.1. Npp(t) is normalized by the total number of atoms of all PAA20 chains. After 50 ns of equilibration run, all of these profiles converged around average values indicated by dashed lines in the figure. 72

Figure 4.3 Simulation snapshots (after equilibration) for systems described in Table 4.1. Colour scheme: PAA20 (red), sodium ion (green), chlorine ion (white), hydroxyl ion (yellow), acetic acid (cyan), acetate (black), maleic acid (violet), oleate (magenta), and DOX (blue). Water molecules are not shown. 73

Figure 4.4 Intermolecular PAA20-simulated fluids components RDF for syndiotactic PAA20 of 0.123 M concentration of (a) $f = 0$, (b) $f = 0.05$ and (c) $f = 0.25$ with random deprotonation. 75

Figure 5.1 Profiles of normalized number of (a) PAA20-PAA20 contacts against time, and (b) PAA20-DOX contacts against time. All the simulations details are in Table 4.1. Npp(t) is normalized by the total number of atoms of all PAA20 chains. Npd(t) is normalized by the product of the number of PAA20 chains and the number of DOX molecules. After 50 ns of equilibration run, all of these profiles converged around average values indicated by dashed lines in the figure. 78

Figure 5.2 Simulation snapshots (after equilibration) for systems described in Table 4.1. Colour scheme: PAA20 (red), sodium ion (green), chlorine ion (white), and DOX (blue). Water molecules are not shown. 79

Figure 5.3 Mean square displacement (MSD) of DOX w.r.t time with different pH condition of syndiotactic PAA20 of 0.123 M concentration with random deprotonation and DOX concentration 0.384 M. The dashed lines show the fit using a straight line slope for DOX diffusion coefficient. 80

Figure 5.4 DOX diffusion coefficient decreases and PAA-DOX hydrogen bonding increases with increase in pH. See Table 5.1 for the magnitudes of diffusion coefficient and hydrogen bonding. 81

Figure 6.1 Number of PAA20-DOX contacts with time for syndiotactic random deprotonated PAA20 of 0.123 M concentration for $f = 0.60$ and DOX concentration 0.384 M with different approximated water weight percent shows in solid line. Black line indicate 80ns equilibrium run and 30 ns the production run without water removal in box. Subsequent color lines show sequential removal steps, each having a 20 ns equilibrium and 30 ns production run. Npdt is normalized by total numbers of atoms PAA20 chains. Typical simulation snapshots after equilibration are shown in the figure (a)-(c). Color scheme: PAA20 chains (red), sodium ion (green), chlorine ion (white) and DOX (blue). Water molecules are shown in purple dot point. 85

Figure 6.2 (a) Diffusion coefficient of DOX, and (b) Diffusion coefficient of water w.r.t wt. % water (w) of syndiotactic PAA20 of 0.123 M concentration $f = 0.60$ and $f = 0.05$ with random deprotonation and DOX concentration 0.384 M. Markers show the simulation results and the dashed lines show the fit using a function of the type AexpBwβ. 86

Figure 6.3 Mean square displacement (MSD) of DOX w.r.t time for syndiotactic PAA20 of 0.123 M concentration $f = 0.60$ with random deprotonation and DOX concentration 0.384 M with different approximated water weight percent shows in solid line. 87

Figure 6.4 (a) Major energy contributions (kJ/mol) of PAA20-DOX interaction, (b) $\Delta U = Uw\text{-}U(0)$ (kJ/mol) against wt. % water (w) for swellable matrix simulations. 88

Figure 6.5 Intermolecular (a) PAA20-DOX, (b) DOX-DOX RDF for $f = 0.60$ and (c) PAA20-DOX, (d) DOX-DOX RDF for $f = 0.05$ syndiotactic PAA20 of 0.123 M concentration with random deprotonation and DOX concentration of 0.384 M, with different weight percent water shown in legend. g(r) for small values of r are shown in the inset. 89

Figure 6.6 Diffusion coefficient of (a) DOX and (b) water after equilibration w.r.t different PAA20 concentration for $f = 0.05$ and $f = 0.60$ and DOX concentration 0.384 M. 92

Figure 6.7 Mean square displacement (MSD) of DOX w.r.t time for different PAA20 concentration $f = 0.60$ and DOX concentration 0.384 M. 93

Figure 6.8 Intermolecular (a) PAA20-DOX and (b) DOX-DOX RDF of different PAA20 concentration with $f = 0.60$ and DOX concentration 0.384 M. Cpg(r) for small values of r are shown in the inset. 94

Figure 6.9 Diffusion coefficient of (a) DOX and (b) water after equilibration w.r.t DOX concentration, and constant PAA20 concentration 0.123 M for $f = 0.60$ and $f = 0.05$. 96

Figure 6.10 Diffusion coefficient of DOX after equilibration w.r.t syndiotactic PAA at different length in monomers of concentration 0.123 M for $f = 0.60$ with random deprotonation and DOX concentration 0.384 M. 98

Figure A.1: Schematic illustration of the leapfrog algorithm: the coordinates r_i are calculated at every time step (bold line), velocity v_i are calculated at half time steps (dashed line). 103

Figure A.2: Radius of gyration Rg and center of mass r_G in a bead spring model 104

Figure B.1 Comparison of the Rg values against degree of deprotonation for three chains with different random deprotonation (Table B.1, B.2 and B.3) and their average values. 110

Figure B.2 Typical chain conformations of PAA at various degrees of deprotonation. Water molecules and counter ion are not shown here; aliphatic backbone carbon gray, hydrogen white, oxygen red color atoms are shown 110

Figure B.3 Protonated (left) and deprotonated (right) repeating units in PAA20 with atom types shown in red color 111

Figure B.4 Structure of cationic anticancer drug doxorubicin (DOX) with atom types shown in red color 115

भारतीय प्रौद्योगिकी संस्थान रुड़की
INDIAN INSTITUTE OF TECHNOLOGY ROORKEE

LIST OF TABLES

Table 2.1 List of molecular simulation methods commonly employed in drug delivery 13

Table 2.2 Comparison of Molecular Simulation Methods with Continuum Methods 17

Table 2.3 List of commonly used force fields 31

Table 2.4 List of commonly used molecular simulation softwares 32

Table 2.5 Representative studies using molecular simulations in drug delivery 34

Table 3.1 Comparison of Rg values of neutral ($f = 0$) and fully deprotonated states ($f = 1$) of single PAA chain of different tacticity. Fraction of "condensed" counterions (fc) is also shown for the $f = 1$ case. The values in brackets are the standard deviation of the last decimal. 53

Table 3.2 Radius of gyration (for single chain and all chains), SASA/monomer, and fraction of condensed ions, of syndiotactic PAA with $f = 0.4$ for different concentration with random deprotonation (Table B.4 in the Appendix B). The values in brackets are the standard deviation of the last decimal. 58

Table 3.3 Radius of gyration (for single chain and all chains), SASA/monomer, and fraction of condensed ions, of syndiotactic PAA at different degrees of deprotonation with random deprotonation (Table B.4 in the Appendix B). The values in brackets are the standard deviation of the last decimal. 60

Table 3.4 Hydrogen bonding per monomer for syndiotactic PAA of different concentration for different f with random deprotonation. The values in brackets are the standard deviation of the last decimal. Values < 0.01 are not reported, since the standard deviation becomes comparable or higher than the mean. 62

Table 3.5 Radius of gyration (for single chain and all chains), SASA/monomer (hydrophobic, hydrophilic, and total), and fraction of condensed ions, of syndiotactic PAA at different degrees of deprotonation with end deprotonation (Table B.5 in the Appendix B). The values in brackets are the standard deviation of the last decimal. 66

Table 4.1 Systems simulated in this study. The composition of FaSSGF, FeSSGF, and FeSSIF are taken from literature (Marques et al. 2011) and components with less than 10 molecules in the simulation box size (10 nm) are not included, since statistical averaging over very few molecules of a component in the simulation box is not likely to provide reliable statistics. 71

Table 4.2 Radius of gyration for all chains, SASA/monomer and hydrogen bonding per monomer of syndiotactic PAA20 at different degrees of deprotonation with random deprotonation. The values in brackets are the standard deviation of the last decimal. 74
Table 5.1 Simulation results for set 2 described in Table 4.1. The values in brackets indicate the standard deviation of the last digit in decimals, e.g., 3.04(4) is equivalent to 3.04 ± 0.04. The last row represents the diffusion coefficient of DOX in the system containing no PAA. 82
Table 6.1 Hydrogen bonding syndiotactic PAA20 concentration 0.123 M for $f = 0.60$ and $f = 0.05$ with random deprotonation and DOX concentration 0.384 M with different weight % water. The values in brackets indicate the standard deviation of the last digit in decimals, e.g., 0.79(4) is equivalent to 0.79 ± 0.04. 90
Table 6.2 Hydrogen bonding different PAA20 concentration with $f = 0.60$ and $f = 0.05$ and DOX concentration 0.384 M. The values in brackets are the standard deviation of the last decimal. 95
Table 6.3 Hydrogen bonding different concentration of DOX, and constant syndiotactic PAA20 concentration 0.123 M for $f = 0.60$ and $f = 0.05$. The values in brackets indicate the standard deviation of the last digit in decimals, e.g., 5.2(3) is equivalent to 5.2 ± 0.3. 97
Table B.1 20 monomer atactic PAA chain with random deprotonation, chain 1 105
Table B.2 20 monomer atactic PAA chain with random deprotonation, chain 2 106
Table B.3 20 monomer atactic PAA chain with random deprotonation, chain 3 107
Table B.4 20 monomer syndiotactic PAA chain with random deprotonation 108
Table B.5 20 monomer syndiotactic PAA chain with end deprotonation 109
Table B.6 Atom types in PAA20 111
Table B.7 Pair types for intramolecular 1-4 interactions in PAA20 112
Table B.8 Bond Energy Parameter for PAA20 112
Table B.9 Angle Energy Parameters for PAA20 113
Table B.10 Proper dihedral energy parameters for PAA20 113
Table B.11 Improper dihedral energy parameters for PAA20 114
Table B.12 Atom types for DOX 115
Table B.13 Pair types for intramolecular 1-4 interactions in DOX 116
Table B.14 Bond energy parameters for DOX 117

Table B.15 Angle energy parameters for DOX 117
Table B.16 Proper dihedral energy parameters for DOX 118
Table B.17 Improper dihedral energy parameters for DOX 121
Table B.18 Atom types for water 121
Table B.19 Bond energy parameters for water 121
Table B.20 Angle energy parameters for water 122
Table B.21 Atom types of ions 122
Table B.22 Atom Types in acetate 122
Table B.23 Pair types for intramolecular 1-4 interactions in acetate 122
Table B.24 Bond Energy Parameter for acetate 123
Table B.25 Angle Energy Parameters for acetate 123
Table B.26 Proper dihedral energy parameters for acetate 123
Table B. 27 Improper dihedral energy parameters for acetate 123
Table B.28 Atom Types in acetic acid 124
Table B.29 Pair types for intramolecular 1-4 interactions in acetic acid 124
Table B.30 Bond Energy Parameter for acetic acid 124
Table B.31 Angle Energy Parameters for acetic acid 125
Table B.32 Proper dihedral energy parameters for acetic acid 125
Table B.33 Improper dihedral energy parameters for acetic acid 126
Table B.34 Atom Types in maleic acid 126
Table B.35 Pair types for intramolecular 1-4 interactions in maleic acid 126
Table B.36 Bond Energy Parameter for maleic acid 126
Table B.37 Angle Energy Parameters for maleic acid 127
Table B.38 Proper dihedral energy parameters for maleic acid 127
Table B.39 Improper dihedral energy parameters for maleic acid 128
Table B.40 Atom Types in oleate 128
Table B.41 Pair types for intramolecular 1-4 interactions in oleate 128
Table B.42 Bond Energy Parameter for oleate 129
Table B.43 Angle Energy Parameters for oleate 129
Table B.44 Proper dihedral energy parameters for oleate 130
Table B. 45 Improper dihedral energy parameters for oleate 131

भारतीय प्रौद्योगिकी संस्थान रुड़की
INDIAN INSTITUTE OF TECHNOLOGY ROORKEE

NOMENCLATURE

f	Degree of deprotonation
f_c	Fraction of "condensed" counterions
pKa	Negative logarithm (base 10) of the acid dissociation constant
K_a	Acid dissociation constant
N	Atoms
V	Volume
T	Temperature
P	Pressure
s	second
k_b	Boltzmann constant
ΔA	Free energy change
g	gram
cc	centimetre^3
m	meter
N_{ij}	Number of contacts between pairs of species normalized by number of atoms of one species
r	Radial distance
kJ	Kilojoule
K	Kelvin
D	Diffusion coefficient (cm^2/s)
R_g	Radius of gyration (nm)
ΔE	Energy change
$\langle r^2 \rangle$	Mean square displacement
t	Time (ns)

$\vec{F_i}(t)$	Force acting on i^{th} particle at time t
m_i	The mass of i^{th} particle
$\vec{r_i}$	The coordinates of i^{th} particle
b_i	Bond distance
q_i, q_j	Partial charge
$\vec{a}_i$	Acceleration of i^{th} particle
$\vec{v}_i$	Velocity of the i^{th} particle
r_G	Center of mass
$g(r)$	Radial distribution function (RDF)
r_{ij}	Distance between pairs

Greek letters

λ	Coupling variable
ρ	Density
ϵ_{ij}	Energy well depth
δr	Bin width
ε_0	Vacuum permittivity
θ_i	Angle
ϕ_i	Dihedral angle
δ_i	Phase shifts
φ_i	Out-of-plane angle

Subscripts

p	PAA oligomer
d	Doxorubicin
i, j	General index
c	“condensed” counterions

CHAPTER 1

INTRODUCTION

BACKGROUND AND MOTIVATION

According to the IUPAC definition, polyelectrolyte is a “polymer composed of macromolecules in which a substantial portion of the constitutional units contains ionic or ionisable groups, or both”(Nič et al. 2009). Depending on the strength of the ionisable group, they can be classified as strong or weak. Strong polyelectrolytes contain strong acidic/basic groups (e.g. sulfonate, hydroxyl, etc.) that remain ionised at all practical pH conditions. On the other hand, weak polyelectrolytes contain weak acidic/basic groups (e.g., carboxyl, amide, etc.) that undergo a transition from a neutral state to a charged state with change in pH (Figure 1.1). This transition from neutral to charged state occurs due to deprotonation of acidic groups with an increase in pH or protonation of basic groups with a decrease in pH. In general, polyelectrolytes have better aqueous solubility than neutral polymers. Moreover, they exhibit interesting self-assembly behavior driven by electrostatic forces(Cohen Stuart et al. 2005; Dobrynin 2008). For example, oppositely charged polyelectrolytes self-assemble to form polyelectrolyte complexes, which can either be solid-like (precipitate) or a liquid/gel-like (coacervate(Radhakrishna et al. 2017)) depending on the pH and ionic strength (salt concentration) of the medium(Gucht et al. 2011; Jha et al. 2014; Kizilay, Kayitmazer, and Dubin 2011; Kudlay, Ermoshkin, and De La Cruz 2004; Priftis and Tirrell 2012). Similar self-assembly behavior can also be observed in systems containing identical polyelectrolytes, by either varying the degree of ionization by changing pH(de la Cruz et al. 1995; Morrow, Payne, and Shen 2015) or screening the Coulomb repulsion between the chains by increasing salt concentration(Kudlay and de la Cruz 2004; Kundagrami and Muthukumar 2008). Such self-assembly behavior of polyelectrolytes finds use in a range of applications; some recent areas of applications include fuel cell technology(Guo et al. 2002; Sachan et al. 2014), drug delivery(Nie et al. 2014; Peyratout and Dahne 2004; Schmaljohann 2006), tissue engineering(Almeida, Amaral, and Lobão 2012; Coimbra et al. 2011), and optoelectronic devices(Hoven et al. 2008).

Physical properties of polyelectrolytes are fundamentally interesting and have intrigued scientists working in the area of biology and soft matter from last several decades(Dobrynin 2008; Dobrynin and Rubinstein 2005; Holm et al. 2004). At the single chain level (dilute concentrations), polyelectrolyte chains are stretched and have high persistence length due to

Coulomb repulsion between chain segments. For charge densities beyond a threshold value or for the case of multivalent salts, counterions condense on the polyelectrolyte backbone (Manning condensation(Gerald S. Manning 1969)), resulting in chain collapse. Concentrated solutions of polyelectrolytes possess strong ion-ion correlations resulting in the formation of strongly segregated structures(Sing, Zwanikken, and Olvera de la Cruz 2013a, 2013b). These behaviors have been captured in field-theoretical studies(Muthukumar 2004; Wang, Taniguchi, and Fredrickson 2004) and coarse-grained simulations(Alarcón et al. 2013; Liu and Muthukumar 2002), which however have mainly focused on strong polyelectrolytes. Such studies of pH-responsive, weak polyelectrolytes are relatively few(Berghold, van der Schoot, and Seidel 1997; Laguecir et al. 2006). Although the field-theoretical and coarse-grained simulation approaches succeed in achieving a qualitative understanding of polyelectrolyte behavior, they do not adequately account for the chemical details of polyelectrolytes and thus do not provide a molecular-level insight of the underlying physics. In particular, physical interactions that vary strongly with the polymer chemistry (e.g., hydrogen-bonding) are only captured at a rudimentary level and often requires a priori knowledge about the magnitudes of such interactions. Atomistic simulations, on the other hand, include the necessary chemical details and thus capture such interactions in a predictive manner, that is, without a prior knowledge about these interactions. Despite this obvious advantage, studies of polyelectrolyte systems using atomistic simulations are relatively scarce, mainly because of the computational expense of these simulations. While atomistic simulations of realistic large molecular weight polymers remains impossible, simulations of reasonably long oligomers that mimic the behavior of real polymers are only now becoming feasible(Chockalingam and Natarajan 2015; Jha and Larson 2014; Liu et al. 2009; Min, Kwak, and Kim 2015). Atomistic simulations of long oligomers coupled with systematic coarse-graining approaches(Hsu et al. 2014; Huang et al. 2016a; Reith et al. 2002) now provide a pathway to study polyelectrolyte systems at atomic resolution, and is being actively pursued.

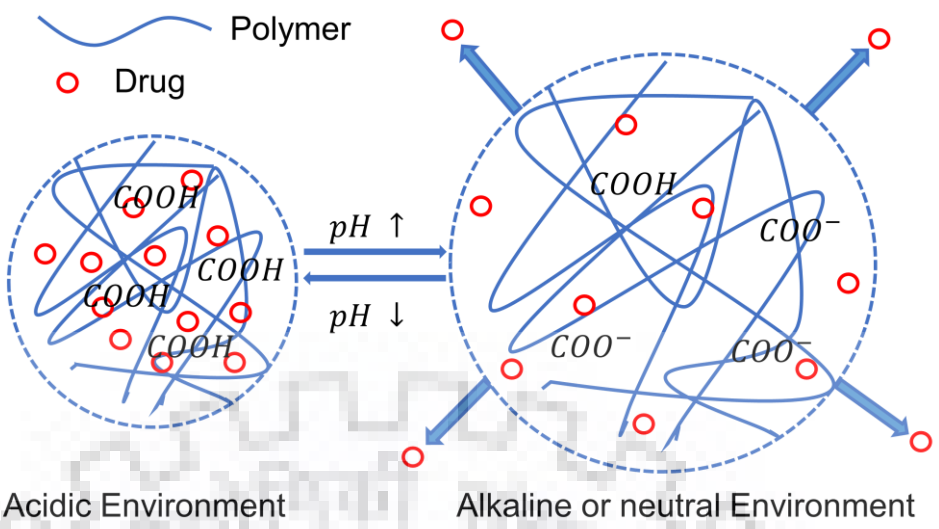

Figure 1.1 Swelling of weakly acidic pH-responsive polyelectrolytes with change in pH

The degree of deprotonation of polyelectrolytes at a given pH can be obtained using the Henderson-Hasselbalch equation(Atkins and De Paula 2011), that is, in the case of polyacids,

$$f = \frac{1}{1+10^{pKa-pH}} \tag{1.1}$$

Here, f is the fraction of deprotonated groups (degree of deprotonation) and pKa is the negative logarithm (base 10) of the acid dissociation constant, K_a. There are two major issues in the use of this equation for polyelectrolytes. First, the pKa values of polyelectrolyte solutions are a function of the polyelectrolyte molecular weight and salt concentration(Jha et al. 2014) and are generally not available. Second, the Henderson-Hasselbalch equation can only provide the average fraction of charged groups and provide no information on the actual positions of these charged groups on the polyelectrolyte chain, which further keep changing due to dynamic nature of protonation-deprotonation equilibrium. This is demonstrated in Figure 1.2, where the two PAA chains have the same deprotonation fraction but different deprotonation patterns. COO^- groups are closer to each other in Figure 1.2b compared to Figure 1.2a, which results in relatively larger intra-chain electrostatic repulsion. Therefore, the structure and properties of these two PAA chain conformations, both of which can be obtained at the same pH, may be strikingly different. Further, the Henderson-Hasselbalch equation provide no clue about which of these conformations would be more likely. It ignores the fact that the deprotonation free energy of a $COOH$ group is generally expected to be larger if a COO^- group is present on the neighbouring monomer(s), since the deprotonation would lead to high electrostatic repulsion. Thus, we need to resort to molecular simulations that provide detailed insights into the effect of pH on the polyelectrolyte behaviour. Yet another advantage of molecular simulations is their predictive nature; simulations can be performed to study behaviour of novel molecules that have not been synthesized to access their potential for a given application.(Jha and Larson 2014) This can save experimental effort and expense, while screening molecules for different applications.

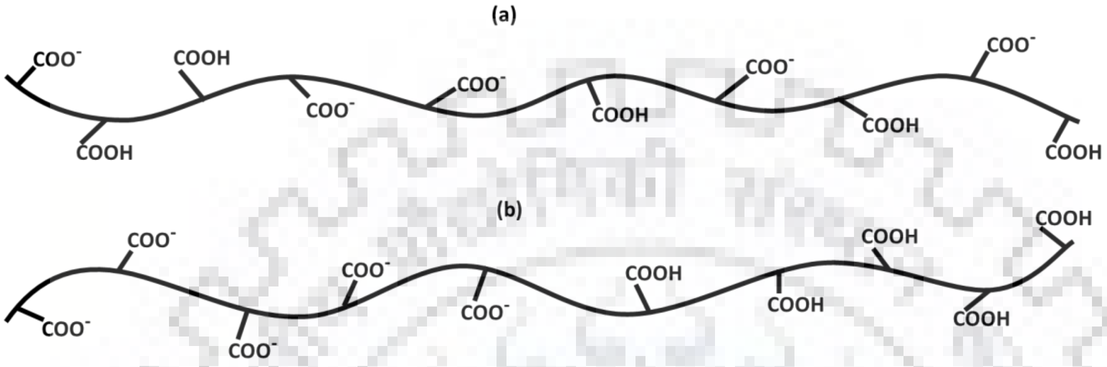

Figure 1.2 PAA chains with same fraction of deprotonation, but different deprotonation patterns.

Two distinct approaches can be used in the atomistic simulations of weak polyelectrolytes. First is the conventional molecular dynamics (MD) simulations performed in the canonical (NVT) ensemble or isothermal-isobaric (NPT) ensemble simulations of polyelectrolytes, performed for different degrees of deprotonation and deprotonation patterns(Chockalingam and Natarajan 2015; Hoda and Larson 2009), which include the pH-induced changes in the average deprotonation but do not account for the dynamic nature of protonation-deprotonation equilibrium. Second is the constant-pH molecular dynamics approaches(Börjesson and Hünenberger 2001; Donnini et al. 2011) that have originally been developed for proteins and can be extended for simulations of weak polyelectrolytes as done in a recent study(Morrow et al. 2015). Constant-pH simulations also accounts for the dynamic protonation-deprotonation processes and therefore can predict the pKa values and the titration curve of polyelectrolytes. However, there are several issues in the practical implementation of these methods. For instance, the use of an artificial barrier potential, a reference “chemically similar” compound, incorporation of explicit titratable water, and presence of multiple titration sites on a molecule remains problematic from a fundamental standpoint and computationally difficult.(Donnini et al. 2011) More importantly, such methods should be adequately able to sample 2^M possible deprotonation patterns for a polyelectrolyte chain containing M ionisable groups, which results in a very large number of possible conformations in a solution of polyelectrolytes. We therefore adopt the first approach and vary both the degree of deprotonation and deprotonation patterns to understand the effect of these on the phase behaviour. We expect that the main conclusions of our study will be the same for constant-pH simulations, provided they are able to adequately sample all possible conformations. However, the effects of dynamic changes in the deprotonation patterns are not captured in our study.

Weakly charged polyelectrolytes have tremendous potential as stimuli-responsive drug carriers, as they can benefit from intrinsic pH differences present inside the body (Kocak, Tuncer, and Bütün 2017; Manallack et al. 2013; Mura, Nicolas, and Couvreur 2013; Schmaljohann 2006). In the context of oral drug delivery, they are useful for the delivery of poorly soluble drugs that tend to aggregate in the stomach, thus resulting in low intestinal absorption and bioavailability. In an ideal situation, drug molecules should be physically entrapped in the carrier in the acidic gastric environment with limited or no aggregation, and released as free molecules in the basic intestinal environment. The pH gradient is reversed in the context of intravenous drug delivery, i.e., drugs need to be released at lower extracellular pH conditions of affected tissues and entrapped by the carrier in the relatively higher pH of the bloodstream (Kanamala et al. 2016) (Figure 1.3). Apart from the requirement that the carrier should rapidly respond to the physiological pH gradient, several other factors such as the role played by various components of physiologically relevant media (e.g., gastric and intestinal fluids for oral delivery), drug chemistry, drug-carrier interactions, and carrier biodegradability must also be considered during carrier design. However, with an exception of carrier biodegradability, a thorough molecular understanding of all these factors is seldom sought and a trial-and-error approach is usually employed to find the best carrier for a given drug. Molecular simulations can fill this gap by providing a detailed molecular insight into the carrier/drug response to pH, media-carrier and drug-carrier interactions, and their effects on drug release. This approach has been followed in some of the recent studies to understand the effects of pH on polymer aggregation, effects of bile salts on digestion (Birru, Warren, Han, et al. 2017; Birru, Warren, Headey, et al. 2017), and drug release through concentrated polymer solutions(Goel et al. 2008) and gels (Jha and Larson 2014).

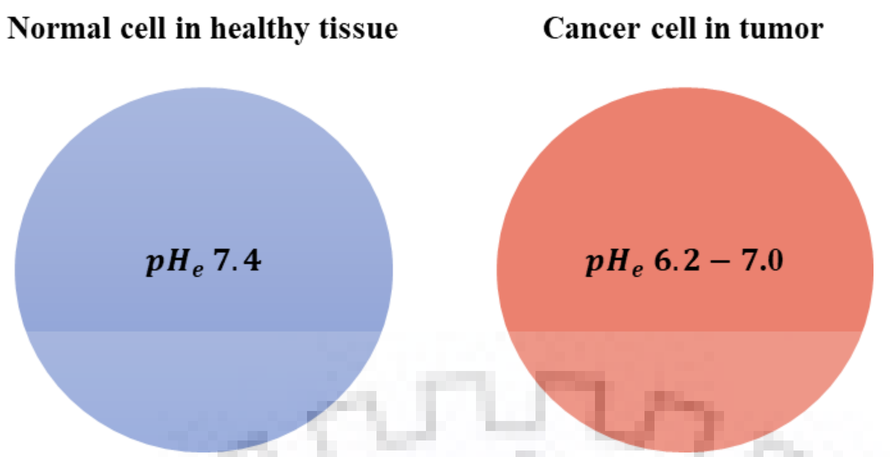

Figure 1.3 Extracellular pH differences between normal cell and cancer cell inside the human body. Bloodstream has a pH of 7.4.

Polymer-drug formulations(Zhang et al. 2008) are one of the most common and effective controlled release technologies available today(Uhrich et al. 1999). Polymer chemistries provide an extensive design space not only in terms of monomer combinations (block copolymers(Kataoka, Harada, and Nagasaki 2012)) or crosslinking (Figure 1.4) (hydrogels(Hoare and Kohane 2008)), but also in terms of possible functionalization, novel polymer architectures(Hsiao, Schroeder, and Sing 2016; Qiu and Bae 2006) (e.g., dendrimers(Maiti et al. 2009)), and polymer tethering/grafting to nanoparticles(Patra and Singh 2013), etc. Moreover, the stimuli-responsive nature of polymers has been explored in vastly different contexts, including both the intrinsic (pH(Almeida et al. 2012), enzymes, etc.) and extrinsic (heat, light, etc.(Schmaljohann 2006)) stimuli. Not surprisingly, exponentially increasing reports on synthesis of novel polymeric excipients and their proof-of-concept studies are being published every year(Jha and Larson 2014). This has however raised an additional burden of optimizing such excipients for performance by exploring their design space. Since the experimental synthesis of large number of chemistries is a costly affair, such optimization should preferably be carried using a virtual (computational) screening as typically used in drug design. However, unlike computational drug design where the main focus is on drug-receptor interaction(Liu et al. 2018), excipient design should involve thorough study of the entire lifecycle of the formulation inside the body. For instance, in the case of oral drug delivery, one needs to know the possible interactions of the excipient with gastric and intestinal fluids and also the changes in excipient-drug interactions with changes in environmental conditions in the gastrointestinal (GI) tract, both of which are expected to affect the eventual drug release(Bag and Rao 2006; Hoffman 2013).

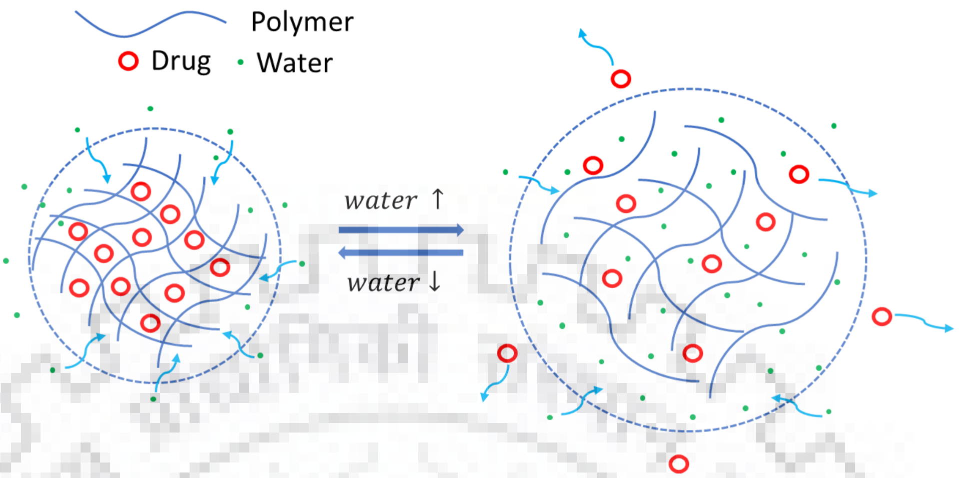

Figure 1.4 Mimicking the dissolution behavior of pH-responsive polymer drug formulations

Conventional pharmacokinetic models (e.g., compartment models) approach the excipient design problem as the analysis of diffusive and non-diffusive transport of drug molecules from a swelling/eroding/degrading matrix comprised of excipient and drug molecules. These models, in combination with dissolution experiments, do provide reliable model parameters by 'fitting' the experimental data of specific systems. Thus, though they succeed in explaining the experimental results or an approximate extrapolation of findings to longer times, they have limited applicability for other chemistries. An upcoming but relatively immature approach is the use of atomistic simulations, which though limited in the capability to simulate realistic length and time scales, are able to predict behavior of systems prior-to-synthesis. Apart from the possibility of deriving model parameters for pharmacokinetic studies, their strength lies in their ability to decipher the molecular details of excipient-drug interactions and how they change during the lifecycle of excipient-drug formulation inside the human body. Recent studies have used molecular simulations to rank the performance of excipients, analyze the effects of gastric/intestinal media, and understanding the physical changes in the formulation in response to an intrinsic/extrinsic stimulus.

Depending on the application (oral or intravenous) and the type of drug to be released, pH-response can be incorporated in the carriers in a variety of ways. For neutral drugs without significant carrier-drug interactions, cationic (anionic) carrier would dissolve/swell due to electrostatic repulsion between chain segments at lower (higher) pH when it is protonated (deprotonated), resulting in release of drug molecules. The situation is complicated when the drug molecules are also charged or possess other significant carrier-drug interactions. In such cases, it is important to observe how the carrier-drug interactions vary with pH. In this study, we have chosen a cationic anticancer drug, doxorubicin (DOX), with an anionic carrier, polyacrylic acid (PAA), where the degree of deprotonation of PAA varies with pH. An increase in pH in this case not only increases the effective negative charge on PAA but also changes the PAA-DOX complexation and intermolecular hydrogen bonding. The detailed analysis of such changes and their effect on the drug release behaviour is the ultimate goal of our study. Before proceeding to the case including drug molecules, we first analyse the detailed phase behaviour of PAA in physiological fluids.

OBJECTIVES

- To study the phase behavior of polyacrylic acid (PAA) solutions using atomistic molecular dynamics simulations of model oligomers in different physiological pH conditions (water, gastric/intestinal fluids).
- To understand cationic anticancer drug, doxorubicin (DOX) release from PAA in different physiological pH conditions
- To mimic dissolution behaviour of poly(acrylic acid) (PAA)-doxorubicin (DOX) formulation in water by atomistic MD simulations

STRUCTURE OF THESIS

This thesis has been organised in seven chapters summarized as follows:

Chapter 1: In this chapter, I present the background and motivation for my research on pH-responsive polymeric carriers on drug delivery. Objectives of my research on molecular simulations of polymeric carrier are outlined.

Chapter 2: In this chapter, I review the relevant literature for opportunities and challenges in drug delivery by molecular simulations. I discuss the molecular simulation methods and their applications in the context of drug delivery.

Chapter 3: In this chapter, I discuss the study of the solvation and aggregation behaviour of a weak pH-responsive polyelectrolyte, poly(acrylic acid) (PAA), in dilute aqueous solution.

Chapter 4: In this chapter, I describe the simulations of PAA in model gastric and intestinal fluids.

Chapter 5: In this chapter, I present the simulations of PAA with the anticancer drug, doxorubicin for a range of pH values representative of various physiological conditions.

Chapter 6: In this chapter, I discuss our attempts on mimicking the dissolution behavior of PAA-DOX formulations in water, as function of pH, PAA and DOX concentration, and PAA chain length.

Chapter 7: In this chapter, I discuss the conclusion of the present work along with the possible impact and future areas of work.

भारतीय प्रौद्योगिकी संस्थान रुड़की
INDIAN INSTITUTE OF TECHNOLOGY ROORKEE

CHAPTER 2

LITERATURE REVIEW

2.1. BACKGROUND OF MOLECULAR SIMULATION

“Simulation”, as defined by Oxford Dictionary, is the “imitation of a situation or process”, or “the action of pretending; deception”, or “the production of a computer model of something, especially for the purpose of study”. Indeed, computer simulations have been highly successful in imitating reality, and have served as great tools to understand complex systems and to test hypotheses, especially in cases where experiments are impossible, expensive, or unsafe. However, the beautifully animated movies of the simulation output also adds a sense of illusion, as they often provide much more information than that can be verified by experiments. This is particularly true for the simulations of nanoscale systems(Ayappa et al. 2007), where highly sophisticated microscopy techniques can only partially capture the structural and dynamical information, which are routinely obtained in a molecular simulation. Nevertheless, the fact that an increasingly larger number of findings of computer simulations of the past are being confirmed by latest experiments have increased our confidence in computer simulations(Dror et al. 2012; Tildesley 1995). In the last couple of decades, we have witnessed a paradigm shift in the use of computer simulations, moving from the understanding of complex processes to the computational (in silico) design of materials(Ganesan, Coote, and Barakat 2017; Gubbins and Moore 2010), e.g., computational screening of materials for a desired application by prediction of material properties of candidate materials prior to synthesis.

“Molecular simulation” or “Molecular modeling” is a general term that encompasses all theoretical and computational methods (Table 2.1) to study the behavior of a molecule or a system of molecules. (Leach 2001) Naively speaking, the behavior of a molecule corresponds to the behavior of its atoms, which in turn corresponds to the behavior of its atomic constituents. With this perspective, we should resort to quantum-mechanical (QM) methods that essentially solve the Schrödinger equation for a reliable description of molecular behavior. It turns out however that QM methods are computationally intensive and often unnecessary for determining the properties of interest in complex molecular systems. Specifically, for most properties of practical interest with a notable exception of chemical reactivity, it is possible to resort to a simplified, classical “atomistic” description where the motion of atoms are approximated by the motion of their nuclei, which are assumed to be classical particles obeying Newtonian mechanics.

This is the theoretical basis of atomistic Molecular Dynamics (MD) method, where the atoms of molecules are the fundamental entities that move due to interatomic forces (referred as the “force field”) applied by the atoms of the same molecule or other molecules in the system. The Atomistic Monte Carlo (MC) method also employs above approximation and uses the notion of force-field, but is methodically different from the MD method. MC simulation samples the configurations of a system of molecules according to the probability of finding those configurations(Fredrickson, Ganesan, and Drolet 2002), given by their Boltzmann weights. The consecutive configurations are obtained using smart trial moves (steps) comprised by random displacements of atom(s), which are accepted/rejected with a probability dependent on the global energy change due to the trial move. Unlike MD that numerically integrates equation of motion using small timesteps, MC simulations lack a definition of time and configurations sampled in an MC simulation do not represent the true trajectory of atoms. Nevertheless, both MC and MD methods provide similar results for prediction of certain equilibrium properties (e.g., pair distribution functions), provided they are run long enough.

For the sake of convenience, we will discuss the common features and applications of both MC and MD simulations by referring them as MC/MD simulations, but the readers must note that the underlying methods are essentially different. In particular, the step size in an MC simulation and timestep in an MD simulation have different meaning, but the computation time shows similar scaling with both the number of timesteps in MD simulations and the number of steps in MC simulations, for a given system size. Specifically, all physical time scales (in ns) mentioned in the thesis refer to MD simulations. Otherwise, the simulated time refers to the number of timesteps in MD simulations and number of steps in MC simulations. Advantages and disadvantages of MC and MD simulations will be compared in a separate section. It is important to point out that the MD simulations have so far been more commonly used for problems in drug delivery when compared to MC simulations. We therefore place more emphasis on MD simulations and do not elaborate on some of the recent advancements in MC simulations that are yet not employed in drug delivery problems.

Table 2.1 List of molecular simulation methods commonly employed in drug delivery

Simulation Method	**Variants**	**Applications**
Quantum-Mechanical (QM) methods(Merz 2015; Mucs and Bryce 2013; Raha et al. 2007)	Density functional theory (DFT), Hartree-Fock (HF) theory, Semi-empirical and QM/MM methods	Potential energy, geometry optimization, docking, force-field parameterization
Monte Carlo (MC)	Atomistic Monte Carlo(Bernini et al. 2014; Meunier, Goupil, and Lienard 2017)	Free energy, Absorption/binding energy, docking
	Coarse-Grained Monte Carlo(Pogodin et al. 2012; Yan and de Pablo 2003)	Self-assembly, Swelling of gel carriers, Membrane translocation
	Lattice Monte Carlo, Kinetic Monte Carlo (kMC)(Martínez et al. 2009; Vlugt-Wensink et al. 2006; Zeng, Jacob, and Tikare 2004)	Drug release from excipient matrices, Crystallization
Molecular Dynamics (MD)	Atomistic Molecular Dynamics(De Vivo et al. 2016; Zhao and Caflisch 2015)	Solubility, hydrogen bonding, diffusivity, Membrane permeability, Carrier-drug miscibility, Carrier-drug interaction, Glass transition, Drug aggregation and crystallization

	Coarse-grained Molecular Dynamics(Prates Ramalho, Gkeka, and Sarkisov 2011; Thota, Hu, and Jiang 2015), Brownian Dynamics (BD)(Chen et al. 2009), Dissipative Particle Dynamics (DPD)(Guo et al. 2010)	Self-assembly, Drug release from excipient matrices, Membrane translocation

2.1.1. MC and MD methods: State-of-the-art

The development of MC and MD methods were closely aligned with the development of early computers in the mid-twentieth century. However, early use of these methods were limited to toy-models such as the “hard sphere” model to simulate perfectly elastic collisions, or spheres interacting with a Lennard-Jones potential used to model the behavior of liquid Argon(Gubbins and Moore 2010; Tildesley 1995). With an exponential rise in computational power and development of efficient computational schemes, application of these methods to more sophisticated atomic models of complex molecules (e.g., proteins) have now become feasible(Shaw et al. 2018). Currently, simulation time ~ 100 ns (for MD) and system size ~ 15 nm are typically feasible with modest computational resources. Some intuition into the computational cost of these simulations can be achieved by considering a system of N atoms, with a pair interaction force between all pairs of atoms. One step of the simulation would involve the calculation of $\sim N^2$ pair-interaction forces or energies. Since the pair interactions would vary with inter-particle distances, these calculations need to be repeated after every simulation step and the simulation must be continued until the properties of interest converge to an average value (“thermodynamic equilibrium”). Massive speedups are obtained by noting that not all pair interactions needs to be computed in the case of short-ranged interactions (e.g., van der Waals interactions), as the interaction energies are much smaller than the thermal energy ($k_B T$) at long distances. In practice, only pairs within a small cutoff distance (~ 1 nm) are usually considered. Even in the case of long-ranged interactions (e.g. Coulomb interactions), approximations such as Ewald summation are invoked to facilitate faster computation of pair interactions at the expense of small inaccuracies in the determination of interactions energies.

The MC step/MD timestep needs to be small enough in order to be able to explore all possible states of the N-particle system (for MC simulations) or minimize the errors associated with the numerical integration of the equation of motion (for MD simulations). MD simulations of atomistic systems typically require time steps of the order of 1 fs and 1 million such steps are required to study the system behavior for 1 ns. In order to determine certain thermodynamic property, simulations must be run for a time significantly longer than the time scales of relevant phenomena. For example, hydrogen bonds form and break at time scales ~ 1 ps(Luzar and Chandler 1993), whereas nucleation and crystal growth occur at much longer time scales ($> 1 \mu$s)(Walsh et al. 2009) often going beyond the existing computational capabilities. Further, although the number of simulated molecules is almost always much smaller compared to the number of molecules in a real system, choice of N is not completely arbitrary as the obtained thermodynamic behavior must be representative of the real system. This is particularly an issue for simulation of macromolecules such as polymers and proteins often encountered in drug delivery, where the individual molecule size is much larger than the computationally feasible simulation box size. It has been the bottleneck for the extensive use of molecular simulations by the drug delivery community prior to 2000. The situation has however changed in recent times with an increasingly large number of studies reporting the use of molecular simulations in drug delivery.

Substantial gains in feasible time and length scales can be achieved using “coarse-grained” descriptions where several atoms of molecules are grouped together, which then interact via an “effective force-field” obtained after averaging out the lost degrees of freedom. In general, a system containing N atoms can be represented using N_c coarse-grained entities by lumping together N/N_c atoms into larger coarse-grained entities (beads). Higher values of the coarse-graining parameter N/N_c produce higher computational speedups ($\sim N^2/N_c^2$ times the atomistic simulations in the example given in the last paragraph) at the expense of loss of information regarding phenomena occurring at resolutions lower than N/N_c atoms. Another promising strategy is to remove the solvent molecules altogether (“implicit solvent”), resulting in drastic computational speedups in simulations of liquid-phase systems typically encountered in drug delivery. Although highly promising and heavily used, the coarse-grained descriptions must be taken with a pinch of salt, as the role played by the lost degrees of freedom is often underestimated. This also results in systematic inaccuracies in the computed forces and energies.

2.1.2. Comparison of molecular simulations with continuum approaches

Several alternate theoretical and simulation strategies have been used with some success in drug delivery problems, most prominent of which are continuum approaches (Table 2.2) such as those involving the analytical or numerical solution of convection-diffusion equations(Peppas and Narasimhan 2014; Siepmann and Siepmann 2012) or the Computational Fluid Dynamics (CFD) simulations(Steuperaert et al. 2017; Worth Longest and Hindle 2010). For instance, the compartment models of drug release through formulations(Huang, Lee, and Yu 2009; Yu, Crison, and Amidon 1996) have achieved significant success in the understanding of ADMET (adsorption, distribution, metabolism, excretion, and toxicity) characteristics of drug formulations and are routinely employed in formulation design and determination of dose levels. Provided reliable model parameter estimates are obtained from in vitro/in vivo experiments, such models are excellent tools as there is no practical limitation on the time and length scales that can be simulated as long as the model assumptions hold true. However, there are two major issues with these approaches. First, since these continuum approaches do not incorporate atomistic details, the information pertaining to the formulation chemistry is only captured at a rudimentary level and detailed molecular insights are not obtained. Therefore, these models are mainly employed after synthesizing formulations, unlike molecular simulations that can be employed in the design stage prior to synthesis. Second, the required experiments are time-consuming and expensive. Poor in vitro in vivo correlation is observed in many systems, which necessitate the use of many in vivo animal experiments involving sacrifice of healthy animals. Provided the relevant chemistry is known, better in vitro in vivo correlation can be obtained in atomistic simulations, thus minimizing the required experimentation.

Table 2.2 Comparison of Molecular Simulation Methods with Continuum Methods

Attribute	**Continuum Simulations**	**QM calculations**	**Atomistic Simulations**	**Coarse-grained Simulations**
Governing Equations	Transport equations (Fluid flow, heat transfer, mass transfer)	Schrödinger equation	Newton’s laws of motion, Statistical mechanics	Newton’s laws of motion, Langevin equation, Statistical mechanics
Assumptions	Continuum approximation	Mean field approximation, Neglect of electron correlations	Motion of atoms approximated by the motion of nuclei obeying Newtonian mechanics.	Effective degrees of freedom
Model Parameters	Viscosity, heat transfer coefficient, diffusivity	None	Force-field parameters (bonded and non-bonded)	Effective force-field parameters (bonded and non-bonded)

Simulation Output	Profiles of velocity, temperature, concentration of species	Charge distribution, Electronic structure, Potential energy	Coordinates and momenta of atoms, Thermodynamic properties	Coordinates and momenta of coarse-grained particles, Thermodynamic properties
Length Scale	Typically $> 1\mu$m (continuum approximation should hold)	Typically ~ 1 nm (within current computational capabilities)	Typically < 100 nm (within current computational capabilities)	Depends on coarse-graining resolution (between atomistic and continuum)
Time Scale	Typically $> 1\mu s$ (longer than molecular relaxation times)	Typically < 1 ns (within current computational capabilities)	Typically < 100 ns (within current computational capabilities)	Depends on coarse-graining resolution (between atomistic and continuum)

In the following, we discuss the current status of in silico methods for the design of drug delivery formulations, with special emphasis on the use of molecular simulation approaches such as atomistic and coarse-grained Molecular Dynamics (MD)/Monte Carlo (MC) simulations. Continuum approaches (e.g., diffusion equations), statistical methods(Panyukov and Rabin 1996) based on quantitative structure-activity relationships (QSAR)(Cherkasov et al. 2014) and quantitative structure–property relationships (QSPR)(Jorgensen 2009; Malani, Ayappa, and Murad 2009), and quantum-chemistry methods are beyond the scope of the literature. Also, we focus on drug delivery; conformal search methods and molecular docking methods used in drug design are not discussed and the readers are referred to recent reviews(Jorgensen 2009; Yuriev, Agostino, and Ramsland 2011) on these topics. In the following section, we discuss the basic scheme of atomistic MC and MD simulations. Since excellent texts(Allen and Tildesley 1989; Frenkel and Smit 2002; Leach 2001) are available on these methods, we do not delve deeply into the mathematical aspects of these methods and instead focus on the practical aspects relevant to drug delivery. Recent applications of these methods in the area of drug delivery is discussed afterwards, grouped by the properties of interest to drug delivery. Finally, we conclude with a perspective on the opportunities and challenges associated with the use of molecular simulations in drug delivery.

2.2. SIMULATION SCHEME

An atomistic MC/MD simulation typically involve the sequence of steps shown in Figure 2.1. Some applications, e.g., free energy calculations and grand-canonical ensemble simulations, require a more detailed protocol, which are discussed separately later. The initial geometry of the drug and other molecules (e.g., carrier, membrane, solvent) being studied are first built in a molecule builder program (e.g., Materials Studio(Accelrys Inc. 2017), Marvin(Csizmadia 2019), GaussView(Dennington, Keith, and Millam 2016), etc.) or obtained from a database (e.g., Protein Data Bank, ZINC, etc.). This is demonstrated in Figure 2.2a and 2.2b, for a model drug compound Doxorubicin and a model drug carrier polyacrylic acid, respectively. These geometries are then used to list all unique bonded and non-bonded atomic pairs in the system, and force-field parameters are specified for each of these pairs. In the next step, a simulation box is created and molecules of different species are added to the box according to their concentrations (Figure 2.2c-f). The usual practice is to add molecules one-by-one at random locations in the box, while avoiding the positions that are already filled. However, such scheme often results in few pairs of atoms being too close to each other or overlapping with each other. If an MC/MD simulation is started from this configuration, such pairs of atoms would have very high interatomic repulsions between them, resulting in numerical instabilities. It is therefore recommended to perform an energy minimization or a short MC (MD) simulation with a much smaller step length (time step) than that typically employed in the actual simulation. These simulations involve small relaxations of atoms and are continued until all pair-interaction forces fall below a specified tolerance.

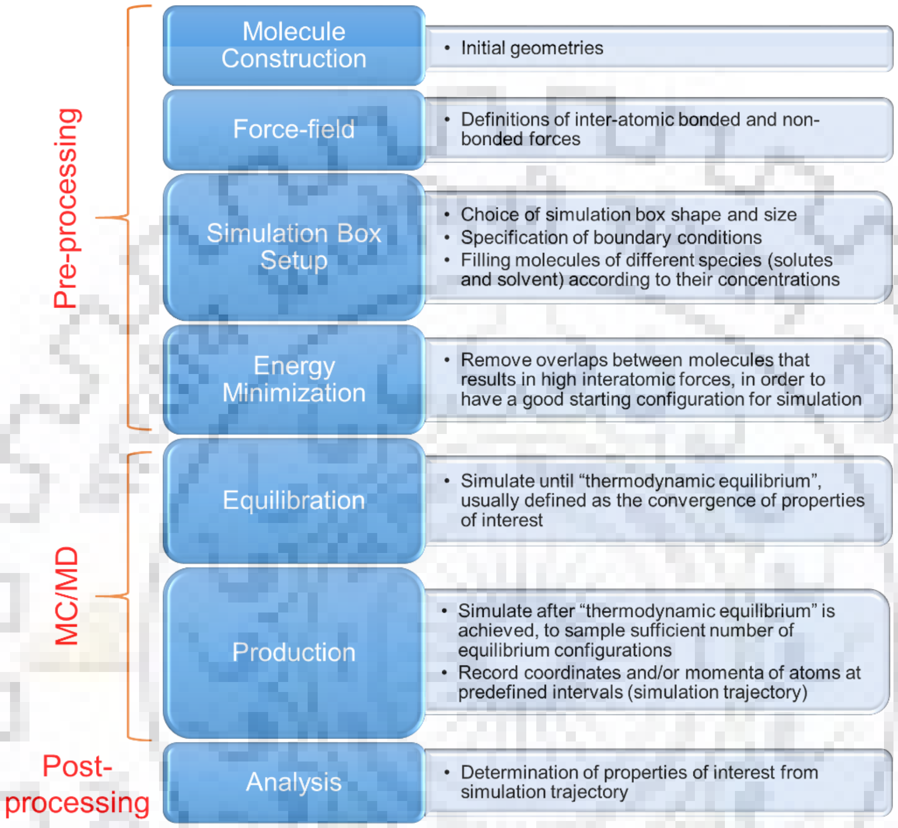
Pre-processing
MC/MD
Post-processing
Molecule Construction
• Initial geometries
Force-field
• Definitions of inter-atomic bonded and non-bonded forces
Simulation Box Setup
• Choice of simulation box shape and size
• Specification of boundary conditions
• Filling molecules of different species (solutes and solvent) according to their concentrations
Energy Minimization
• Remove overlaps between molecules that results in high interatomic forces, in order to have a good starting configuration for simulation
Equilibration
• Simulate until "thermodynamic equilibrium", usually defined as the convergence of properties of interest
Production
• Simulate after "thermodynamic equilibrium" is achieved, to sample sufficient number of equilibrium configurations
• Record coordinates and/or momenta of atoms at predefined intervals (simulation trajectory)
Analysis
• Determination of properties of interest from simulation trajectory

Figure 2.1 Basic steps of atomistic (MC/MD) simulations.

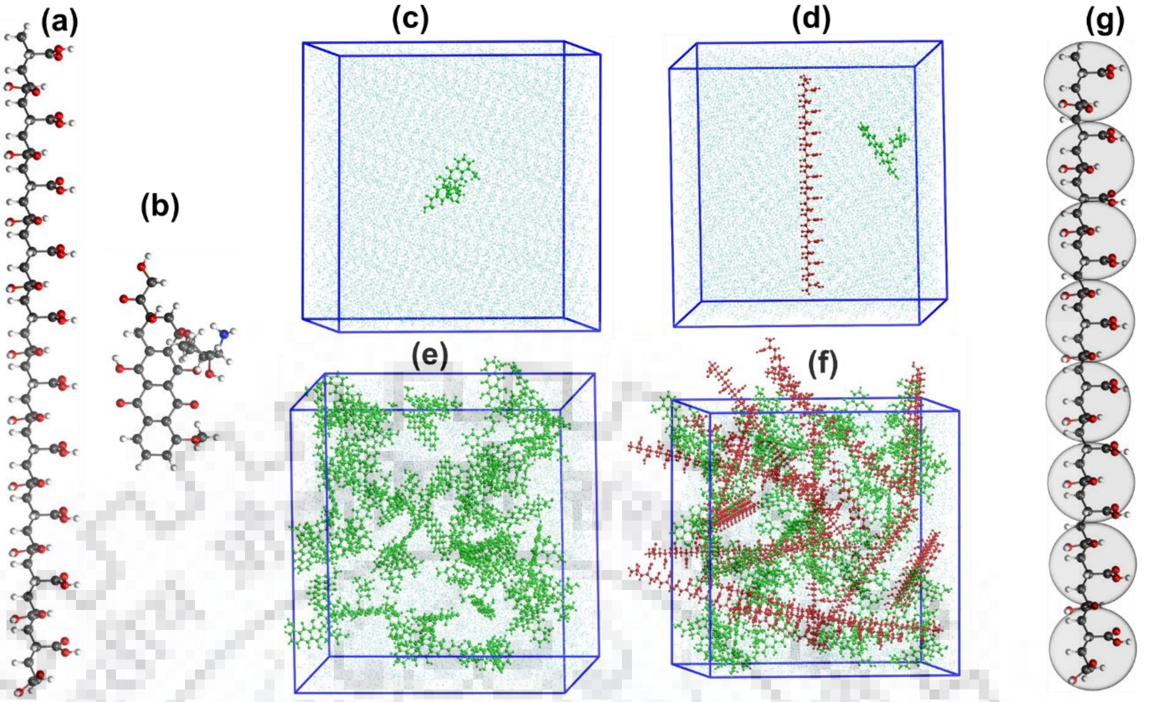

Figure 2.2 (a) and (b) shows the atomistic representation of a model polymeric drug carrier syndiotactic polyacrylic acid chain containing 20 repeat units (PAA20) and a model anti-cancer drug Doxorubicin (DOX), respectively. Here, carbon, hydrogen, oxygen, and nitrogen atoms are shown in grey, white, red, and blue colors, respectively. (c) and (d) shows initial simulation configuration of a single DOX molecule in water and a DOX molecule along with a PAA20 molecule in cubic simulation box of length 6 nm, respectively. Periodic Boundary Conditions (PBC) are used at all faces of the simulation box. (e) and (f) shows initial simulation configuration of multiple DOX molecules in water and multiple DOX molecule along with multiple PAA20 molecules, respectively. In Figure c-f, DOX, PAA20, and water molecules are shown in green, red, and cyan colors, respectively. Figure g shows a coarse-grained (CG) representation of PAA20 with the circles representing coarse-grained beads.

MC/MD simulations are performed starting from the configuration obtained after energy minimization and are comprised of equilibration and production steps. As suggested by the name, the equilibration simulations are performed to achieve a state of "thermodynamic equilibrium". It is important to understand that here the concept of "thermodynamic equilibrium" is loosely defined, since the total number of molecules in the system are much smaller than that in a macroscopic system. Specifically, fluctuations in thermodynamic properties that decay as the inverse square root of system size are often overestimated. Moreover, the typical practice is to monitor a thermodynamic property of interest with simulation time, and consider that the "equilibration" has been achieved when that property appears to converge, i.e., fluctuates around an average value. This scheme captures those relaxation modes of the system that occur at time scales shorter than the simulated time (e.g., of smaller molecules) but fails to capture slower relaxation modes (e.g., of macromolecules). Since the total possible simulation time is limited by computational capabilities and almost always much smaller than experimental time scales, our abilities to capture the complete relaxation behavior of macromolecules is far from perfect. Similar restrictions apply in the study of rare events such as crystal nucleation, though it is now possible to simulate such processes for small molecules(Walsh et al. 2009).

The production simulation begins from an equilibrated configuration and is performed to sample a statistically large number of equilibrium system configurations that are then used to compute the properties of interest. Both MC and MD simulations track the change in positions of atoms as a function of time, which can be used to determine structural quantities such as molecular size and pair distribution function. However, MD simulations also track the momenta of atoms that can be used to determine dynamical quantities such as diffusion coefficient. In order to obtain reliable measures of thermodynamic averages and fluctuations, it is important that the sampled configurations are uncorrelated in nature, that is, the time duration between two samples is sufficiently longer than the correlation time. Here, the correlation time is defined as the first order decay time constant of the autocorrelation function of the property of interest. Further, we assume that the system is ergodic in nature, that is, the time-averaged properties obtained from simulations for a representative subsystem would be identical to the spatial-averaged properties for the entire system. Whether this assumption holds true for a simulated system can be debatable(Cho and Joannopoulos 1992), but the success of MC/MD methods in predicting equilibrium properties for many diverse systems works in favor of the ergodic hypothesis.

2.2.1. Difference between MC and MD methods

As discussed earlier, both MC and MD methods can be used interchangeably in many cases to predict certain thermodynamic properties, which are averaged over large number of system configuration during production run. However, they essentially differ in their approach to explore phase space, i.e., how they obtain various system configurations. System configurations obtained at subsequent timesteps in an MD simulation are connected in time and indicate the trajectory (position and velocity as a function of time) of the molecules of the system, which is obtained by solving the equations of motion. On the other hand, an MC step consists of a random displacement of an atom or a collection of atoms in the system, which are accepted or rejected with a probability, assigning higher probabilities to moves that results in lower energies or smaller energy changes $\Delta E = E_{new} - E_{old}$. Here, the energies are obtained for the entire system that is a global operation, as opposed to force computation in MD simulation that is a local operation. Most MC simulations use the Metropolis criteria, where the moves resulting in a negative ΔE are always accepted and moves resulting in a positive ΔE are accepted with a probability equal to $\exp(-\Delta E/k_B T)$, which follows from the Boltzmann distribution.

Unlike the MD simulation where the atoms should move according to the true dynamics of the system, the movement of atoms in an MC simulation can be arbitrary as long as we satisfy "detailed balance"(Frenkel and Smit 2002), which refers to the equality of the rates of forward and reverse transitions when the system reaches equilibrium. Therefore, nonphysical collective moves performed using smart algorithms (e.g, translation and rotation of long polymer chains) can be used, which can result in a faster approach to equilibrium. One of the most advanced strategies in this category is the configurational bias MC methods(Siepmann and Frenkel 1992), where fragments of a large molecule are discarded/regrown within the simulation that allows for rapid exploration of phase space. Yet another advantage of MC simulation is that they are easily applied on various ensembles, e.g., isothermal-isobaric (NPT) and grand-canonical(Valleau and Cohen 1980) (μVT) ensemble. Phase equilibrium studies(Ganesan and Jayaraman 2014) are easily performed in Gibbs ensemble(Panagiotopoulos 1987) MC simulations, where one starts with two simulation boxes representative of two phases and particle transfers are performed between the two boxes. On the other hand, MD method has been developed assuming a microcanonical (NVE) ensemble and require the use of an artificial "thermostat" and "barostat" for performing simulations at constant temperature and constant pressure, respectively. These affect the performance of MD simulations and often results in poor prediction of dynamical properties. Despite these obvious advantages, atomistic MC simulations are less commonly employed than atomistic MD simulations. An obvious advantage of MD simulations is that it can used to compute the dynamical properties (e.g. diffusion coefficient) and study the non-equilibrium behavior of systems, which is not possible with conventional MC algorithms. However, recently developed kinetic Monte Carlo (kMC) simulations partly overcome this challenge(Jha, Kuzovkov, and Olvera de la Cruz 2012a, 2012b), where the probability of transitions are set equal to the transition rates obtained from the Smoluchowski diffusion equation(Sevilla and Sandoval 2015). Also, MC simulations are easy to perform in atomic systems with only translational degree of freedom, but suffer from practical difficulties in molecular systems with internal degree of freedoms. Systems with many internal degrees of freedom results in higher possibility of overlaps, which gives rise to higher rejection rates of random trial displacements. Moreover, requirement of global energy computations pose difficulties in parallelization of MC codes.

2.2.2. System Size and Boundary Conditions

As mentioned earlier, the simulation box must be of size large enough to be representative of the real system and small enough to be simulated using existing computational capabilities. In practice, simulation box sizes up to $10-30$ nm are within reach of current supercomputers(Huang, Dalal, and Larson 2014; Jha and Larson 2014) for simulations of the order of 100 ns (for MD). In order to facilitate the study of bulk system behavior using nanoscale simulations, periodic boundary conditions (PBC) shown in Figure 2.3 are often employed, where we assume that the system configuration in the simulation box is periodically replicated in an infinite lattice. Therefore, the simulation box must be space-filling and commensurate with a 3D lattice. For example, simulation box can be cubic but not spherical, as the latter is not space-filling. Also, PBC introduces certain finite-size artifacts due to the assumption of a “crystalline” order at length scales above the system size and the simulation must be performed for system sizes large enough in order to minimize such artifacts. In practice, this can be ensured by performing simulations at various system sizes until the properties of interest converge with system size. However, for certain properties (e.g., diffusion coefficient), such convergence is never achieved and a well-defined property scaling with system size is obtained(Yeh and Hummer 2004). In many other cases, it may not be feasible to simulate systems beyond a certain size to confirm the convergence with system size and we must be skeptical about the simulation results. Simulations of macromolecules such as polymers and proteins is more problematic as their actual size is too large to be simulated as the whole molecule and fragment(s) of molecule can only be studied(Iyer, Lele, and Shanbhag 2007). In such cases, it is desirable that the simulation box size is significantly larger than the maximum possible size of the fragment in the unfolded configuration.

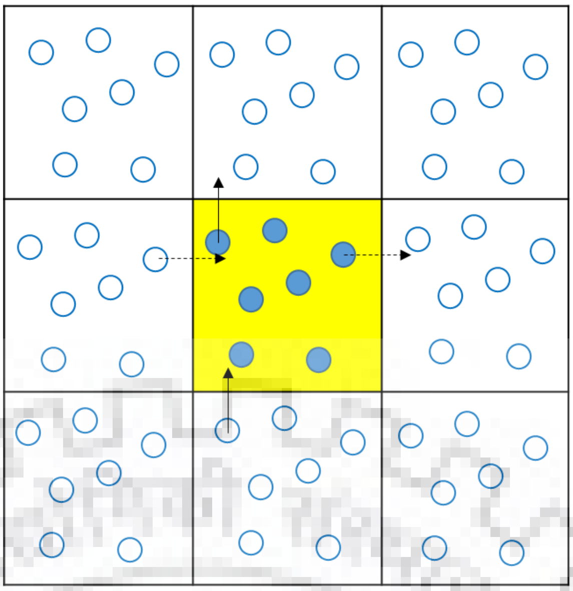

Figure 2.3 2D Representation of periodic boundary condition. The central cell (filled with yellow) represent the simulation box. Filled circles represent particles in the simulation box and open circles represent their periodic image in other cells. Bold and dashed lines shows movement of two particles near the boundary; as a particle leaves the simulation box, its image enters the box from the opposite end.

Scientists engaged in molecular simulations often fear that since the computing speeds will undergo a tremendous growth in the years following the publication, findings of the study may later prove to be false or limited in scope. Indeed, the assumption that the simulations of small fragments of a large system for nanoseconds would capture the behavior of the large system for realistic time scales is a mere necessity. Long-range correlations and long-time relaxations are features present in most systems that are being studied and are purposely ignored. Even worse, critics of molecular simulations argue that a microscopic study of various components of the system is not sufficient to predict the behavior of the system-as-a-whole, since unique system characteristics may emerge due to correlations between the system components. For instance, while the pharmacological response of a drug may be evaluated using the known chemistry of drug and the physiological environment, variations in the pharmacological response due to psychological factors involving the brain may be important but are ignored. Though this criticism may be valid, this should not deter us from performing such microscopic studies using molecular simulations with a well-defined goal of determining predictable microscopic behavior of systems that can be verified using experiments. Fortunately, a substantially large number of molecular simulations that are reported are successful in meeting this goal where the findings are either supported by experiments at the time of publication or are experimentally verified later. With such focus and a continuous updating of our findings as computing power grows, we can hope to win over the critics.

2.2.3. Coarse-graining

A huge leap in computational speed is obtained by using coarse-grained (CG) representation of molecules in place of an atomistic representation, exemplified by the CG representation of PAA20 shown in Figure 2.2g. United-atom force-fields (e.g, GROMOS, OPLS-UA) achieve a lower-level coarse-graining by not explicitly including hydrogen atoms attached to aliphatic and aromatic carbon atoms, that is, a united-atom representing the interaction center of CH_n is used in place of a carbon and n hydrogen atoms. Since the hydrogen atoms linked to oxygen are still treated explicitly, the solvent molecules are treated the same as in the all atom force field. Therefore, the computational gains of united-atoms are mainly observed in simulations of large molecular weight hydrocarbons in solid or gaseous states. The MARTINI force-field(Marrink et al. 2007) uses a relatively higher-level coarse-graining, where four heavy atoms and associated hydrogens are combined to form a MARTINI particle type, which are further classified into subtypes according to their polarity. Further, MARTINI water model comprise of four water molecules, which results in substantial computational gains even for liquid-state systems. The recently developed dry MARTINI force field(Arnarez et al. 2015) takes it to an even higher level, by completely removing the solvent beads and including the effect of solvent in the parameterization of inter-particle forces between the solute molecules. More aggressive coarse-graining approaches are inspired from the bead-spring models(Everaers et al. 2004; Liao, Dobrynin, and Rubinstein 2003) that have been proved to be great tools in qualitative understanding of polymer behavior. In such models, the level of coarse-graining, number of atoms in a “bead”, and the interaction between beads is loosely defined, as the objective is to capture universal scaling laws applicable for large molecular weights. However, more recent studies have used mapping of beads to certain number of atoms in the system (e.g., one repeating unit(Huang et al. 2016b)). Though the force-field parameters for united-atom models are now available for a wide range of systems, the other CG methods described above typically require an atomistic simulation to build the CG model parameters. The typical protocol for developing such parametrization involve the following steps. First, a CG model is developed and the form of inter-particle forces are decided. Second, both atomistic and CG simulations are performed for a small-sized system where both these simulations are feasible. Third, certain property is determined from both these simulations, where the atomistic simulation results are the "target" values of the property. CG model parameters or the form of inter-particle forces are then refined in subsequent CG simulations, in order to match the "target" values. This process is continued until CG simulations are able to reliably reproduce the "target" values. The resulting CG model can then be used in cases where atomistic simulation is not feasible. Iterative Boltzmann Inversion (IBI) scheme(Müller-Plathe 2002) and force-matching method(Izvekov and Voth 2005) uses the inter-particle RDF and inter-particle forces as the "target" values, respectively.

Coarse-grained models can be developed using a top-down or bottom-up strategy. The top-down strategy is based on the premise that the behavior of a system can be understood by incorporating only certain degrees of freedom. On the other hand, the bottom-up strategy assumes that certain degrees of freedoms of a system are less important than others and thus can be ignored ("averaged-out"). An excellent example to demonstrate the two models is a polymer chain in solution. In the top-down approach (*generic coarse-graining*), we begin by noting that the mean squared end-to-end distance of the polymer chain follows universal scaling laws, which are then established by using simple random-walk descriptions of toy models of polymer chain (e.g., freely jointed chain) without worrying about the details of polymer chemistry. In the bottom-up approach (*systematic coarse-graining*), we begin with a fully-atomistic representation of polymer chain in a solvent, where we first average-out the effect of solvent (implicit solvent) by incorporating an average drag and a random noise. This is usually followed by reducing the degrees of freedom of the polymer chain by lumping several atoms into beads that interact via effective forces. Analogy can be seen with taking images of an object from a camera. In generic coarse-graining, we capture the behavior that we see and hypothesize a representation that gives the same behavior; in systematic coarse-graining, we first zoom in to higher magnification to look at certain behavior followed by zooming out to lower magnifications while building a representation that preserves that behavior.

The most commonly used generic coarse graining models of polymeric chains are (Dobrynin and Rubinstein 2005; Van Krevelen and Te Nijenhuis 2009):

1. Freely joined chain model is typically used to describe flexible chains. The polymer is assumed to be composed of "Kuhn segments" whose individual motions are uncorrelated. The mean squared end to end distance for a chain of N Kuhn segments with length of each segment ("Kuhn length") A

$$\langle R_e^2 \rangle = NA^2$$

The contour length of the chain L can be used to relate to the bond length as

$$L = NA = nl$$

where n is the number of bonds and l is the bond length.

2. Wormlike chain model is typically used to represent semiflexible chains. Polymer chain is a assumed to be a continuous line with the tangent at each point indicating the bond vector. Mean squared end-to-end distance vector is given as

$$\langle R_e^2 \rangle = 2l_p \left\{ L - l_p \left[1 - \exp\left(\frac{-L}{l_p} \right) \right] \right\}$$

l_p is the persistence length defined as half the Kuhn length.

3. Bead-spring model is most commonly employed in computer simulations for simulations of flexible polymers where the chain is represented using beads connected by springs. The energy of springs is often assumed to be of the form $\frac{1}{2}k(l - l_0^2)$ where k is the spring constant and l_0 is the "equilibrium bond length".

2.2.4. Free-energy calculation

For many applications in drug delivery, we are interested in the free energies(Beveridge and DiCapua 1989; Jorgensen 1989; Kollman 1993) instead of equilibrium properties obtained using conventional MC/MD simulations. One common example is the formation of drug-receptor complexes(Ajay and Murcko 1995; Pan et al. 2013), where the binding free energy of complex determine the equilibrium constant of binding process. To determine these free energies, thermodynamic integration scheme is usually followed, where we integrate the energy changes along a pre-defined path of a coupling variable λ. For example, we gradually switch the coupling between drug and receptor, from $\lambda = 0$ (unbound state) to $\lambda = 1$ (bound state). The free energy change is then described using the equation,

$$\Delta A = \int_0^1 \langle \frac{\partial U}{\partial \lambda} \rangle_\lambda \, d\lambda$$

Here the energy in the intermediate states $U(\lambda)$ is determined using the force field equation given in section 2.3. However, these calculations are tedious when computing free energy changes in a solution phase, as the formation of such complexes is limited by slow solvent equilibration. Rapid binding energy calculation can be performed using the concept of a thermodynamic cycle, as illustrated in Figure 2.4 for the case of drug-receptor binding(Dickson, Tiwary, and Vashisth 2017; Vashisth 2015). Here, thermodynamic integration calculation is first performed in vacuum and obtained free energy changes are added to the free energy change of desolvation of unbound drug and receptor and that of solvation of bound drug-receptor complex. Yet another and simpler application of this concept is in the calculation of solvation free energies of drug and carrier molecules. Alternate strategies to obtain the free energy changes involve the use of a bias potential (e.g., umbrella sampling) and metadynamics method(Barducci, Bussi, and Parrinello 2008), which are useful for systems with multiple free-energy minima. Such strategies are also highly useful in the study of rare events, such as nucleation and growth of crystals(Filion et al. 2010).

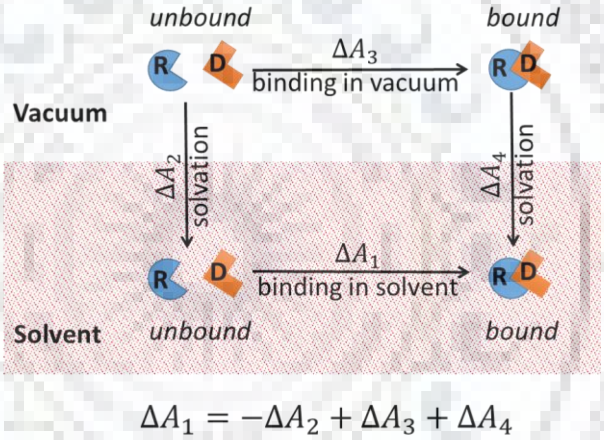

unbound
bound
ΔA_3
binding in vacuum
R
D
R D
Vacuum
ΔA_2 solvation
ΔA_4 solvation
ΔA_1
binding in solvent
R
D
R D
Solvent
unbound
bound
$\Delta A_1 = -\Delta A_2 + \Delta A_3 + \Delta A_4$

Figure 2.4 Thermodynamic cycle used in the calculation of binding free energy.

2.2.5. Force-fields

A large variety of force fields are employed in molecular simulations, some of which are listed in Table 2.3. Although the force fields substantially differ in the functional form and model parameters of different interactions and parameters, they broadly comprise of the following interactions:

i. Bond stretching between adjacent bonded pairs of atoms in a molecule,

ii. Angle bending between three consecutive atoms in a molecule,

iii. Bond rotation (torsion) between four consecutive atoms in a molecule referred as a ‘proper’ dihedral,

iv. Out-of-plane bending to maintain planar structure of certain molecules, e.g., benzene, modeled using an ‘improper’ dihedral involving a group of atoms in a molecule,

v. Coulombic interaction between pairs of atoms of the same or different molecule(s) due to the partial charges of atoms,

vi. van der Waals interactions between pairs of atoms of the same or different molecule(s).

That is, in general,

$$\Delta FF = \Delta F_b^{bonds} + \Delta F_\theta^{angles} + \Delta F_\phi^{dihedrals} + \Delta F_\phi^{impropers} + \Delta F_{vdw} + \Delta F_{elec}$$

In addition, cross-terms involving more than one interaction type listed above are also present in certain force fields. It is worth pointing out that the concept of a bond, angle, dihedral, and partial charges, are features of a molecular mechanics force-field and are not inherent to the QM representation. Instead, they emerge from the mapping of the QM representation to an atomistic representation. For example, partial charge can be loosely defined as a measure of net charge density in the vicinity of the atom and assumes negative (positive) values for electronegative (electropositive) atoms. Therefore, in principle, the force-field parameters can be completely determined from QM calculations. In practice, however, these calculations are tedious and the force-field accuracy suffers from the approximations made during force-field formulation (e.g., treatment of van der Waals interactions, use of point charges, neglect of polarization effects, etc.) and limitations of the empirical data used in the force-field parametrization. Usually, the force-field development involves a mix of QM calculations and empirical fitting of force-field parameters to reproduce certain experimentally obtained molecular properties. Thus, the terms corresponding to different interactions listed above in a force-field should not be construed as the exact measure of those interactions. Instead, the resulting functional form should be viewed as a convenient mathematical expression with model parameters that provides best fit of the system behavior.

Table 2.3 List of commonly used force fields

Force field family	**Variants**	**Original Developer**
CHARMM	CGenFF, CHARMM22, CHARMM27, CHARMM36	Martin Karplus, Harvard University
OPLS	OPLS-AA, OPLS-UA	William Jorgensen, Purdue University & Yale University
AMBER	GAFF, GLYCAM, ff94, ff96, ff98, ff99, ff02, ff02EP, etc.	Peter Kollman, University of California San Francisco
Consistent force fields	COMPASS, COMPASS II, CFF, CFF91, PCFF	Molecular Simulations Inc. (now Biovia)
UFF	UFF	William Andrew Goddard III, California Institute of Technology
MMFF	MMFF, MMFF94	Merck Research Laboratories
GROMOS	GROMOS 43a1, 43a2, 43b1, 45a3, 53a5 and 53a6	Wilfred van Gunsteren, University of Groningen & ETH Zürich
MARTINI	MARTINI	Siewert J. Marrink, University of Groningen, and Peter Tieleman, University of Calgary

2.2.6. Simulation software

The development of efficient computer programs to perform molecular simulations is a time-intensive task and requires expertise of people from various disciplines. Thankfully, a concerted effort of scientists across the globe has resulted in a range of highly efficient and capable open source and commercial software (Table 2.4). In addition, many software and online portals are separately used for building molecules (e.g., Materials Studio, Marvin, etc.), determining force-field parameters (e.g, SwissParam, ATB, PRODRG, MKTOP, OBGMX, etc.), and analysis and visualization of results (e.g., VMD, PYMOL, RASMOL, CHIMERA, etc.). Such user-friendliness of these software have promoted large-scale use of molecular simulations, giving rise to skepticism that the results are being generated and reported without proper understanding of algorithmic details and thus prone to being wrong. This skepticism is valid to a certain extent and a thorough study of the working of a software and its features and limitation must be performed before using it in a practical application.

Table 2.4 List of commonly used molecular simulation softwares

Software	Distribution	Maintained By	Features
GROMACS	Open-source	University of Groningen, Netherlands	MD
LAMMPS	Open-source	Sandia National Laboratories	MD
CHARMM	Commercial	Martin Karplus and others (Academic version), Biovia (Commercial version)	MD
AMBER	Commercial	David Case, Rutgers University, and others	MD
NAMD	Open-source	Klaus Schulten, University of IIlinois at Urbana-Champaign	MD
DESMOND	Commercial	D. E. Shaw Research	MD
DL_POLY	Commercial	W. Smith and T.R. Forester, Daresbury Laboratory	MD
ACEMD	Commercial	Acellera Solutions	MD
Materials Studio	Commercial	Biovia	MD, MC, QM, MM
MacroModel	Commercial	Schrodinger LLC	MM, MD, MC

2.3. APPLICATIONS IN DRUG DELIVERY

Thousands of studies have been reported in recent years that use molecular simulations for applications in drug delivery. A large fraction of these studies concern the drug-receptor binding or docking studies, which are not the focus of this review. Table 2.5 shows representative studies in last couple of decades that use molecular simulations in applications other than docking. A cursory glance of Table 2.5 will reveal that the system size and simulation time have increased many fold over the years, thus enabling studies of systems containing large numbers of molecules. Moreover, while the earlier studies focused on local properties of single molecules (e.g., molecular surface area(Krarup et al. 1998), drug orientation in a bilayer(Alper and Stouch 1995; Baginski, Resat, and McCammon 1997), etc.), recent studies have increasingly focused on the global behavior of a collection of molecules (e.g., phase behavior(Birru, Warren, Han, et al. 2017; Jämbeck et al. 2014; Jha and Larson 2014; Warren, King, Benameur, Colin W. Pouton, et al. 2013), crystallization(Greiner, Elts, and Briesen 2014a; Mandal, Marson, and Larson 2016), etc.). In the following, we discuss five main areas of applications of molecular simulations in drug delivery.

Table 2.5 Representative studies using molecular simulations in drug delivery

Reference	**System**	**Simulation software and method**	**System Size**	**Simul-ation time**	**Properties**	**Comparison / Correlation to experiment**
Alper and Stouch 1995	Nifedipine in a phospholipid bilayer	DISCOVE-R, MD	~4 nm	4 ns	Drug orientation in bilayer, drug diffusion rate	No
Baginski et al. 1997	amphotericin B (AmB)/cholesterol channel in a phospholipid membrane	CHARMM, MD	~4.5 nm	~60 ps	Hydrogen bonding, channel structure	No
Krarup et al. 1998	6 beta-blocking agents and their prodrugs	Sybyl, Energy minimization and MD	~ 1 nm	1 ns	Molecular surface area and molecular volume	Correlation with apparent permeability
Tang and Xu 2002	Halothane on a gA channel in a DMPC membrane	NAMD, MD	~7.5 nm	2.2 ns	Drug orientation, drug-drug binding, channel structure and dynamics	No

Bemporad, Luttmann, and Essex 2005	3 beta blockers in a DPPC bilayer	CHARMM, MD, MC	~5.5 nm	~4 ns	Drug orientation, hydrogen bonding	No
Mohanambe and Vasudevan 2005	Ibuprofen, Diclofenac, and Indomethacin, within the galleries of an anionic clay, Mg-Al layered double hydroxide (LDH)	Cerius or Materials Studio, MD	~2 nm	50 ps	Drug geometry and orientation, layer structure	Comparison of interlayer spacing with X-ray diffraction. Correlation of layer structure with Raman spectra.
Huynh et al. 2008	Docetaxel with various excipients	Cerius, MD	~3.5 nm	800 ps	Solubility, Flory-Huggins interaction parameter	Comparison with solubility
Patel, Lavasanifar, and Choi 2008	Fenofibrate and nimodipine in micelle-forming PEO-b-PCL block copolymers	Material Studio, MD	~3 nm	2 ns	Solubility parameter, Flory-Huggins interaction parameters	Correlation with solubility
Patel, Lavasanifar,	PCL-PEO block copolymer	Materials Studio, MD,	~2 nm	2 ns	Flory-Huggins interaction	No

and Choi 2010	with hydrophobic drug				parameters, hydrogen bonding, radial distribution function	
Subashini et al. 2011	Different combinations of 3 drugs and 6 polymers	GROMACS, MD	~7 nm	300 ps	Polymer-drug interaction energy, hydrogen bonding	Correlation with drug uptake by polymer
Boggara and Krishnamoorti 2010	Aspirin and ibuprofen in DPPC bilayer	GROMACS, MD	~6.5 nm	5 ns	Free energy, Hydrogen bonding, Drug hydration, Permeability	Comparison with ranking order of partition coefficient
Adnan et al. 2011	Doxorubicin (DOX) on a faceted nanodiamond (ND)	Constant-pH MD	Up to 18 nm	100 ps	DOX-ND binding	Comparison with experimental DOX-ND binding capacity
Abdel-Halim et al. 2011	Beclomethasone dipropionate (BDP)	Material Studio, MD	~3.5 nm	25 ps	Glass transition temperature, T_g	Comparison with experimental T_g

Gupta et al. 2011	Indomethacin in carriers	Materials Studio, MD	3 nm	50 ps	Solubility parameters, miscibility	Correlation with data from thermal analysis
Zhu et al. 2012	Griseofulvin with surfactants and polymers	Material Studio, MD	~ 5.5 nm	500-800 ps	Interfacial binding energy of polymer/ surfactant with drug	Correlation with crystal growth data
Luo and Jiang 2012a	Camptothecin (CPT) in PAE-PEG copolymer	Materials Studio, MD and DPD	104.3 nm (DPD)	Up to 1260 ns	MD: Flory–Huggins interaction parameters and miscibility DPD: Drug loading/ release	No
Paloncýová, Berka, and Otyepka 2013	Drug substrates of cytochrome P450s on DOPC and POPG membrane	GROMACS MD	~5 nm	10.25 ns	Free energy of drug penetration	No
Warren, King, Benameur, Colin W	MGL-DGL lipids with/without drugs	GROMACS , MD	Up to ~13.5 nm	100 ns	Phase behavior	No

Pouton, et al. 2013						
Jämbeck et al. 2014	Hypericin in liposome	GROMACS, CG MD	~12.5 nm	~ 10 μs	Phase behavior, free energy	No
Gao and Olsen 2013	Acetaminophen crystal	NAMD, MD	~12 nm	~10 ns	Interaction energies, crystal dissolution	Correlation with experimental dissolution behavior
Carpenter et al. 2014	Model drug compounds with DOPC membrane	GROMACS, MD	~6 nm	25 ns	Diffusivity and permeability	Comparison of permeability
Jha and Larson 2014	Phenytoin with cellulosic excipients	GROMACS, MD, 10-20 ns	Up to 15 nm	Up to 100 ns	Phase behavior, drug aggregation, drug diffusivity	No
Bernini et al. 2014	Ibuprofen on metal-organic frameworks (MOF)	RASPA, GCMC	~ 3 nm	~ 2×10^6 MC steps	Drug capacity, drug adsorption	No
Wang, Ren, and Meng 2015	6 beta-blocker drugs with POPC bilayer	GROMACS, MD	~ 7 nm	10 ns	Free energy, hydrogen bonding, bilayer structure, drug orientation	No

Yousefpour et al. 2015	Amlodipine, atenolol and Lisinopril, with DMPC bilayer	GROMACS, MD	~7 nm	100 ns	Drug orientation, diffusivity, hydrogen bonding, bilayer structure, free energy	No
Melchior et al. 2015	Cisplatin aqua-derivatives	DLPOLY, MD	~ 1 nm	~2 ns	Hydration structure, hydration number	No
Moghadam and Larson 2017	Phenytoin with polymer excipients	GROMACS, MD	5-10 nm	90 ns	Polymer-drug interactions, drug aggregation	No
Mandal et al. 2016	Phenytoin crystal	GROMACS, Atomistic and CG MD, Well-tempered metadynami-cs	~ 6.5 nm	~100 ns	Drug crystal growth, adsorption free energy, Crystal polymorphs	Correlation with crystallization data
Xiang and Anderson 2017	Felodipine with HPMC	Amber, MD	~ 2 nm	30-100 ns	Solubility parameter, Flory-Huggins interaction parameter, miscibility,	No

					phase behavior, hydrogen bonding	
Mahdavi, Rahmani, and Nouranian 2016	Doxorubicin on pristine graphene (PG) and graphene oxide (GO) nanocarriers	Materials Studio, MD	4-6 nm	1-3 ns	Drug graphene interaction energy, drug loading and release	No
Huang, Mandal, and Larson 2017	Phenytoin with HPMCAS	GROMACS, atomistic MD, CG BD	~35 nm (CG)	~ 10μs	Phase behavior, drug aggregation, polymer-drug interaction	No
Liang, Shen, and Wang 2017	Anticancer drugs with DNA nanotubes (DNT)	GROMACS, MD	~11.5 nm	60 ns	Drug absorption on DNT	No
Birru, Warren, Han, et al. 2017	Danazol in simulated GI environment	GROMACS, MD	15 nm	~200 ns	Phase behavior, drug aggregation, solubility	Correlation of phase behavior with experiments
Greiner, Elts, and Briesen 2014b	Aspirin nanocrystal	GROMACS, MD	~15 nm	150 ns	Crystal dissolution	Correlation with experimental

						dissolution behavior
Lu et al. 2017	Paclitaxel in DPPC bilayer under shock waves and nanobubbles	GROMACS, MD	~9 nm	600 ns	Drug-bilayer interaction, membrane penetration	No

2.3.1. Drug diffusion and permeation through lipid bilayer

The bioavailability of a drug depends strongly on its ability to migrate through the lipid bilayer membrane. According to the classical Meyer-Overton rule(Missner and Pohl 2009), hydrophobic drugs are lipophilic and thus find it easy to migrate through the lipid membrane. In crude terms, the hydrophobicity/lipophilicity can be characterized by the number of hydrogen-bond donors and acceptors in a molecule,(Lipinski et al. 2012) which can be accessed by looking at its chemical structure. Molecular simulations provide much detailed information such as the orientation of the drug molecule (defined with respect to the bilayer normal) and the energetic interactions of the drug with the bilayer constituents.(Alper and Stouch 1995; Bemporad et al. 2005; Yousefpour et al. 2015) Such studies have been applied with success on a diverse range of drug and membrane chemistries. In addition, molecular simulations can provide insights into the role played by transporter molecules and identify other sources of departures from the Meyer-Overton rule(Alper and Stouch 1995). Finally, molecular simulations can elucidate the mechanism of channel formation(Baginski et al. 1997) and provide detailed insights into bilayer structure and dynamics(Tang and Xu 2002).

2.3.2. Drug solubility

Drugs with high solubility in gastric and intestinal fluids tend to possess high concentrations in these environments, which should favour high drug absorption. However, since the gastric and intestinal fluids are aqueous in nature, high drug solubility in these fluids is observed for hydrophilic drugs, which in turn have low membrane permeability. It is therefore apt to characterize both the solubility and permeability of a drug molecule. This is the basis of the Biopharmaceutics Classification System (BCS)(Löbenberg and Amidon 2000); drugs are broadly classified into four classes: Class I (high permeability, high solubility), Class II (high permeability, low solubility), Class III (low permeability, high solubility), and Class IV (low permeability, low solubility). As noted earlier, one indirect measure of solubility is the number of hydrogen-bond donors/acceptors, which is included in the famous Lipinski rule of five(Lipinski et al. 2012) to evaluate drug-likeness of molecules. An alternate theoretical description of solubility is based on the thumb rule “like dissolves like”; molecules are assigned a “solubility parameter”(Barton 1991; Hancock 1997; Hansen 2007) and two molecules are considered to be soluble if the difference in their solubility parameters is small. Although the solubility parameters can be estimated from available experimental data or can be derived from the molecular structure using a group-contribution method(Fedors 1974), a more accurate determination can be achieved using molecular simulations (Gupta et al. 2011; Huynh et al. 2008; Patel et al. 2008; Xiang and Anderson 2017), especially in the case of novel drug candidates. Further, complete understanding of changes in drug solubility with changes in pH and salt concentrations occurring in the gastro-intestinal tract can only be attained by the use of molecular simulations.

2.3.3. Carrier-drug miscibility

In the case of poorly soluble drugs, various carrier molecules (excipients) are used to enhance their solubility or maintain drug supersaturation. Molecular simulations can assist in the selection of such excipients, as methods for quantification of drug-excipient interactions. Roughly speaking, molecules that form physical complexes with drug molecules are ideal excipients, but the drug-excipient binding should not be too strong to prevent the eventual release of drug molecules. One of the ways to quantify the drug-excipient interactions especially for the case of polymeric excipients is the use of Flory-Huggins interaction parameters(Marsac, Shamblin, and Taylor 2006) that can be estimated from molecular simulations.(Gupta et al. 2011; Patel et al. 2008; Xiang and Anderson 2017) More importantly, molecular simulations can also provide a detailed insight into phase behavior of excipient-drug combinations, i.e., composition-dependent changes in excipient-drug miscibility and complexation(Jha and Larson 2014). As an illustrative example, Jha and Larson(Jha and Larson 2014) have performed atomistic MD simulations to access the compatibility of cellulosic polymers (HPMC and HPMCAS) with the drug phenytoin for a range of polymer-drug compositions and polymer chemistries. Using the polymer-drug and drug-drug radial distribution functions, they correlated the polymer-drug complexation with the inhibition of drug aggregation; drug diffusivity through carrier was used as an indicator of drug release rate. Moreover, by sequential removal of water molecules followed by re-equilibration, they were able to mimic the dissolution process in a reverse manner, as the final solvent-free state correspond to the dose form. Significant attention has been achieved recently by the pH-responsive excipients that contain the drug molecules at lower pH of the stomach and release them at higher pH of the intestine. Molecular simulations may serve as excellent tool to design such excipients, as demonstrated recently for the doxorubicin-graphene(Mahdavi et al. 2016) and doxorubicin-nanodiamond systems(Adnan et al. 2011).

2.3.4. Drug crystallization

Several oral dosage forms contain drug molecules in crystalline form; poorly soluble drugs may also have a tendency to crystallize in the body. Since the crystalline forms of a drug have poorer absorption when compared to amorphous forms of the same drug, it is often desired to suppress such crystallization by using excipients that inhibit crystallization. From the computational standpoint, molecular simulations of crystallization processes are enormously expensive, which stems from the fact that crystals are structures with long-range spatial correlations (require simulations of larger system sizes) and nucleation is a rare event (require very long simulations or the use of smart algorithms). Though the simulations of crystal nucleation of large drug molecules from molecular simulations remain a far-fetched goal, significant progress has been made in the last decade on the simulations of crystal growth(Mandal et al. 2016) and dissolution(Gao and Olsen 2013; Greiner et al. 2014b). Such simulations can be used to compare the crystallization inhibition tendency of different molecules, identify crystal faces with higher growth rates, and to predict crystal habit of novel drug molecules. An important mention needs to be made here about the systematic yet aggressive coarse-graining approaches(Mandal et al. 2016) that succeed in the modeling of crystal growth with proper parametrization achieved through atomistic simulations(Jha and Larson 2014).

2.3.5. Drug loading and release

In the context of carrier-mediated drug release, drug loading and release refers to the incorporation of the drug in the carrier and its subsequent release inside the body, respectively. Since the drug loading and release processes occur due to the difference between the osmotic pressures inside and outside the carrier, we require to change the environmental condition in order to change the direction of drug movement. Typically, drug loading is conducted in a non-aqueous solvent, since the ultimate release occurs in an aqueous medium inside the body. Although continuum approaches beginning from the Higuchi equation(Manga and Jha 2017; Petropoulos, Papadokostaki, and Sanopoulou 2012; Siepmann and Peppas 2011, 2012) have been highly successful in the study of the drug loading and release from carrier matrices, such approaches do not usually include the structural details of the carrier. In particular, if the loading/release involves the formation of drug-excipient nanostructures, molecular simulations can provide a detailed description of the mechanism of drug loading/release. However, unlike continuum approaches, results of molecular simulations do not facilitate a direct comparison with experimentally determined loading/release data of drug formulations due to wide disparity in the simulated and actual length and time scales. An indirect yet useful approach is to obtain the drug diffusivity through the carrier, which can either be correlated with the experimental data or used as a model parameter in the continuum model. While such correlations are often direct and useful to rank the performance of different carriers(Larson et al. 2014), an accurate determination of drug diffusivity is not possible due to its dependence on system size. A more promising strategy is the use of systematic coarse-graining strategies that uses atomistic simulations to parametrize coarse-grained simulations. As an example, Luo and Jiang 2012 have integrated atomistic MD and coarse-grained DPD simulations to study the drug loading and release behavior of pH-sensitive release behavior of amphiphilic copolymers.

2.4. PERSPECTIVE

Can we build drug delivery systems of the future by obeying the Newton's laws of motion and theories of statistical mechanics? This seemingly unrealistic dream may become true one day given the rapid pace of growth in the molecular simulation field. The challenges however are two-fold, first to discern the molecular mechanism underlying the drug action in the body that need to be simulated, second to make our computers and computer programs fast enough to do such simulations. While the pace of growth in both these aspects have been rather encouraging in the last few decades, there is still a long way to go before this dream becomes true. Specifically, despite rapid growth in computing speeds in last couple of decades, there remains a huge gap between the system size and time scales of the simulated systems and realistic systems. Because of this, in silico tools based on the concept of molecular simulations have so far played a supporting role compared to in vitro and in vivo experimentation. They provide means to gain a molecular insights into specific systems and to provide a method to rank efficiency of candidate drug formulations. In most cases, the simulation predictions do not facilitate a direct comparison with an experimental observable, but provide useful correlations between the predicted quantities and experimental observables. For instance, drug diffusivity obtained in the simulations correlates positively with the experimentally obtained drug release behavior. Therefore, despite the inherent limitations of molecular simulations, they have tremendous potential as virtual screening tool of drug carriers and may assist in the development of design rules for drug delivery formulations. In particular, molecular simulations have a decisive edge over continuum approaches that do not incorporate the chemical and structural details of drug formulations. These are relevant to phenomena such as drug diffusion and membrane permeation, drug solubility, carrier-drug miscibility, drug crystallization, and drug loading and release.

One of the key areas for future development is multiscale simulations,(Peter and Kremer 2009; Praprotnik, Site, and Kremer 2008) especially those based on systematic coarse-graining. Not only do they allow us to extend the applicability of atomistic simulations to an order-of-magnitude higher length and time scales, they may be able to provide a systematic method to achieve model parameters for continuum approaches used at physiological length and time scales. The challenge however is to identify the degrees of freedom to be averaged-out, which are expected to have diminishing effect at progressively higher length/time scales. Yet another key area is the development and usage of efficient sampling strategies (e.g., metadynamics(Barducci et al. 2008)) to accelerate atomistic simulations. These are particularly useful in free-energy calculations and study of slow (e.g., macromolecular relaxations) or rare events (e.g., crystal nucleation). From a computational vantage point, there is scope for further development in efficient parallelization schemes for Monte Carlo simulations and development of specialized, inexpensive hardware for molecular simulations.(Lee et al. 2010; Shaw et al. 2008) Finally, for any scientific pursuit to make a big impact, it must win the confidence of stakeholders, which in the present case includes the pharmaceutical industry, medical professionals, and academic researchers. The realisation that the theories of statistical mechanics should explain the behavior of drug formulations may come naturally to a physicist but not others who tend to (and often rightly) believe in experimental observations more than theoretical predictions. Mathematical modelling in the area of drug delivery has so far been carried with the objective of explaining experimental findings and to extrapolate experimental results to larger populations. This is because the model parameters of continuum approaches need to be determined from experimental results usually by a fitting procedure. Thus, the paradigm that simulation predictions can precede or even direct systematic experiments need to be accepted and tried. More importantly, mutual co-operations between the industry and computational scientists working in this area can facilitate work in the areas where molecular simulations may make a huge impact.

CHAPTER 3

PHASE BEHAVIOR OF POLYACRYLIC ACID (PAA) OLIGOMERS IN AQUEOUS SOLUTIONS

3.1. INTRODUCTION

In this chapter, we present the results of fully atomistic molecular dynamics simulations of aqueous solutions of a weak, pH-responsive polyelectrolyte, polyacrylic acid (PAA). Model oligomers of PAA of different tacticities, molecular weights, degrees of deprotonation, and deprotonation patterns are simulated with water molecules. Deprotonation of PAA chains that occurs with an increase in pH results in an increase in Coulomb repulsion between chain segments on one hand, and a non-monotonic change in the hydrogen bonding between chain segments on the other hand. Consequently, at the single chain level, PAA chains are stretched at higher pH values, where the amount of stretching varies with chain tacticity. For the multiple chains case, PAA forms aggregates at higher concentrations, which are relatively denser and contain lesser water (solid-like) at lower pH than compared to higher pH (liquid-like). Phase behavior of polyacrylic acid (PAA) solutions using atomistic molecular dynamics simulations of model oligomers in different physiological pH conditions. Such phase transitions of PAA aggregates with pH has possible implications in the design of pH-responsive polyelectrolytes for applications in drug delivery.

3.2. SIMULATION METHODOLOGY

Simulations are performed in the GROMACS 4.6.7 simulation package (Groningen Machine for Chemical Simulation) (Pronk et al. 2013) using the CHARMM27 force field(Lindahl et al. 2010). PAA oligomers (chains) of different tacticities (*isotactic*, *syndiotactic*, *and atactic*) containing 20 monomers (repeating units) and various degrees of deprotonation and deprotonation patterns are constructed using GaussView 5(Dennington et al. 2016). Our choice of 20 repeat units is dictated by the fact that the contour length of the chain must be substantially smaller than the simulation box size to avoid periodicity artifacts. Although simulations of chains containing higher number of repeat units would have been more appropriate to understand the “polymer”-nature of PAA, computational cost of such simulations limited our choice. Two different kinds of deprotonation patterns are studied for partially ionized PAA. In random deprotonation, COO^- groups are randomly distributed on the PAA chain. In end deprotonation, $COOH$ groups are deprotonated starting from one end of PAA chain. PAA at different pHs, the number of COO^-

groups on the oligomer are determined using the Henderson-Hasselbalch equation using $pKa = 6.27$ (Spruijt, Cohen Stuart, and Van Der Gucht 2013), which are then randomly distributed on the PAA oligomer. The degree of deprotonation, f, is defined as the ratio of the number of COO^- groups to the number of repeating units. As an illustration, for $f = 0.05$, 1 out of 20 repeating units of PAA20 is randomly selected to contain COO^- group, and the other 19 repeating units contain a $COOH$ group. GROMACS compatible topologies of model oligomers for force calculations are generated using the automatic topology building tool Swiss Param(Zoete et al. 2011) (Molecular modelling group, Swiss Institute of Bioinformatics, Lausanne, Switzerland) (Pronk et al. 2013). Single chains and multiple chains (for various concentrations) of PAA are simulated with simple point charge (SPC) water in a cubic simulation box with periodic boundary conditions. Appropriate number of Na^+ counterions are added, as needed, to maintain the overall electroneutrality of the simulation box. The simulation box size (depends for all simulations) is significantly larger than the chain contour length ($\approx 5\ nm$) in order to avoid periodicity artefacts. The density of the simulation box is approximately 1 g/cc for all simulations.

Simulations have been performed in three steps. In the first step, energy minimization is performed using the steepest descent technique, with an initial step size of $0.001\ nm$ and adaptive step size control, until the maximum force on each atom become smaller than $10\ kJ/(nm \cdot mol)$. In the second step, MD equilibration is performed for $\sim 60\ ns$, beyond which the properties of interest converge around an average value. Finally, in the third step, MD production is performed for 5 ns with a typical sampling frequency of 0.5 ps. Both equilibration and production simulations are performed in the NVT ensemble with a reference temperature of 298 K. Nosé-Hoover thermostat is used for temperature control, with a coupling constant of 0.5 ps in both equilibration and production simulations. Electrostatic calculations are performed using the particle mesh Ewald (PME) scheme with a Fourier spacing of 0.1 nm, van der Waals cut-off of 1 nm, and cubic interpolation. Bonds containing hydrogen atoms are constrained using a fourth-order LINCS (Linear Constraint Solver) algorithm.

Number of oligomer-oligomer contacts with time, $N_p(t)$ (normalized by the total number of atoms of oligomers) is monitored to track the equilibrium process. Here, a "contact" is counted if any atom of any oligomer is within a chosen threshold distance ($0.6\ nm$) from any atom of another oligomer. Similar concept is used to obtain the fraction of "condensed" counterions (f_c) (Gerald S Manning 1969), which is defined as the total number of "contacts" between the oxygen atoms of COO^- groups and Na^+ counterions, divided by the total number of oxygen atoms of

COO^- groups. In this case, a "contact" is counted if any oxygen atom of any COO^- group is within a threshold distance of 0.22 nm from any Na^+ counterion. Please note that the choice of the above threshold distances are somewhat arbitrary due to inherent ambiguities in the definition of a "contact" or a "condensed counterion". The number of hydrogen bonds between the two species is defined as the number of donor-acceptor pairs that are within a threshold distance 0.35 nm and the hydrogen-donor-acceptor angle less than 30 degrees. Inter-molecular PAA-PAA radial distribution functions (RDFs), $g(r)$, are defined as the normalized probability of finding any atom of a PAA chain at a distance between r and $r + \delta r$ from any atom of another PAA chain, where bin width, $\delta r = 0.002\,nm$, and normalization is performed with such probability of an ideal gas. Radius of gyration (R_g) of PAA is computed in two ways – average R_g of individual chains and the R_g of all chains. While the former represents the size of individual chains, the latter represents the size of PAA aggregates. Water content of PAA aggregates are quantified by computing the R_g of all chains (entire PAA aggregate) and the solvent-accessible surface area(Eisenhaber et al. 1995) (SASA) computed using a 0.14 nm probe radius. A decrease in R_g of all chains signifies compaction of aggregates, i.e., an increase in the local density of aggregates ($\propto N/R_g^3, N$ being the total number of atoms in PAA chains). Equivalently, a decrease in SASA/monomer (SASA divided by the total number of monomers in PAA chains) indicates a decrease in water content or an increase in the compaction (local density) of aggregates(Athawale et al. 2007). Except $N_p(t)$, all the above quantities are time-averaged over trajectories sampled during production simulations.

3.3. RESULTS AND DISCUSSION

3.3.1. Single-Chain Simulations

In order to validate the force-field employed in our simulations, we first compare the results of single-chain simulations of atactic PAA solutions for different degrees of deprotonation (f) with that reported by Sulatha and Natarajan(Sulatha and Natarajan 2011). Unlike the other simulations reported in this work that uses the simulation protocol given above, we use the simulation protocol used in their study(Sulatha and Natarajan 2011) for these single-chain simulations. Since the actual tacticity patterns used in the simulations are not provided in their paper, we have performed the simulations for three different tacticity patterns (Tables B.1, B.2, B.3 in the Appendix B). We observe that the R_g averaged over the three chains increases with the increase in the degree of deprotonation (Figure B.1 in the Appendix B), though the magnitude of R_g

significantly vary for the three chains. Further, the typical chain conformations at different values of f show a transition from a collapsed to a stretched conformation with an increase in f (Figure B.2 in the Appendix B). All these results compare well with the results reported in their paper, but we do not attempt a direct comparison due to differences between tacticity patterns in the two studies. It is worth noting that the force-field employed in our study has also been used in a previous molecular dynamics study of PAA-PDMAEMA complexation.(Jha et al. 2014)

In order to investigate the effects of tacticity on the single-chain statistics in more detail, we have used a simpler terminology than a probably more appropriate terminology used by Suter and Neuenschwander 2005. We have not done a detailed analysis of the tacticity in our work and the current terminology is used for simplicity of representation. It is expected that the tacticity effect would be more pronounced for larger ones, not for the small oligomers simulated in our study, since we did not observe significant differences in phase behavior for polymers of different tacticities. We then perform single chain simulations for PAA of different tacticities (isotactic, syndiotactic, and atactic) for the neutral ($f = 0$) and fully deprotonated ($f = 1$) cases. As shown in Figure 3.1 and Table 3.1, while the PAA chains are always more stretched for the fully deprotonated case than compared to the neutral case, R_g for a given f varies with tacticity in the order syndiotactic > atactic > isotactic. This difference between R_g values for different tacticity is explained using the fact that all $COOH$ groups are on the same side of PAA chain in the isotactic case, and adjacent $COOH$ groups are on the opposite sides of PAA chain in the syndiotactic case. Therefore, the magnitude of short-ranged hydrophobic attraction for the neutral case is larger for isotactic PAA than compared to syndiotactic PAA, resulting in more collapsed conformations. If a similar reasoning is applied to the case of fully deprotonated chains, electrostatic repulsion should be higher in the isotactic case than compared to syndiotactic case, which would result in larger stretching in the isotactic case than compared to syndiotactic case. This is in contradiction with the observed result that syndiotactic PAA is more stretched compared to isotactic PAA at $f = 1$. It can be justified using the fact that the presence of COO^- groups on the same side of PAA chain in the isotactic case results in the bending of chain in order to keep the COO^- groups as far away as possible. Such bending is not favored in the syndiotactic case as the COO^- groups are on both sides of the chain, resulting in a straight chain. Yet another explanation for larger stretching in the syndiotactic case compared to the isotactic case is the difference in the magnitudes of counterion condensation in the two cases. Since the fraction of condensed counterions in the isotactic case is significantly higher than that in the syndiotactic case (Table

3.1), it would have relatively lower electrostatic repulsion between chain segments due to the charge screening effect of counterions. The former reason appears more convincing, given the relatively large differences in the values of R_g in the isotactic and syndiotactic cases. The mean R_g value of all tacticity at $f = 0$ and 1 is 1.05 and $1.18\, nm$. It is useful to compare these R_g values with their upper bound, that is, the theoretical estimate in the rodlike limit. The $C - C$ equilibrium bond distances along the backbone is $b_0 \approx 0.15\, nm$, which results in a theoretical estimate of $R_{g,rod} = 39 b_0/\sqrt{12} \approx 1.69\, nm$ in the rodlike limit(Teraoka 2002). As expected, all values of R_g shown in Table 3.1 are lower than $R_{g,rod}$ and maximum R_g is obtained for $f = 1$ case of syndiotactic PAA that has most stretched configuration (Figure 3.1d) in Figure 3.1.

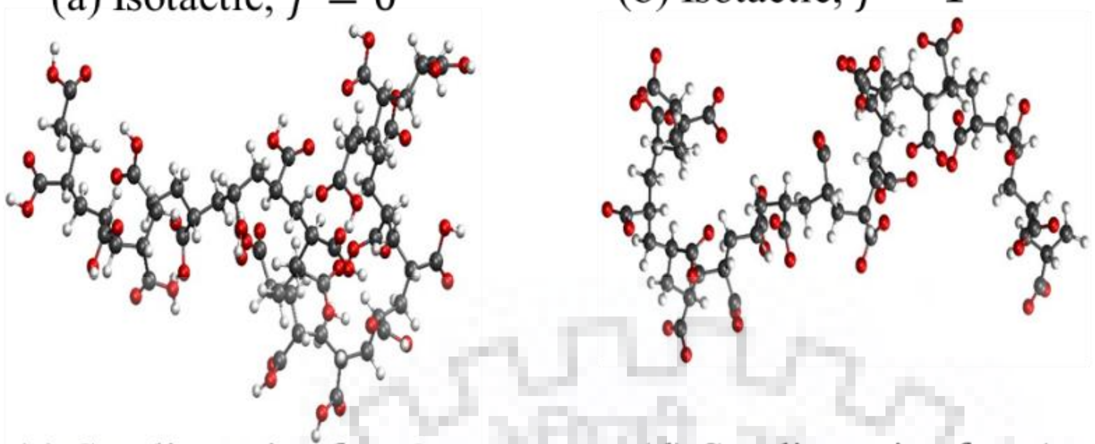

(a) Isotactic, $f = 0$

(b) Isotactic, $f = 1$

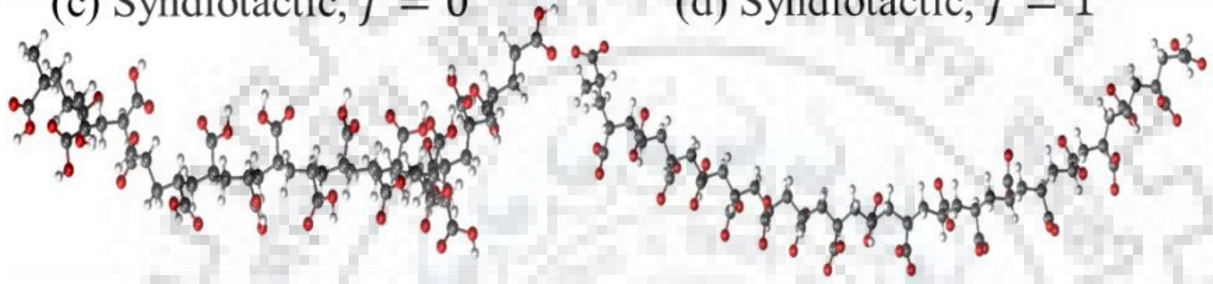

(c) Syndiotactic, $f = 0$

(d) Syndiotactic, $f = 1$

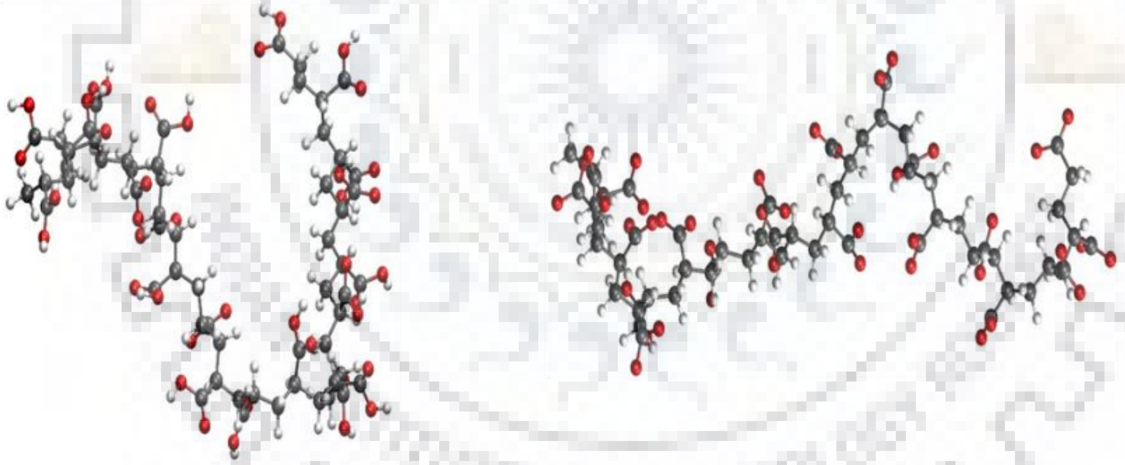

(e) Atactic, $f = 0$

(f) Atactic, $f = 1$

Figure 3.1 Typical single chain conformations of PAA for neutral and fully deprotonated cases for three types of tacticity: (a)-(b) isotactic, (c)-(d) syndiotactic, (e)-(f) atactic PAA chain. Carbon, oxygen, and hydrogen atoms in PAA are shown in grey, red, and white colors, respectively. Water molecules and counterions are not shown.

Table 3.1 Comparison of R_g values of neutral ($f = 0$) and fully deprotonated states ($f = 1$) of single PAA chain of different tacticity. Fraction of "condensed" counterions (f_c) is also shown for the $f = 1$ case. The values in brackets are the standard deviation of the last decimal.

Tacticity	$\boldsymbol{f = 0}$	$\boldsymbol{f = 1}$	
	R_g (nm)	R_g (nm)	f_c
Isotactic	0.83(4)	0.97(1)	0.28(6)
Syndiotactic	1.26(7)	1.42(2)	0.20(6)
Atactic	1.06(1)	1.16(1)	0.27(6)

3.3.2. Multiple-Chain Simulations

Four different concentrations of PAA are simulated by varying the number of PAA chains in a simulation box of 6 nm size containing SPC water. PAA concentration in the four systems, defined in moles per liter (M) of monomers are: (a) 0.615 M (4 PAA chains), (b) 1.223 M (8 PAA chains), (c) 2.456 M (16 PAA chains), and (d) 3.689 M (24 PAA chains).

$$Concentration = \frac{Total\ number\ of\ monomers}{Avogadro\ number \times volume\ of\ box}$$

To decide the amount of equilibration time required for the simulations, we monitor the number of oligomer-oligomer contacts with time, which appear to converge after 60 ns, as established by simulations performed for a longer time of 90 ns in Figure 3.2 for the neutral syndiotactic case. Equilibration times of this order had also been reported in earlier atomistic simulation studies on polymer aggregation for systems of similar sizes.(Huang et al. 2016a, 2014; Jha and Larson 2014) Note that our estimate of equilibrium time is based on simulations performed over significantly long time permitted within the current computational capabilities of atomistic simulations. The possibility of further aggregation or crystallization occurring over time scales that are much longer than that permitted by existing computational capabilities (e.g., time scales higher than 1 μs) can neither be established nor be ruled out. Interestingly, PAA aggregates span the simulation box after equilibration in Figure 3.2, which at first glance, appear to be an artefact of periodic boundary condition used in our simulations. However, since the chain contour length is significantly smaller than the box size, PAA spanning the simulation box is less likely to be a periodicity artifact, and is more likely to be reminiscent of a “gel”-like structure reported in a previous study(Jha and Larson 2014).

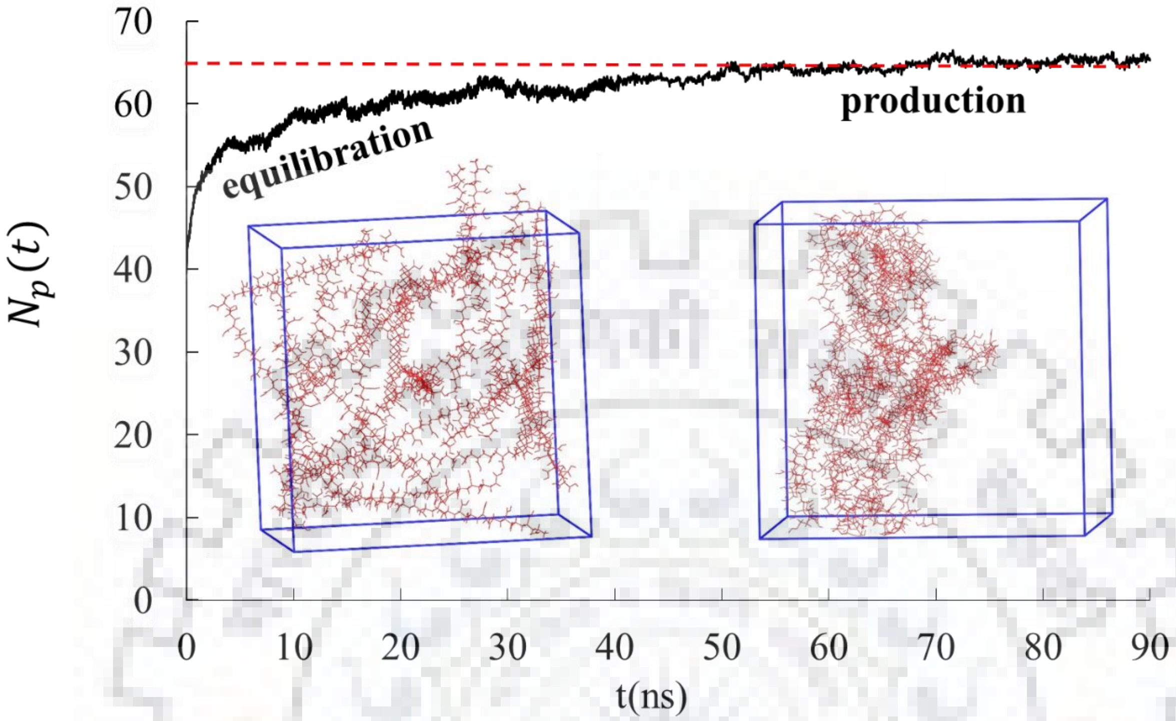

Figure 3.2 Number of oligomer-oligomer contacts with time for neutral syndiotactic PAA of concentration 3.689 M. Red dotted line indicate the convergence of oligomer-oligomer contacts around an average value. Simulation snapshots at the start of simulations (left) and after equilibration (right) are also shown. PAA chains are shown in red color; water molecules are not shown.

Next, we compare the aggregation behavior of PAA of different tacticity for the neutral and fully deprotonated cases. As expected, neutral cases for all tacticities formed more compact aggregates than compared to the fully deprotonated cases, as evidenced by larger intermolecular RDF peaks for the neutral cases in Figure 3.3. However, the difference between the RDF for different tacticities at a given f are not as substantial as the difference in R_g of single-chains for different tacticities (Table 3.1). This is because the $COOH$ groups of a PAA chain in an aggregate interact not only with the $COOH$ groups on the same chain, but also with $COOH$ groups on other PAA chains, which in turn may be oriented in any direction with respect to the PAA chain. Therefore, changes in the single-chain conformations due to tacticity play little role in determining the aggregation behavior. It is worth pointing out that the first peak around $r \sim 0.2\, nm$ for the neutral case in Figure 3.3 is due to hydrogen bonding between $COOH$ groups. Roughly, ~ 0.25 $COOH - COOH$ hydrogen bonds/monomer were observed for all tacticities. This peak is absent for the fully deprotonated cases, as the COO^- groups do not hydrogen bond. The second peak occurring around $r \sim 1\ nm$ represent an aggregation length scale of the order of R_g (Table 3.1). This peak is much broader for the neutral case than compared to the fully deprotonated case, implying more PAA aggregation in the neutral case.

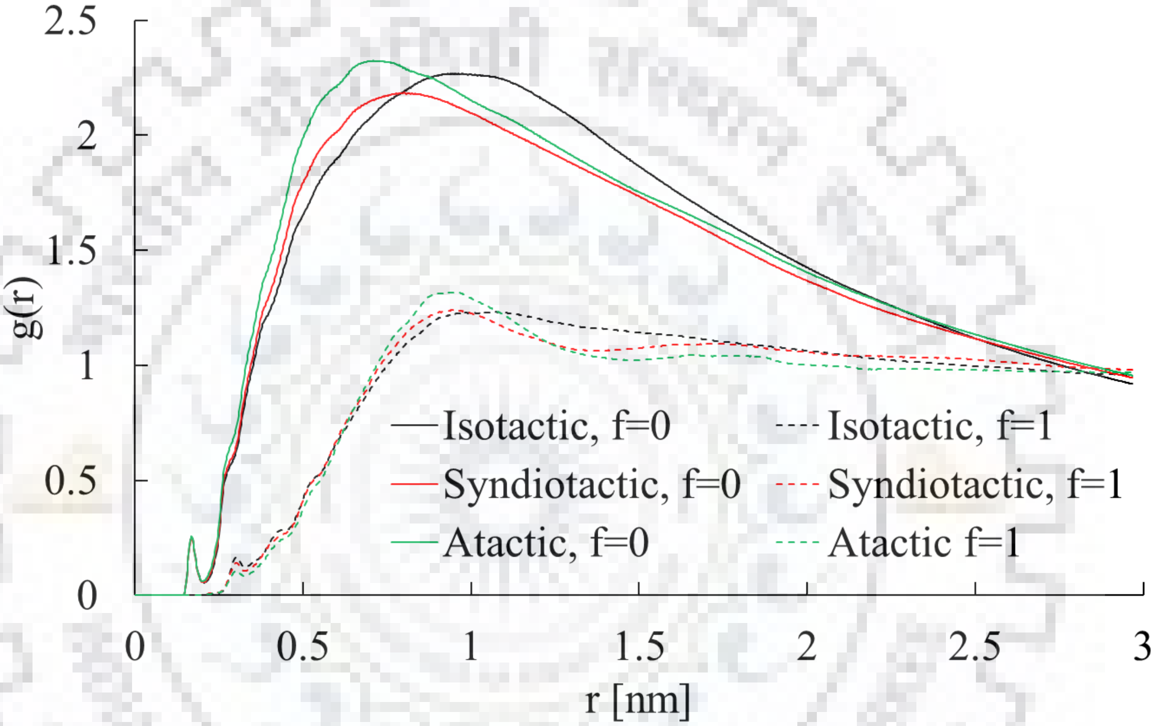

Figure 3.3 Intermolecular PAA-PAA RDF for neutral ($f = 0$) and fully deprotonated ($f = 1$) PAA of different tacticities at a concentration of 3.689 M.

Figure 3.4 shows the equilibrium configurations of syndiotactic PAA chains at various concentrations for $f = 0.4$ with random deprotonation (Table B.4 in the Appendix B). As expected, aggregation increases with increase in PAA concentration. Although the counterions have higher mobility than compared to PAA, they mostly reside within the PAA aggregate, thus neutralizing its overall charge. Further, when compared to $f = 0$ case in Figure 3.2 (Figure 3.4d has the same concentration as Figure 3.2), the aggregate appears less compact. The effect of PAA concentration on the aggregation behavior is quantified in terms of several measurable parameters in Table 3.2. The average R_g of individual chains increases with increase in PAA concentration, implying an increase in the stretching of individual chains. On the other hand, the overall R_g of all chains first increases (until 2.456 M in Table 3.2) and then decrease (for 3.689 M in Table 3.2). The initial increase in R_g can be attributed to an increase in the size of PAA aggregates with increase in the number of PAA chains, and the final decrease (after $R_g \approx 3\ nm$) can be understood to result from the compaction of aggregates. Although the R_g values show a slightly non-monotonic trend with concentration, the local density of aggregates ($\propto N/R_g^3$, N being the total number of atoms in PAA chains) increases uniformly with increase in concentration. This is further confirmed by the fact that the water content of aggregate, characterized by the SASA/monomer roughly decreases with increase in concentration, with small anomaly at the two intermediate concentrations where the SASA/monomer is nearly same.

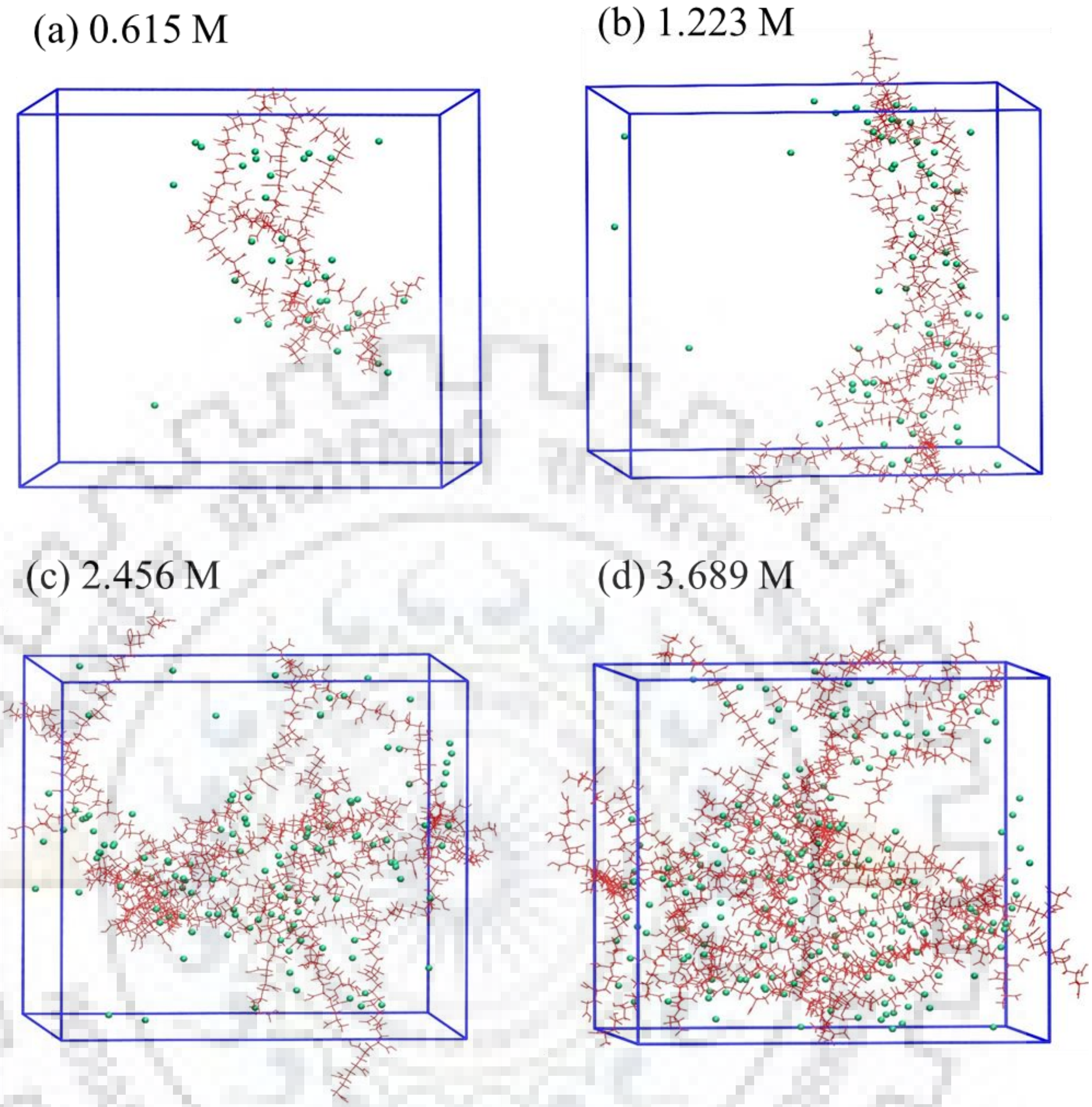

Figure 3.4 Simulation snapshots (after equilibration) of syndiotactic PAA with $f = 0.4$ for different concentration with random deprotonation (Table B.4 in the Appendix B). PAA chains and counterions are shown in red and green colors, respectively; water molecules are not shown.

Table 3.2 Radius of gyration (for single chain and all chains), SASA/monomer, and fraction of condensed ions, of syndiotactic PAA with $f = 0.4$ for different concentration with random deprotonation (Table B.4 in the Appendix B). The values in brackets are the standard deviation of the last decimal.

PAA Concentration	**R_g (nm)**		**SASA/monomer (nm^2)**	**f_c**
	Individual chains	All chains		
0.615 M	1.05 (2)	2.0(4)	0.65(1)	0.26(5)
1.223 M	1.185(9)	2.8(2)	0.567(6)	0.30(4)
2.456 M	1.296(5)	3.06(6)	0.573(6)	0.32(3)
3.689 M	1.309(3)	2.68(3)	0.542(4)	0.32(2)

The effect of f on PAA aggregation behavior is more clearly demonstrated in Figure 3.5, which shows that the compaction of PAA aggregate decreases with increase in f. Electrostatic repulsion between PAA chains increases with increase in f resulting in the formation of less compact structures. This is further confirmed by a monotonic increase in SASA/monomer with an increase in f at the given concentration (Table 3.3). Such monotonic trend is not observed in the R_g of individual chains and R_g of all chains in Table 3.3. However, roughly speaking, both the R_g of individual chains increases and R_g of all chains increases with increase in f, signifying an increase in the stretching of individual chains and a decrease in overall compaction of aggregates, respectively.

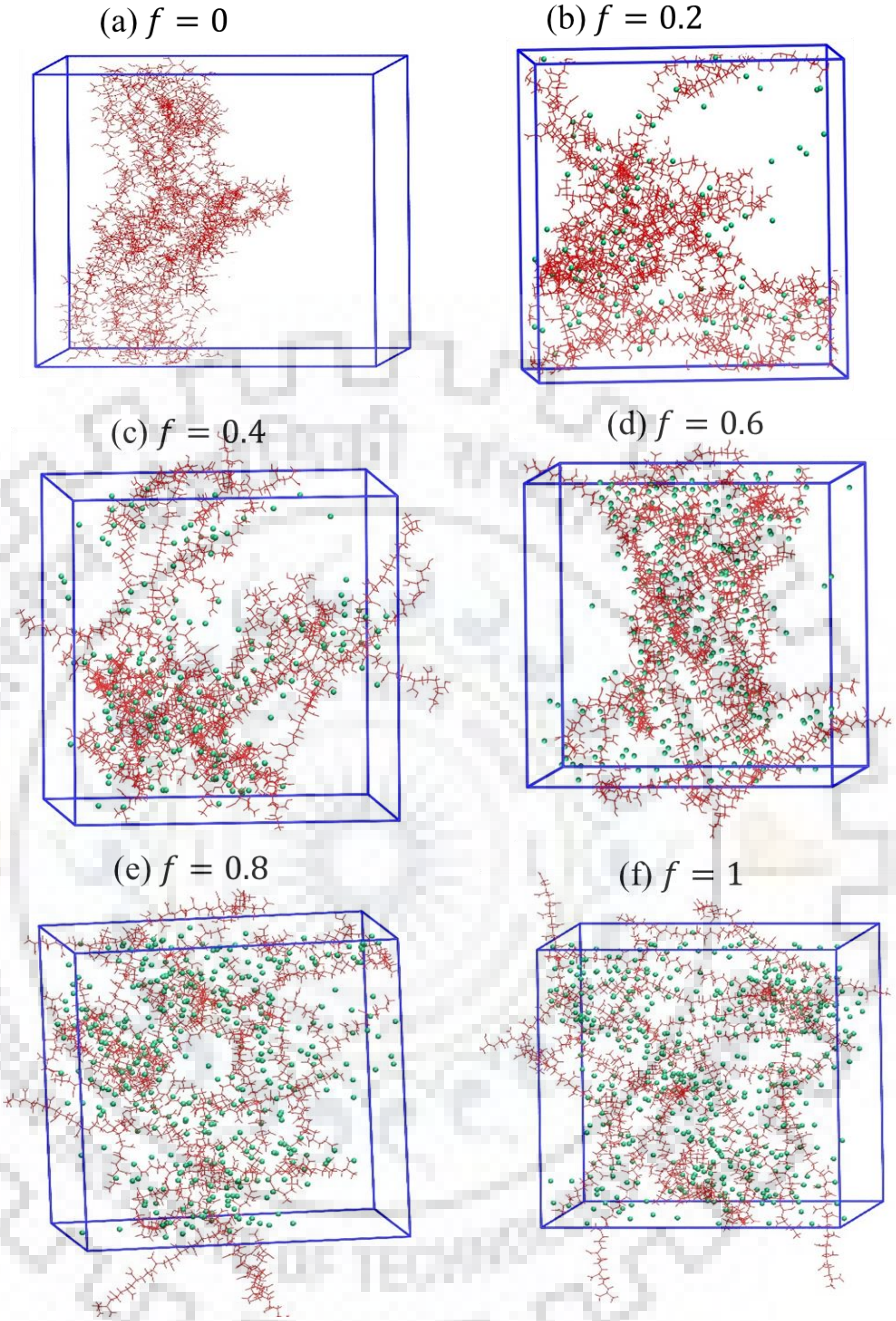

Figure 3.5 Simulation snapshots (after equilibration) for syndiotactic PAA of concentration 3.689 M for different values of f with random deprotonation (Table B.4 in the Appendix B). PAA chains and counterions are shown in red and green colors, respectively; water molecules are not shown.

Table 3.3 Radius of gyration (for single chain and all chains), SASA/monomer, and fraction of condensed ions, of syndiotactic PAA at different degrees of deprotonation with random deprotonation (Table B.4 in the Appendix B). The values in brackets are the standard deviation of the last decimal.

f	R_g (nm)		SASA/monomer (nm^2)	f_c
	Individual chains	All chains		
0	1.272(5)	2.66(4)	0.375(4)	-
0.2	1.268(4)	2.76(5)	0.511(4)	0.19(2)
0.4	1.309(3)	2.68(3)	0.542(4)	0.32(2)
0.6	1.342(2)	2.70(1)	0.569(4)	0.39(2)
0.8	1.320(3)	2.91(4)	0.603(3)	0.43(2)
1.0	1.357(2)	2.99(1)	0.651(3)	0.45(2)

More information about the structure of PAA aggregates is revealed by the intermolecular PAA-PAA RDF (Figure 3.6). Second peak of this RDF occurring around $\sim 1\ nm$ is higher and broader for smaller values of f indicating an increase in PAA aggregation, as already observed in Figure 3.5. However, the first peak occurring around $\sim 0.15\ nm$ (inset of Figure 3.6) do not exhibit the same trend due to rather non-monotonic changes in intermolecular hydrogen-bonding with f. While COO^- cannot hydrogen bond with COO^-, it can hydrogen bond with $COOH$, which contribute to the first peak along with $COOH - COOH$ hydrogen bonding. In the extreme case of fully deprotonated chain ($f = 1$ case in Figure 3.6), the first peak is missing as there is no possibility of hydrogen bonding between COO^- groups. For partially ionized cases ($f = 0.2, 0.4, 0.6, 0.8$ case in Figure 3.6), we observe a peak at $r \approx 0.16\ nm$ due to the combined effect of hydrogen bonding between COO^- and $COOH$ groups, along with $COOH - COOH$ hydrogen bonding. In the other extreme of a neutral chain ($f = 0$ case in Figure 3.6), the first peak occurs at a slightly larger value of $r \approx 0.17\ nm$ as the COO^- groups are not present. The hydrogen bonding data in Table 3.4 shows that the $COOH - COOH$ hydrogen bonding decreases with f

due to a reduction in the number of $COOH$ groups. On the other hand, $COO^{-} - COOH$ hydrogen bonding first increases and reaches a maximum at an intermediate value of f, followed by a decrease at even higher value of f. This is because the number of possible $COO^{-} - COOH$ pairs is maximum at an intermediate f value.

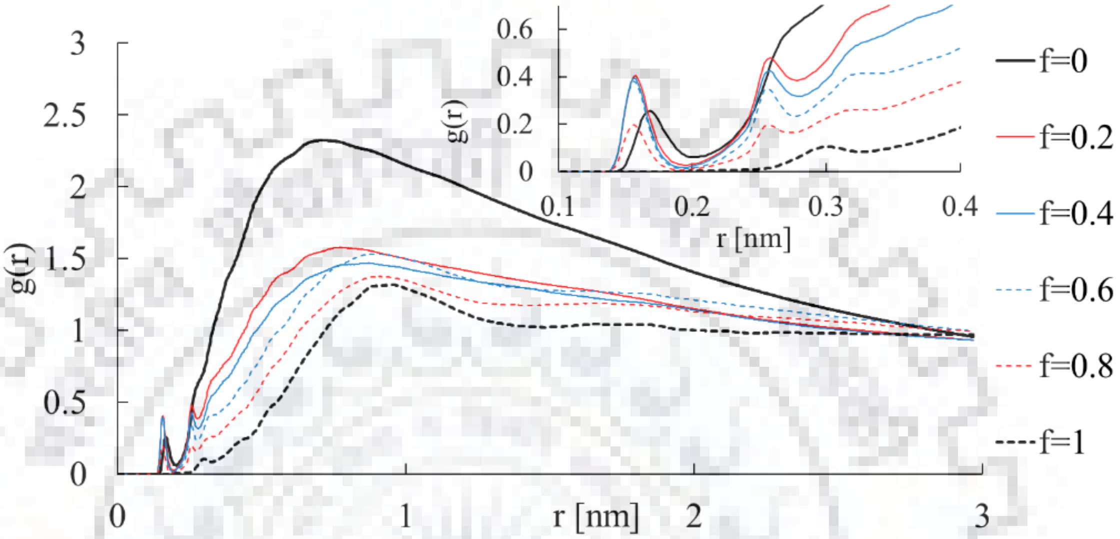

Figure 3.6 Intermolecular PAA-PAA RDF for syndiotactic PAA of 3.689 M concentration for different values of f with random deprotonation. $g(r)$ for small values of r are shown in the inset.

Table 3.4 Hydrogen bonding per monomer for syndiotactic PAA of different concentration for different f with random deprotonation. The values in brackets are the standard deviation of the last decimal. Values < 0.01 are not reported, since the standard deviation becomes comparable or higher than the mean.

f	**0.615 M**		**1.223 M**		**2.456 M**		**3.689 M**	
	COO^- and $COOH$	$COOH$ and $COOH$	COO^- and $COOH$	$COOH$ and $COOH$	COO^- and $COOH$	$COOH$ and $COOH$	COO^- and $COOH$	$COOH$ and $COOH$
0	–	0.05(3)	–	0.19(1)	–	0.25(2)	–	0.22(1)
0.2	0.13(1)	0.01(1)	0.18(1)	0.05(1)	0.23(1)	0.04(1)	0.24(1)	0.05(1)
0.4	0.18(2)	0.03(1)	0.21(1)	0.02(0)	0.22(1)	0.02(1)	0.25(1)	< 0.01
0.6	0.17(1)	< 0.01	0.20(1)	< 0.01	0.19(0)	< 0.01	0.21(1)	< 0.01
0.8	0.12(1)	< 0.01	0.07(1)	< 0.01	0.08(0)	< 0.01	0.11(0)	< 0.01

Further insight into the intermolecular interactions can be obtained by a closer inspection of two nearby PAA chains in the concentrated system. Figures 3.7a-c show the zoomed view of simulation snapshots of the Figures 3.5a, 3.5c, and 3.5f, for the neutral, partially deprotonated ($f = 0.4$), and fully deprotonated cases, respectively. As evident from Figure 3.7, the distance between PAA chains at a given concentration increases with an increase in f due to an increase in electrostatic repulsion (or a decrease in hydrophobic attraction) between PAA chains. However, as noted above, hydrogen bonding between COO^- and $COOH$ groups in the partially ionized case (Figure 3.7b) works together with $COOH - COOH$ hydrogen bonding, resulting in substantial attraction between PAA chains. Finally, while such hydrogen bonding is absent in the fully deprotonated case (Figure 3.7c), segments of PAA chain can still show an effective attraction due to "counterion bridging" as the Na^+ counterions sandwiched between the two PAA chains experience electrostatic attraction from both the PAA chains. The likelihood of counterion bridging increases with increasing either the concentration or the degree of deprotonation of PAA as the fraction of condensed ions (f_c) increases both with increasing concentration (Table 3.2) and with increase in f (Table 3.3). However, this "counterion bridging" (or "salt-bridging") (Bulo et al. 2007) effect is much weaker compared to hydrogen bonding interactions as the counterions have high entropy and prefers to disperse in the solution. Therefore, PAA chains are mostly separated from each other in the fully ionized case (Figure 3.5f).

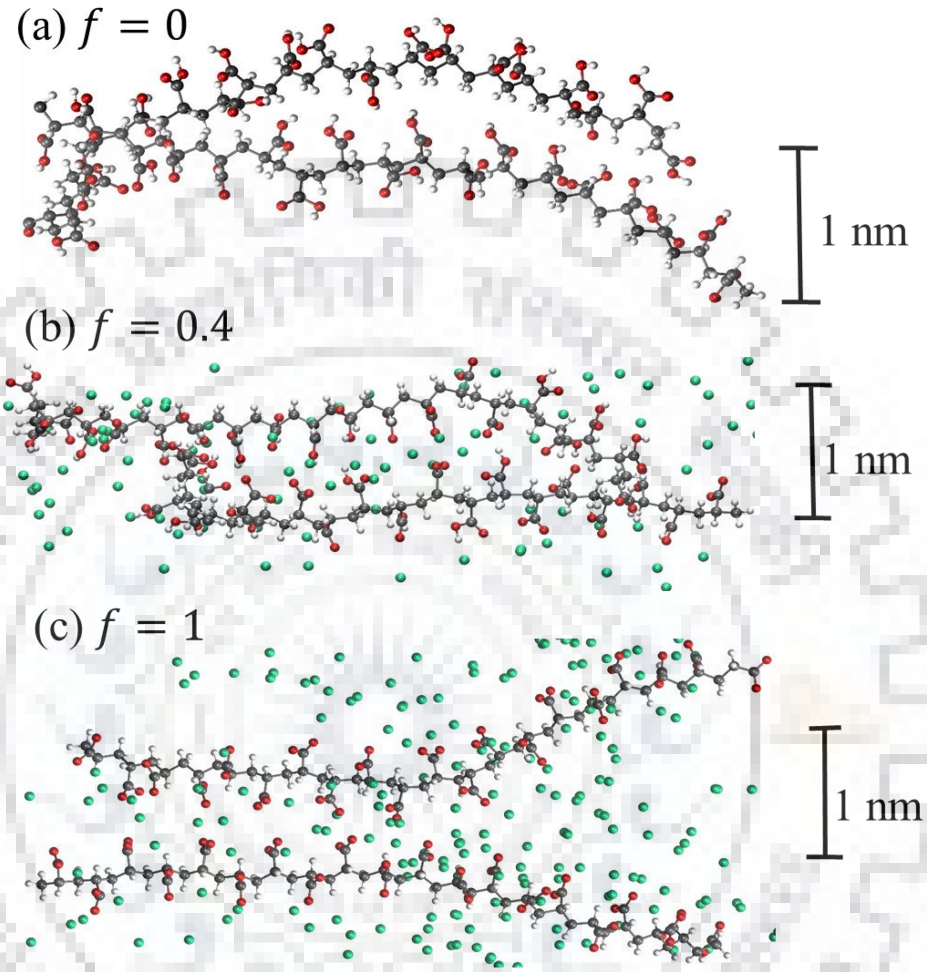

Figure 3.7 Zoomed view of simulation snapshot for syndiotactic PAA of 3.689 M concentration for different values of f with random deprotonation, showing the typical interactions between two nearby chains. Average distance between the center of mass of chains are $2.31 \pm 0.02\, nm$, $2.60 \pm 0.02\, nm$ and $3.20 \pm 0.01\, nm$ for $f = 0$, 0.4, and 1, respectively. Carbon, oxygen, and hydrogen atoms in PAA are shown in grey, red, and white colors, respectively. Counterions are shown in green color. Water molecules are not shown.

Next, we compare the aggregation behavior of the partially deprotonated case for random deprotonation and end deprotonation at the same concentration. As shown in Figure 3.8(a) and 3.8b, the overall aggregation behavior appear similar. This is further confirmed by the comparison of their intermolecular PAA-PAA RDF in Figure 3.8c. However, the dense regions formed by the hydrogen bonding of $COOH$ groups is more populated and prominent in the end deprotonation case (Figure 3.8b) compared to the random deprotonation case (Figure 3.8a). In fact, for realistic chains (much longer than the oligomers studied here), a micelle-like formation (appearance of a dense core of hydrophobic segments) is expected in the end deprotonation case due to the hydrogen bonding between the protonated ends of chains. On the other hand, a network-like(Hamer et al. 2014) formation with no such dense core is expected in the random deprotonation case of realistic chains, as the protonated groups are randomly distributed along the chains. Such differences will however be only apparent at intermediate values of f (e.g., $f = 0.2$ or 0.4). At lower (higher) values of f, most of the chain is hydrophobic (hydrophilic) resulting in the formation of a dense precipitate (dilute solution). This can be substantiated by comparing the magnitudes of SASA/monomer for the random deprotonation case (Table 3.3) and end deprotonation case (Table 3.5). SASA/monomer magnitudes are significantly lower for the end deprotonation case than compared to the random deprotonation case for $f = 0.2$ and 0.4, which implies the formation of denser structures in the end deprotonation case. However, the system size and the length of chain is not sufficient enough to obtain a clear distinction of micelle-like and network-like structures.

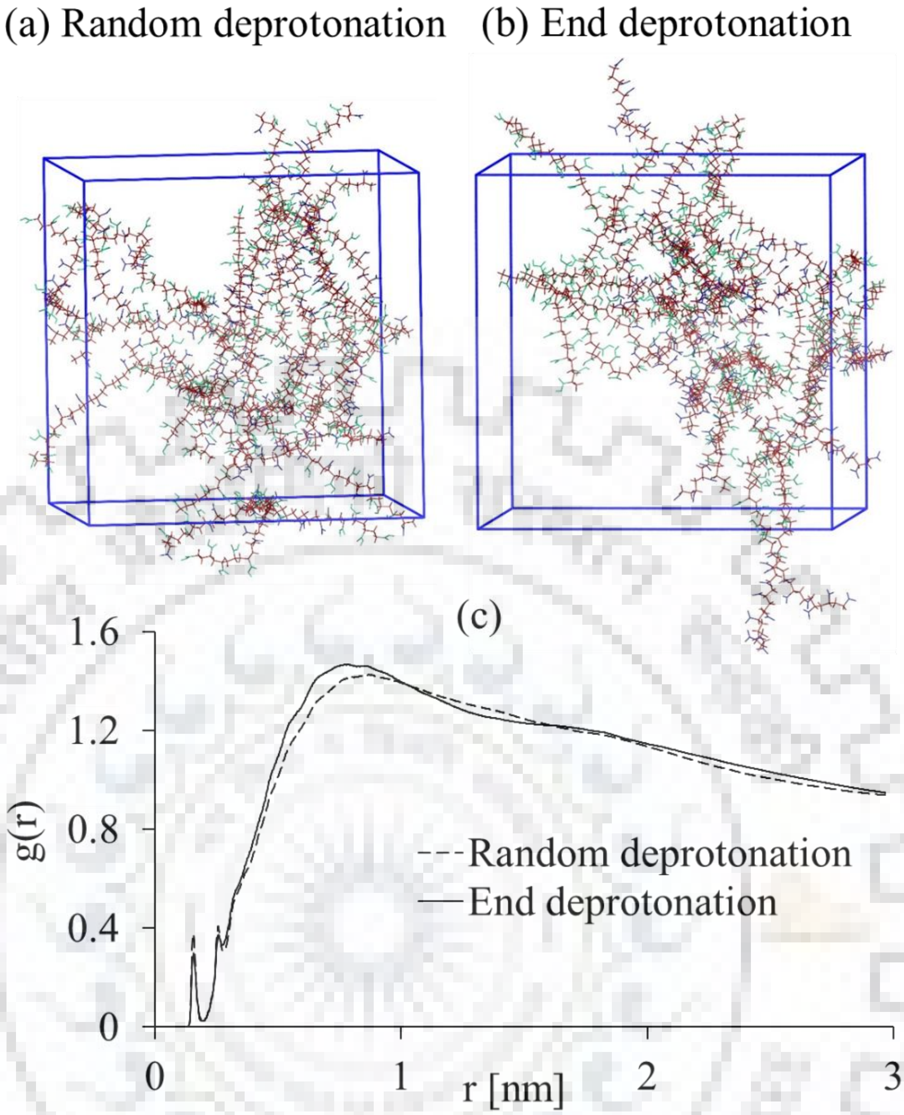

Figure 3.8 Simulation snapshot of syndiotactic PAA of 3.689 M concentration for (a) random deprotonation (Table B.4 in the Appendix B) and (b) end deprotonation (Table B.5 in the Appendix B , at fixed $f = 0.4$, Water molecules and counterions are not shown here; aliphatic backbone carbon, COO^- group, and $COOH$ group are shown in red, blue, and green color, respectively. (c) Intermolecular PAA-PAA RDF for random (dashed line) and end deprotonation (bold line).

Table 3.5 Radius of gyration (for single chain and all chains), SASA/monomer (hydrophobic, hydrophilic, and total), and fraction of condensed ions, of syndiotactic PAA at different degrees of deprotonation with end deprotonation (Table B.5 in the Appendix B). The values in brackets are the standard deviation of the last decimal.

f	R_g (nm)		SASA/monomer (nm^2)	f_c
	Individual chains	All chains		
0	1.272(5)	2.66(4)	0.375(4)	-
0.2	1.258(5)	2.83(7)	0.467(4)	0.28(3)
0.4	1.271(4)	2.96(6)	0.522(4)	0.38(2)
0.6	1.331(3)	2.79(4)	0.585(3)	0.41(2)
0.8	1.339(3)	2.60(3)	0.624(4)	0.42(2)
1.0	1.357(2)	2.99(1)	0.651(3)	0.45(2)

The differences in phase behavior observed with changes in f (Figure 3.5) and deprotonation pattern (Figure 3.7) has important implication in the use of polyelectrolytes as stimuli-responsive materials for various applications. For example, for pH-responsive polyelectrolytes used as drug carriers, it is critical to attain substantial change in the drug release rate with change in pH. This can be realized due to an increase in the drug diffusivity within the carrier with a decrease in polyelectrolyte volume fraction, or equivalently, an increase in the water volume fraction. The water content of the PAA aggregates can be estimated by the solvent-accessible surface area (SASA). In figure 3.9, we plot the SASA normalized by its value at $f = 0$ (measure of change in water content with f) against f. As shown in the plot, SASA changes by ~ 3 times in the entire range of f, which should give rise to substantial change in the drug diffusivity within the aggregate with pH.

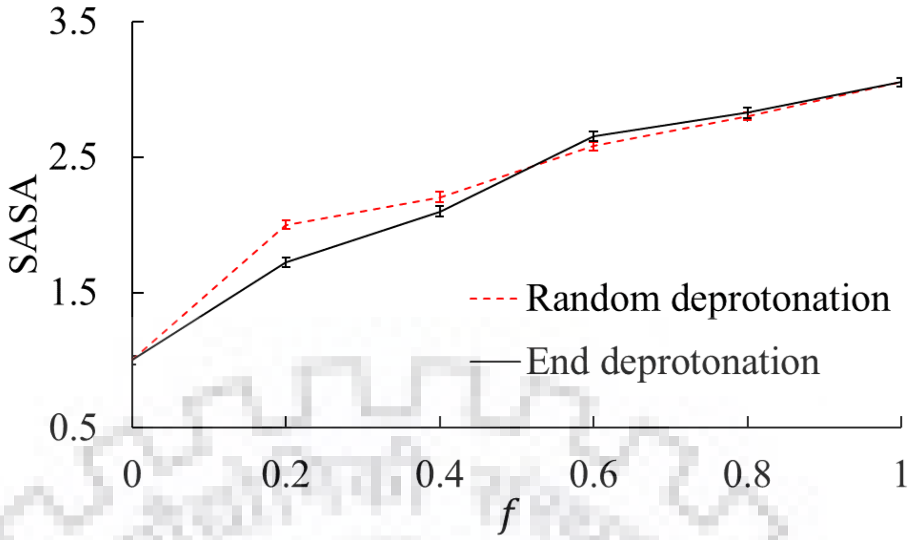

Figure 3.9 Solvent accessible surface area (SASA) divided by its value at $f = 0$ against f for random deprotonation and end deprotonation cases for syndiotactic PAA of 3.689 M concentration.

3.4. SUMMARY

The results of atomistic MD simulations provide a detailed molecular picture of the PAA aggregation behavior as a function of the degree of deprotonation or pH. PAA aggregation increases with PAA concentration and an increase in its degree of deprotonation (pH). Further, the nature of aggregation depends on the deprotonation pattern; end deprotonation and random deprotonation showed the formation of micelle-like and network-like aggregates, respectively. Interactions that were found relevant to the aggregation behavior included the hydrogen bonding between $COOH - COOH$ and $COO^- - COOH$ groups, electrostatic repulsion between COO^- groups, and counterion (Na^+) bridging between the COO^- groups. Finally, the water content of aggregates expressed in terms of solvent-accessible surface area showed a 3-fold increase between the neutral and fully deprotonated limits.

भारतीय प्रौद्योगिकी संस्थान रुड़की
INDIAN INSTITUTE OF TECHNOLOGY ROORKEE

CHAPTER 4

THE EFFECTS OF MEDIA INTERACTIONS ON pH-RESPONSIVE DRUG CARRIERS

4.1. INTRODUCTION

In this chapter, we discuss all atom Molecular Dynamics (MD) simulations of polyacrylic acid (PAA) oligomers, considered as a model pH-responsive carrier in biological fluids representative of gastric and intestinal condition. Multiple oligomers of PAA are simulated in model gastric and intestinal fluids, where the degree of deprotonation of PAA oligomers vary with the medium pH. Since the gastric fluid has a pH substantially lower than intestinal fluid, PAA is relatively lesser ionized in gastric fluid and forms aggregates. As discussed here, the change in PAA aggregation with the pH shows the trend similar to observed in our earlier study of PAA chains simulated in water. However, some of the components of gastric and intestinal fluids contribute towards the hydrogen bonding behavior.

4.2. SIMULATION METHODOLOGY

The simulation method employed in this study is similar to the one used in our previous study of PAA oligomers in water at different pH discussed in the previous chapter and is discussed briefly here. MD simulations are performed using the GROMACS compatible molecular topologies of model syndiotactic PAA oligomers containing 20 repeating units (henceforth referred as PAA20), DOX (uses in next chapter), and components used in simulated biological fluids (Figure 4.1) are generated using the automatic topology building tool SwissParam (Zoete et al. 2011), after the initial structures are created in GaussView 5. Table 4.1 contains the details of the simulations set 1 in this chapter and set 2 for next chapter. It is worth nothing that the inclusion of various components of gastric/intestinal fluids at realistic concentration(Marques, Loebenberg, and Almukainzi 2011) in this results in a requirement of large simulation box size to be able to accommodate a statistically significant (>10) number of molecules of each component. Several other components of gastric and intestinal fluids that would have <10 molecules the box size of 10 nm are not included, since statistical averaging over very few molecules of a component in the simulation box is not likely to provide reliable statistics.

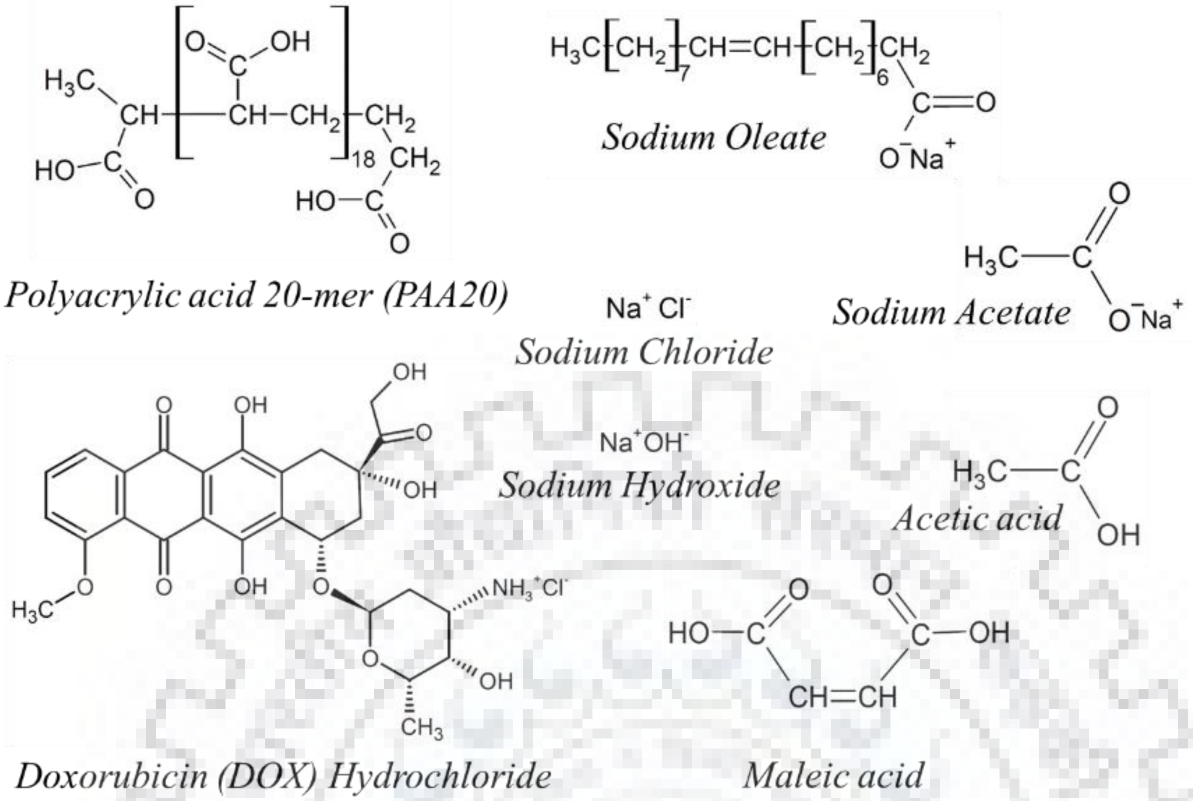
Polyacrylic acid 20-mer (PAA20)
Sodium Oleate
Sodium Acetate
Na+ Cl-
Sodium Chloride
Na+OH-
Sodium Hydroxide
Acetic acid
Doxorubicin (DOX) Hydrochloride
Maleic acid

Figure 4.1 Chemical structures of compounds simulated in this study.

Table 4.1 Systems simulated in this study. The composition of FaSSGF, FeSSGF, and FeSSIF are taken from literature (Marques et al. 2011) and components with less than 10 molecules in the simulation box size (10 nm) are not included, since statistical averaging over very few molecules of a component in the simulation box is not likely to provide reliable statistics.

Set	**Medium**	**Component Name**	**Box size (nm)**	**Number of molecules**	**Concentration (M)**	**pH**
1	**Fa**sted-**S**tate **S**imulated **G**astric **F**luid (FaSSGF)	PAA20, $f = 0$	10	74	0.123	1.6
		Sodium chloride		21	0.035	
	Fed- **S**tate **S**imulated **G**astric **F**luid (FeSSGF)	PAA20, $f = 0.05$	10	74	0.123	5
		Sodium chloride		143	0.237	
		Acetic acid		10	0.017	
		Sodium acetate		18	0.03	
	Fed- **S**tate **S**imulated **I**ntestinal **F**luid (FeSSIF)	PAA20, $f = 0.25$	10	74	0.123	5.8
		Sodium chloride		74	0.123	
		Maleic acid		27	0.045	
		Sodium hydroxide		39	0.065	
		Sodium oleate		18	0.03	
2	Water	PAA20, $f = 0,0.05,0.25,0.6,0.85$	6	16	0.123	1.6, 5, 5.8, 6.5, 7
		DOX		50	0.384	

MD simulations involve an energy minimization step, followed by MD equilibration performed for $\sim 50\,ns$, and MD production performed for additional $30\,ns$ with a typical sampling frequency of $80\,ps$. Both equilibration and production simulations are performed in the NVT ensemble with a reference temperature of 298 K. Number of PAA20-PAA20 contacts with time are monitored to track the equilibration time, where a “contact” is counted if any atom of molecules of one species is within a chosen threshold distance ($0.6\,nm$) from any atom of molecules of another species. We observed that beyond $\sim 50\,ns$ equilibration, the number of contacts converged to an average value, as shown in Figure 4.2.

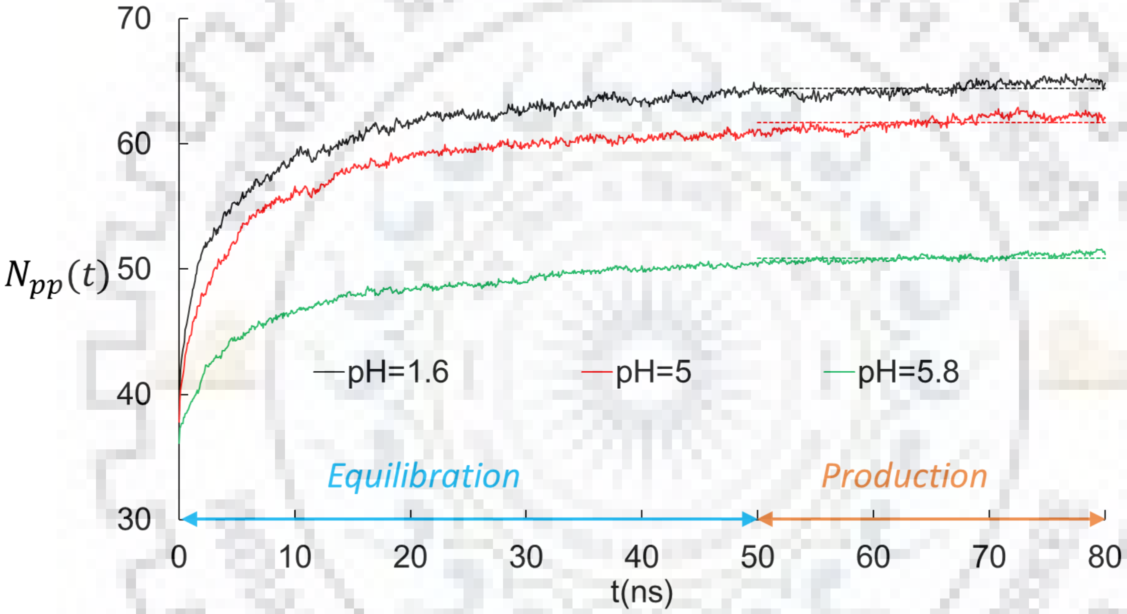

Figure 4.2 Profiles of normalized number of PAA20-PAA20 contacts against time. All the simulations details are in Table 4.1. $N_{pp}(t)$ is normalized by the total number of atoms of all PAA20 chains. After 50 ns of equilibration run, all of these profiles converged around average values indicated by dashed lines in the figure.

4.3. RESULTS AND DISCUSSION

Figure 4.3 shows the simulation snapshots after equilibration. Results obtained in simulation show close similarity with the results of study of PAA in water discussed in the previous chapter, where we studied the effect of PAA molecular weight, degree of deprotonation (f), deprotonation patterns, and tacticity. In that study, we had only considered the effect of degree of deprotonation (f). Three competing changes occur with an increase in solution pH (or equivalently, an increase in f): (1) electrostatic repulsion between PAA segments increases, (2) $COOH - COOH$ hydrogen bonding decreases, and (3) $COO^{-} - COOH$ hydrogen bonding first increases and then decreases. The second and third of these changes also involve the components of gastric/intestinal fluids included in this study that contains COO^{-} or $COOH$ group, which are maleic acid, acetic acid, acetate ion and oleate ion. Interactions of PAA20 with other ions present in gastric/intestinal fluid can be interpreted a balance of Coulombic interactions and entropy. That is, PAA20 repels oppositely charged chloride and hydroxyl ions, and attracts sodium ions, but a majority of these ions prefers to be dissolved than being condensed on PAA20 backbone. In general, however the overall PAA20 aggregation behavior is dominated by the electrostatic repulsion of PAA20 segments alone, since PAA20 aggregation decreases with an increase in pH (increase in f), as also evident from the decrease in the final average value of $N_{pp}(t)$ with increase in pH in Figure 4.2.

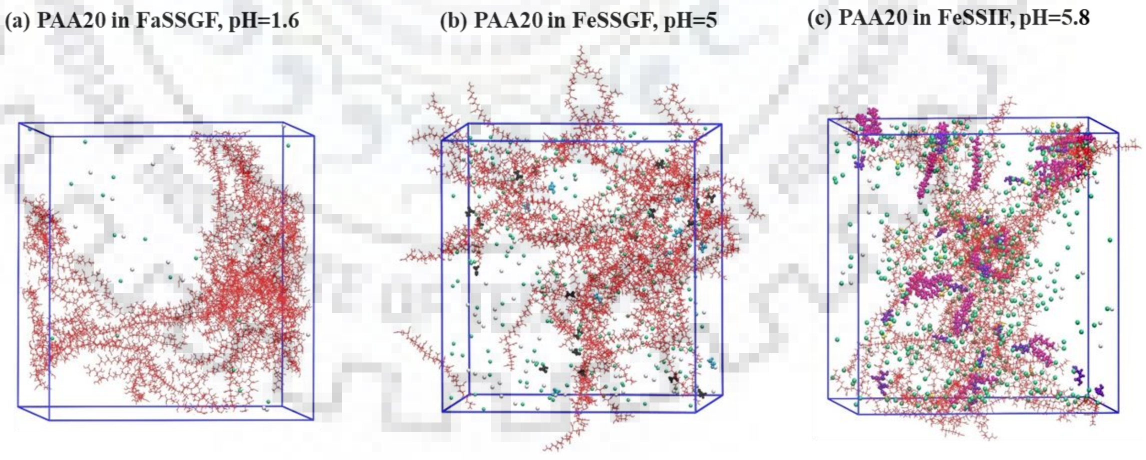
(a) PAA20 in FaSSGF, pH=1.6
(b) PAA20 in FeSSGF, pH=5
(c) PAA20 in FeSSIF, pH=5.8

Figure 4.3 Simulation snapshots (after equilibration) for systems described in Table 4.1. Colour scheme: PAA20 (red), sodium ion (green), chlorine ion (white), hydroxyl ion (yellow), acetic acid (cyan), acetate (black), maleic acid (violet), oleate (magenta), and DOX (blue). Water molecules are not shown.

PAA aggregation behaviour is further quantified by computing the overall radius of gyration (R_g) of all chains, solvent accessible surface area (SASA), and hydrogen bonding, for the PAA of 0.123 M concentration case (Table 4.2), in simulated gastric and intestinal fluids corresponding to the pH values in Table 4.1. Both the R_g and SASA increases with an increase in pH. Electrostatic repulsion between chains increase with an increase in f, thus resulting in higher water content and lesser compaction of aggregates. Note however that an increase in f does not result in an increase in the inter-chain hydrogen bonding as the COO^- formed on deprotonation can still hydrogen bond with $COOH$.

Table 4.2 Radius of gyration for all chains, SASA/monomer and hydrogen bonding per monomer of syndiotactic PAA20 at different degrees of deprotonation with random deprotonation. The values in brackets are the standard deviation of the last decimal.

pH	***f***	***Rg(nm)***	***SASA/momomer (nm^2)***	***Hydrogen bonding***	
		All chains		COO^- and COOH	COOH and COOH
1.6	0	4.3(2)	0.403(8)		0.106(6)
5	0.05	4.3(1)	0.428(7)	0.109(4)	0.077(4)
5.8	0.25	4.54(2)	0.532(5)	0.258(5)	0.021(2)

As shown in Figure 3.6 of the previous chapter, PAA-PAA intermolecular RDF peaks decreases with increase in f, with an increase in electrostatic repulsion between PAA20 chains. Figure 4.4 shows the intermolecular RDF between the various components in the system with PAA, essentially characterized by the hydrogen bonding and electrostatic repulsion between charged components. For example, the chloride ions exhibit repulsion from PAA of similar charge, but the sodium ions show an effective attraction exhibit an attraction with PAA that increases with increase in f. Similarly, PAA binds strongly with acetate when compared to acetic acid due to a higher magnitude of hydrogen bonding. However, both maleic acid and oleate show similar interactions. Comparison of the RDF of different components therefore provide an understanding of the molecular interactions prevalent in the system at the simulated compositions.

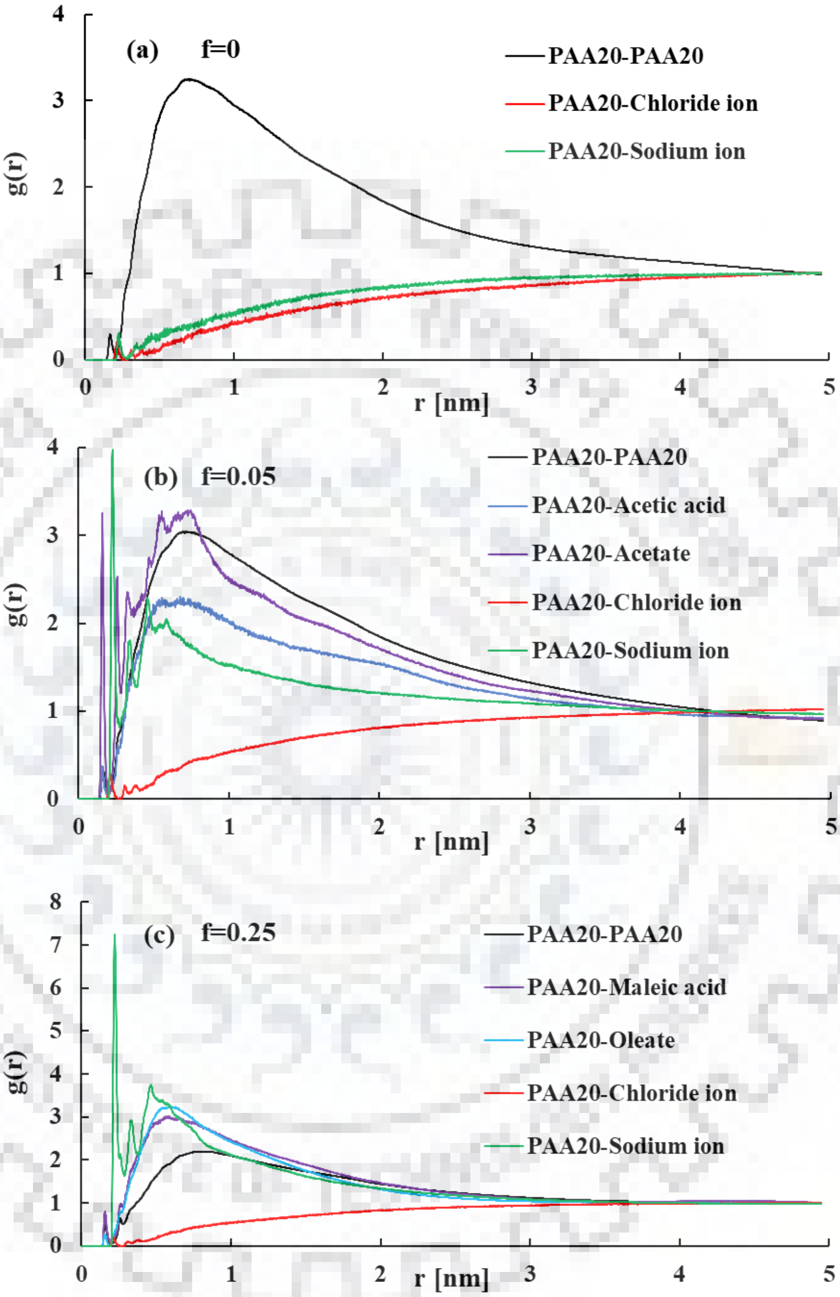

Figure 4.4 Intermolecular PAA20-simulated fluids components RDF for syndiotactic PAA20 of 0.123 M concentration of (a) $f = 0$, (b) $f = 0.05$ and (c) $f = 0.25$ with random deprotonation.

4.4. SUMMARY

In this chapter, we show a successful demonstration of the application of molecular simulation in providing molecular insights into the behavior of pH-responsive controlled release formulations. We studied the polymer behavior in model gastric/intestinal fluids in these simulations. Multiple oligomers of PAA are simulated in model gastric and intestinal fluids, the gastric fluid has lower pH than intestinal fluid. PAA chains shows aggregation behavior in gastric fluid, and is soluble in intestinal fluid.

CHAPTER 5

THE EFFECTS OF MEDIA-DRUG AND CARRIER-DRUG INTERACTIONS ON pH-RESPONSIVE DRUG CARRIERS

5.1. INTRODUCTION

In this chapter, we simulated multiple oligomers of PAA with multiple molecules of a cationic anticancer drug, Doxorubicin (DOX), for a range of pH values representative of various physiological conditions. The diffusion coefficient of DOX decreases with an increase in pH due to an increase in the ionic complexation of PAA with DOX, despite a decrease in PAA aggregation. Our findings are in agreement with recent experimental reports on pH-triggered targeting of tumor cells by PAA-DOX system. Simulations, can be used to infer behavior for both the oral drug delivery and intravenous drug delivery; blood and gastric/intestinal fluids are mostly water but vary with other components. Simulations are performed in water without these additional components and therefore, a smaller box size 6 nm is considered sufficient. Results of these studies establish that both carrier aggregation and carrier-drug interactions are competing influences that together determine the drug release from pH-responsive polymers.

5.2. SIMULATION METHODOLOGY

MD simulations involve an energy minimization step, followed by MD equilibration performed for $\sim 50\,ns$, and MD production performed for additional $30\,ns$ with a typical sampling frequency of $80\,ps$. Both equilibration and production simulations are performed in the NVT ensemble with a reference temperature of 298 K. Number of PAA20-PAA20 and PAA20-DOX contacts with time are monitored to track the equilibration time, where a “contact” is counted if any atom of molecules of one species is within a chosen threshold distance ($0.6\,nm$) from any atom of molecules of another species. We observed that beyond $\sim 50\,ns$ equilibration, the number of contacts converged to an average value, as shown in Figure 5.1. The number of hydrogen bonds between the two species is defined as the number of donor-acceptor pairs that are within a threshold distance $0.35\,nm$ and the hydrogen-donor-acceptor angle less than 30 degrees. The diffusion coefficient of DOX, D, is computed using Einstein’s relation, $\langle r^2 \rangle = 6Dt$, as one-sixth of the slope of mean square displacement $\langle r^2 \rangle$ against time t. Here, the slope is determined for the linear part of the mean square displacement against time plot for reasons elaborated in an earlier study(Jha and Larson 2014).

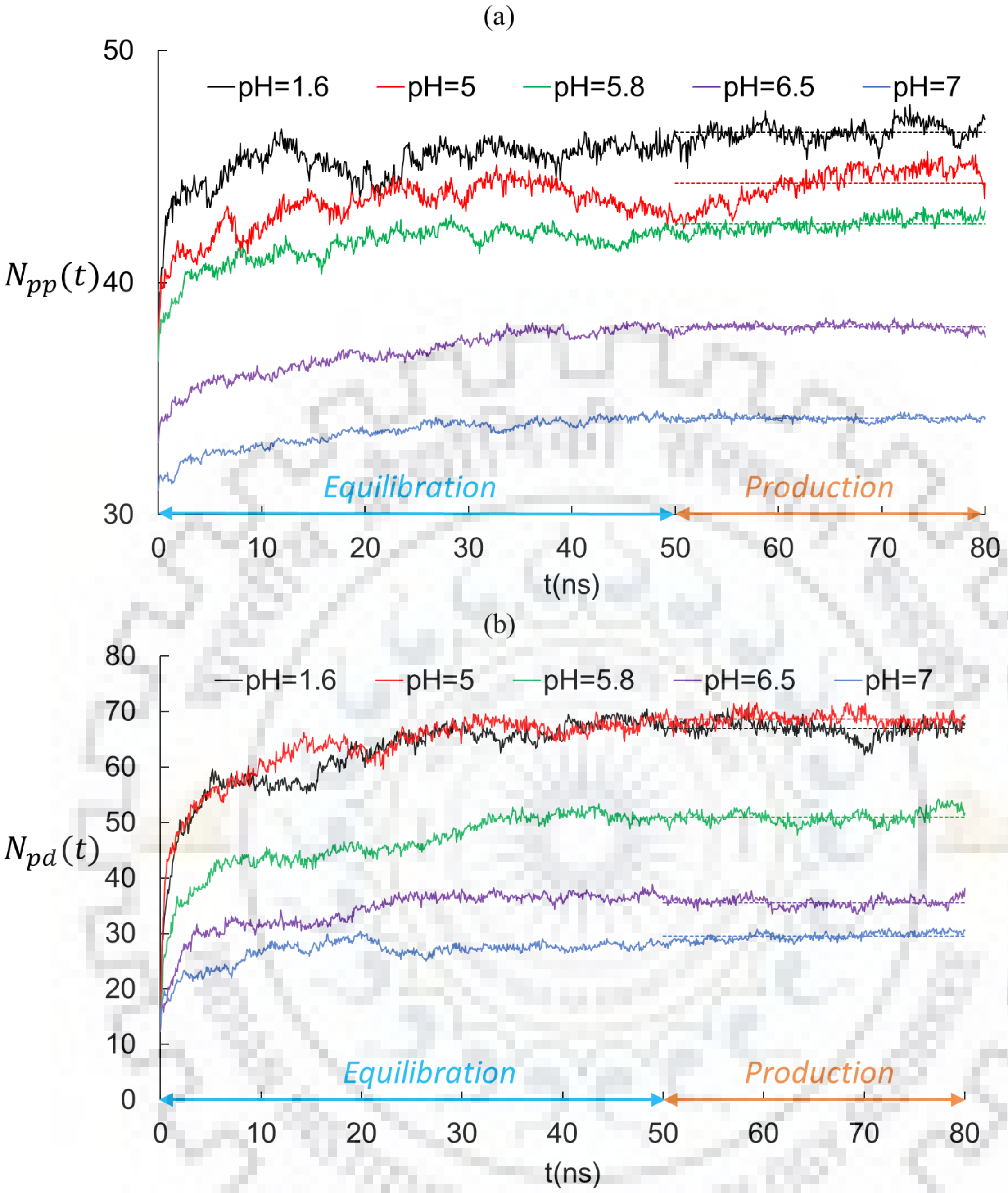

Figure 5.1 Profiles of normalized number of (a) PAA20-PAA20 contacts against time, and (b) PAA20-DOX contacts against time. All the simulations details are in Table 4.1. $N_{pp}(t)$ is normalized by the total number of atoms of all PAA20 chains. $N_{pd}(t)$ is normalized by the product of the number of PAA20 chains and the number of DOX molecules. After 50 ns of equilibration run, all of these profiles converged around average values indicated by dashed lines in the figure.

5.3. RESULTS AND DISCUSSION

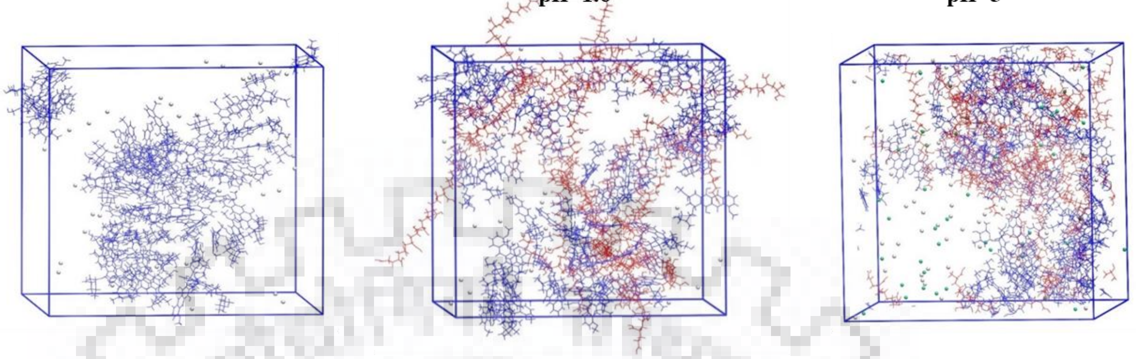

(a) DOX in water

(b) PAA20-DOX in water, pH=1.6

(c) PAA20-DOX in water, pH=5

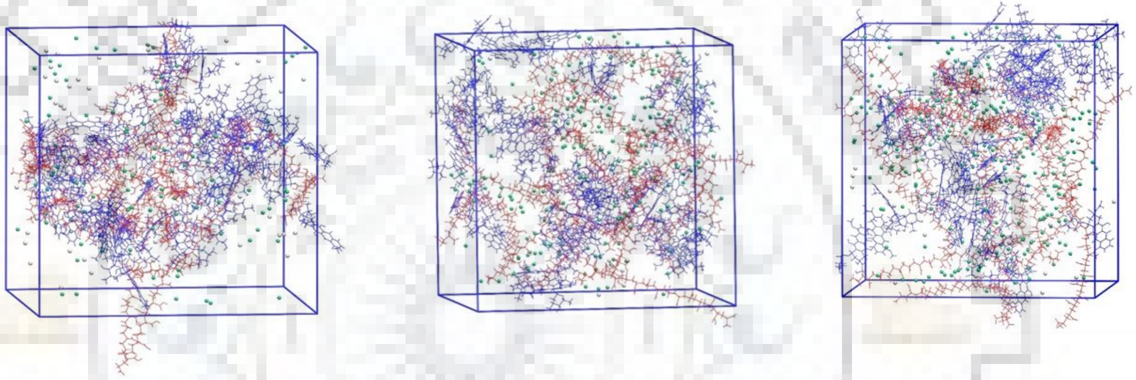

(d) PAA20-DOX in water, pH=5.8

(e) PAA20-DOX in water, pH=6.5

(f) PAA20-DOX in water, pH=7

Figure 5.2 Simulation snapshots (after equilibration) for systems described in Table 4.1. Colour scheme: PAA20 (red), sodium ion (green), chlorine ion (white), and DOX (blue). Water molecules are not shown.

The decrease in PAA20 aggregation with an increase in pH is expected to result in higher entrapment (lower release) of drug molecules at lower pH of gastric fluids than compared to intestinal fluids. This is indeed observed in an earlier simulation study of pH-responsive polymer HPMCAS with phenytoin, which was modelled as a neutral drug (Jha and Larson 2014). However, as shown in Table 5.1, we observe that the DOX diffusion coefficient generally decreases with an increase in pH. A slight increase in diffusion coefficient occurs between $pH = 5$ and $pH = 5.8$, since a decrease in $COOH - COOH$ hydrogen bonding with pH increase is accompanied by an increase in $COO^{-} - COOH$ hydrogen bonding, and therefore, the overall inter-chain PAA20 hydrogen bonding is higher for the $pH = 5.8$ case compared to $pH = 5$ case. This issue has been elaborated in detail in our earlier simulation of PAA20 in water, where we systematically varied the degree of deprotonation and deprotonation patterns. Excluding this minor aberration, the general decrease in DOX diffusion coefficient and slope of the mean square displacement (Figure 5.3) with increase in pH can be attributed to an increase in hydrogen bonding between COO^- group of PAA20 and NH_3^+ group of DOX (Figure 5.4). Note that since a purely geometric criteria is used to determine “hydrogen bonding” between COO^- and NH_3^+ groups, the extend of this “hydrogen bonding” may also be considered as a extent of “ionic complexation” between these groups. Also, in first glance, the fact that number of PAA-DOX contacts decreases with an increase in pH (Figure 5.1b) appears to contradict to fact that the “hydrogen bonding”/“ionic complexation” between PAA20 and DOX increases with an increases in pH (Table 5.1). However, to closer inspection, we can observe that it occurred, because a relatively larger threshold distance (0.6 nm) was used for the computation of the number of PAA20-DOX contacts as compared to the threshold distance of 0.35 nm used for the computation of hydrogen bonding.

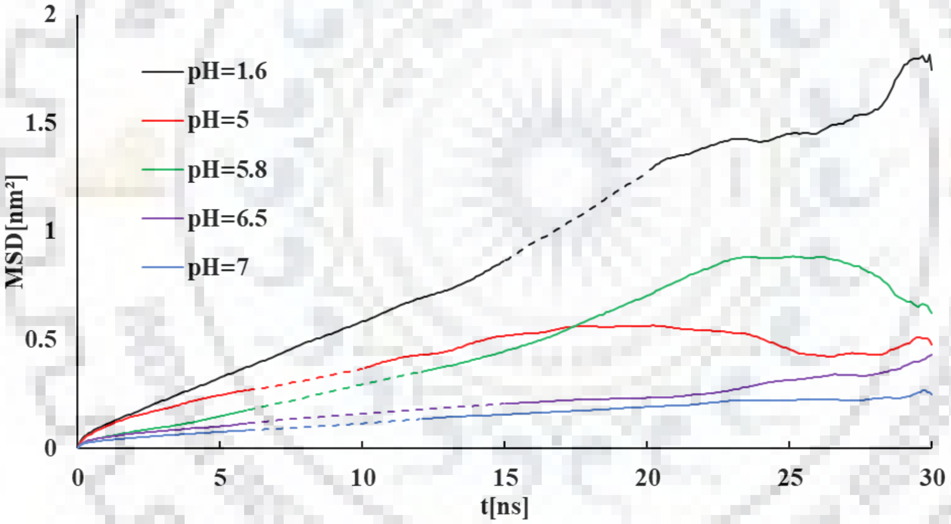

Figure 5.3 Mean square displacement (MSD) of DOX w.r.t time with different pH condition of syndiotactic PAA20 of 0.123 M concentration with random deprotonation and DOX concentration 0.384 M. The dashed lines show the fit using a straight line slope for DOX diffusion coefficient.

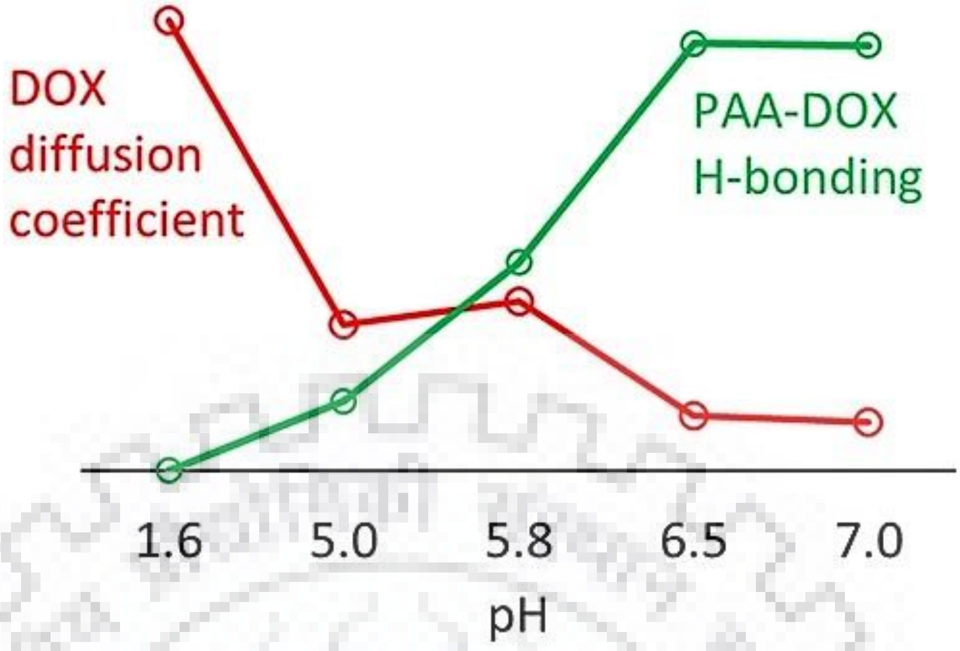

Figure 5.4 DOX diffusion coefficient decreases and PAA-DOX hydrogen bonding increases with increase in pH. See Table 5.1 for the magnitudes of diffusion coefficient and hydrogen bonding.

Finally, the diffusion coefficient of DOX is substantially reduced in the presence of PAA20 ($\sim 5-50$ times in the pH range studied in Table 5.1) compared to the case when PAA20 is not present (also compare Figure 5.2b-f and Figure 5.2a), demonstrating the controlled release behavior of PAA20-DOX system. Our observation that the DOX diffusion coefficient decreases with an increase in pH is in close agreement with the experimental studies of similar systems(Cunningham et al. 2018; Dadsetan et al. 2013; Kim, Kabanov, and Bronich 2009; Tian et al. 2007a; Tian et al. 2007b). One of the closed experiments work by Tian et al. who synthesized pH-responsive block-copolymers of PAA with pluronic copolymers and studied DOX loading and release behaviour. They observed a triggered release in acidic condition at $pH = 5$ and sustained release at $pH = 7.2$, which can be explained by the decrease in DOX diffusion coefficient with an increase in pH observed in our simulations. Other studies(Cunningham et al. 2018; Dadsetan et al. 2013; Kim et al. 2009) that did not use PAA but contain carboxyl groups showed a similar triggered release of DOX in acidic pH.

Table 5.1 Simulation results for set 2 described in Table 4.1. The values in brackets indicate the standard deviation of the last digit in decimals, e.g., 3.04(4) is equivalent to 3.04 ± 0.04. The last row represents the diffusion coefficient of DOX in the system containing no PAA.

pH	**f**	**Diffusion coefficient (10^{-7} cm^2/s)**	**Hydrogen bonding**	
		DOX	*COO$^-$ and NH3$^+$*	*PAA20 and PAA20*
1.6	0	1.30		0.089(9)
5	0.05	0.42	0.036(3)	0.122(9)
5.8	0.25	0.49	0.107(6)	0.17(1)
6.5	0.60	0.16	0.220(6)	0.117(6)
7	0.85	0.14	0.219(9)	0.037(5)
DOX		7.00		

5.4. SUMMARY

The results of this chapter demonstrate the potential of atomistic MD simulations in analyzing the changes in polymer-drug complexation with changes in physiological conditions, and its effect on drug diffusivity. The fact that the simulation results are able to explain the experimental findings of COOH-DOX complexation at high pH demonstrates the power of these simulations, which can therefore be used in the molecular design of excipients.

CHAPTER 6

MIMICKING THE DISSOLUTION BEHAVIOR OF pH-RESPONSIVE DRUG FORMULATIONS

6.1. INTRODUCTION

In previous chapters, we studied the molecular insights into the pH-induced changes in polymer aggregation and polymer-drug complexation obtained using molecular simulations. While we succeed in understanding the physical changes associated with drug entrapment and subsequent release, the actual design of controlled release formulation also requires insights into the changes in drug diffusivity during the dissolution process inside the human body. Depending on the formulation design, the controlled release may occur by a swelling or erosion mechanism. In the swelling mechanism, the drug diffusivity is enhanced as the formulation takes up water and in the erosion mechanism, the polymer erodes giving rise to increase in drug diffusivity. In this chapter, we attempt to mimic these two changes using molecular simulations.

We perform atomistic molecular dynamics (MD) simulations of polyacrylic acid (PAA)-doxorubicin (DOX) formulations dissolved in water. Sequential water removal is performed during the MD simulations, followed by re-equilibration, until an amorphous state devoid of water is achieved. This, therefore mimics the dissolution behavior of swelling-controlled amorphous solid dispersions. We discuss the changes in PAA-DOX interactions and DOX diffusion coefficient as a function of water content, at pH values representative of gastric and intestinal fluids. We then perform simulations for different PAA concentration to understand erosion-controlled behaviour. Simulations are also performed for different DOX concentration, and PAA chain lengths to understand the effect of drug loading and polymer molecular weight, respectively.

6.2. SIMULATION METHODOLOGY

The sequential water removal approach used here is inspired from an earlier study(Jha and Larson 2014) for reverse mimicking the dissolution process of cellulosic excipients with the drug phenytoin. We start from a system containing polymer and drug molecules in water corresponding to the dissolved state of the formulation inside the body. This system is first equilibrated in the NVT ensemble for 110 ns using the protocol of our previous study(Katiyar and Jha 2018). We then remove 10% of the total number of water molecules from the system from the configuration after 110 ns. The molecules removed were located at random positions in the box. The system is then subject to another 20 ns of equilibration and 30 ns of production in the NPT ensemble with a reference temperature of 298 K and reference pressure of 1 bar. Nosé-Hoover thermostat and Berendsen barostat are used for temperature and pressure control, respectively, with a temperature and pressure coupling constant of $0.5\,ps$ in both equilibration and production simulations.

Simulations for different PAA concentrations are performed in the NVT ensemble using the protocol of previous study(Katiyar and Jha 2018) with equilibration for 80 ns and production for $30\,ns$. Simulations for different DOX concentration are performed similarly with equilibration for $50\,ns$ and production for $30\,ns$. Simulations for different PAA chain lengths are also performed with equilibration for 80 ns and production for 30 ns.

Number of PAA-DOX contacts with time, $N_{pd}(t)$ (normalized by the total number of atoms of oligomers molecules) is monitored with time to track the equilibrium process. Here, a “contact” is counted if any atom of one species is within a chosen threshold distance ($0.6\,nm$) from any atom of another species. The calculation of hydrogen bonds and radial distribution functions (RDFs) were performed as our previous study. For the calculation of DOX and water diffusion coefficient, we have divided the production run in three parts of $10\,ns$, and computed average diffusion coefficient of DOX, D, using Einstein’s relation, $\langle r^2 \rangle = 6Dt$, as one-sixth of the slope of mean square displacement $\langle r^2 \rangle$ against time t and standard deviation, SD. Here, the slope is determined for the linear part of the mean square displacement against time plot for reasons elaborated in an earlier study (Jha and Larson 2014).

6.3. RESULTS AND DISCUSSION

6.3.1. Effect of water weight

We monitor the number of PAA20-DOX contacts with time, which appear to converge after $80\,ns$, as established by simulations performed for a longer time of $110\,ns$ (Figure 6.1) before water removal. During sequential water removal as shown in Figure 6.1, PAA20-DOX contacts with time converge to an average value for every intermediate water weight %, and the process is continued until all the water is removed. It is worth pointing out that the equilibration at different weight % was rapid as the water is removed in small increments. On removal water weight % in larger increments, we noticed that the equilibrium times were much longer and often resulted in simulation instabilities. Note that our simulation times are within current computational capabilities of MD simulations. The prospect of further complexation or crystallization of PAA20 and DOX occurring over time scales that are much longer than allowed by existing computational capabilities (e.g., time scales higher than 1 μs) can neither be established nor denied. As can be inferred from the simulation snapshots Figure 6.1a-c the PAA20-DOX complexation increases with decrease in water weight %.

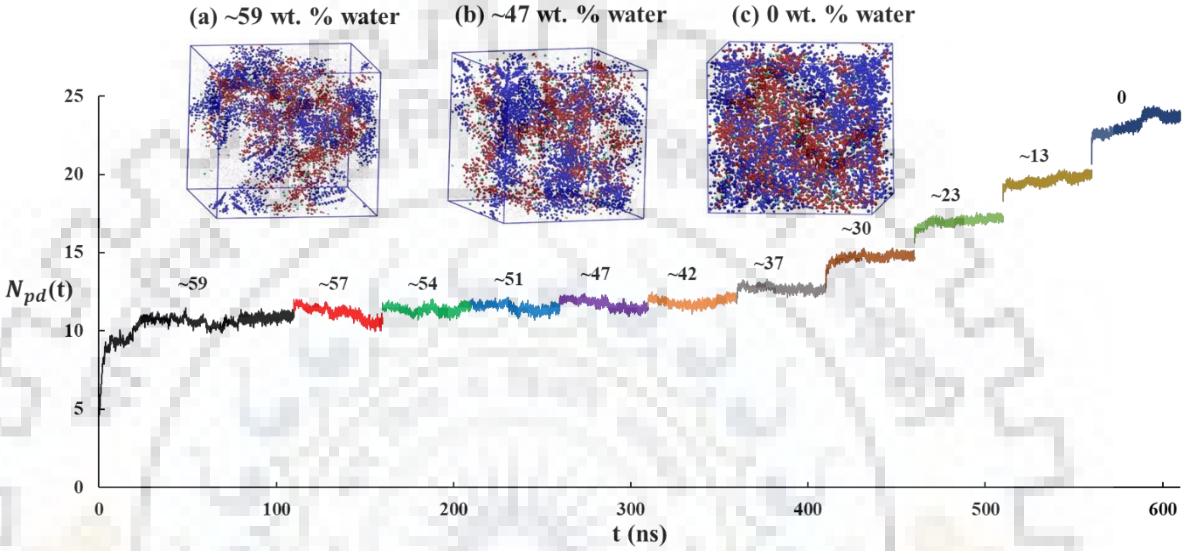

Figure 6.1 Number of PAA20-DOX contacts with time for syndiotactic random deprotonated PAA20 of 0.123 M concentration for $f = 0.60$ and DOX concentration 0.384 M with different approximated water weight percent shows in solid line. Black line indicate 80ns equilibrium run and 30 ns the production run without water removal in box. Subsequent color lines show sequential removal steps, each having a 20 ns equilibrium and 30 ns production run. $N_{pd}(t)$ is normalized by total numbers of atoms PAA20 chains. Typical simulation snapshots after equilibration are shown in the figure (a)-(c). Color scheme: PAA20 chains (red), sodium ion (green), chlorine ion (white) and DOX (blue). Water molecules are shown in purple dot point.

For swelling-controlled formulation, the controlling factors for the drug release are the changes in drug and water diffusivity with increase in water weight %. As shown in Figure 6.2, both of these changes can be characterized by an exponential function. Drug diffusivity is two orders of magnitude smaller than water diffusivity as the drug molecules are larger and forms complexes with the PAA20. Interestingly, both these diffusivities decreases with an increase in f. The slope of mean square displacement decreases of both DOX and water with decrease water weight %

and Figure 6.3 show slope of DOX $f = 0.60$ of production run last 10 ns. The drug diffusivity at a given water weight % is lower for higher f value due to higher magnitude of PAA20-DOX complexation. Water diffusivity is also reduced in this case, which implies that both the drug release and water uptake are coupled to each other. The exponential function obtained for the diffusivity can easily be incorporated in a diffusion model to obtain the drug release profile. We therefore have an in silico approach to obtain the drug diffusivity through polymer matrices.

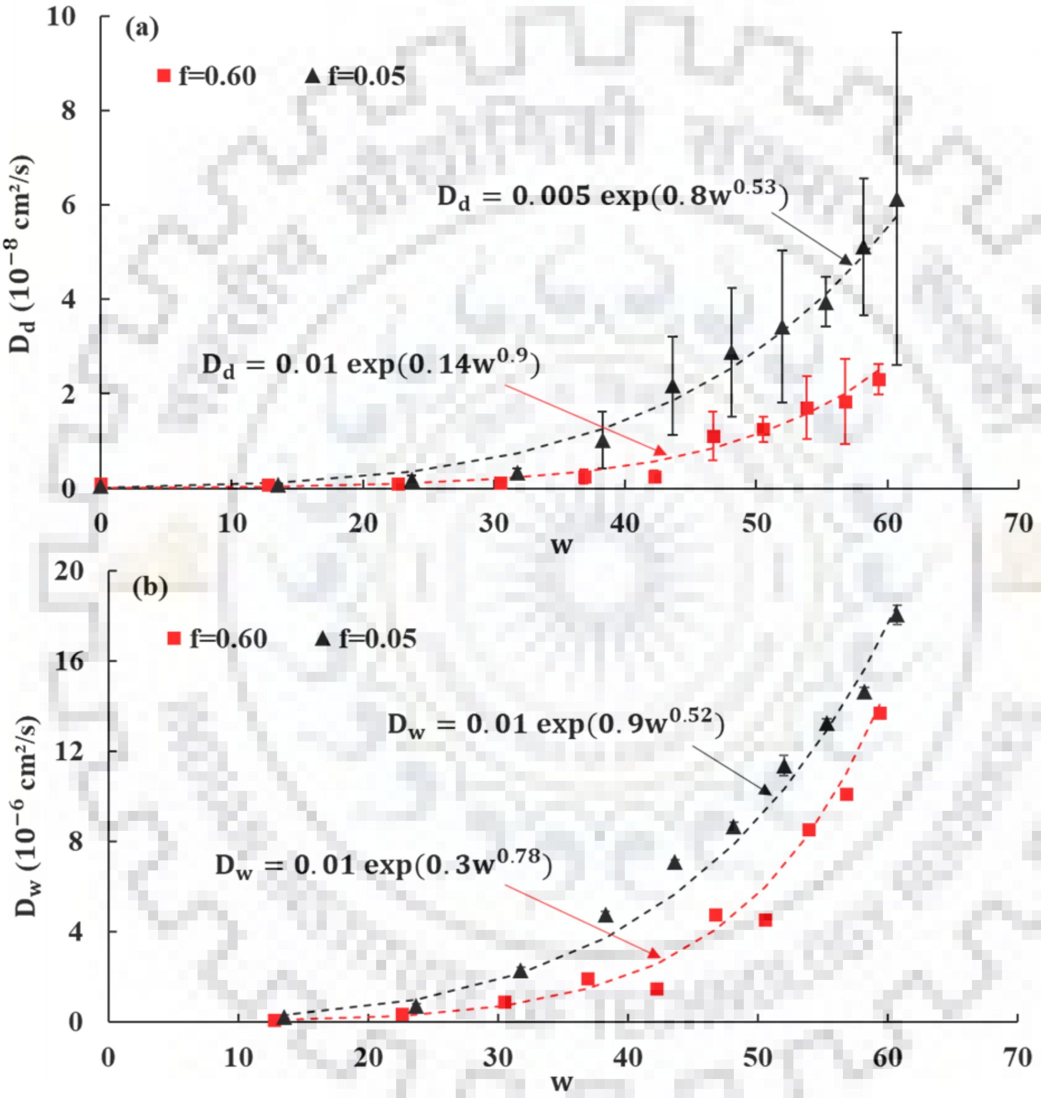

Figure 6.2 (a) Diffusion coefficient of DOX, and (b) Diffusion coefficient of water w.r.t wt. % water (w) of syndiotactic PAA20 of 0.123 M concentration $f = 0.60$ and $f = 0.05$ with random deprotonation and DOX concentration 0.384 M. Markers show the simulation results and the dashed lines show the fit using a function of the type $\mathrm{A}\exp(\mathrm{B}w^{\beta})$.

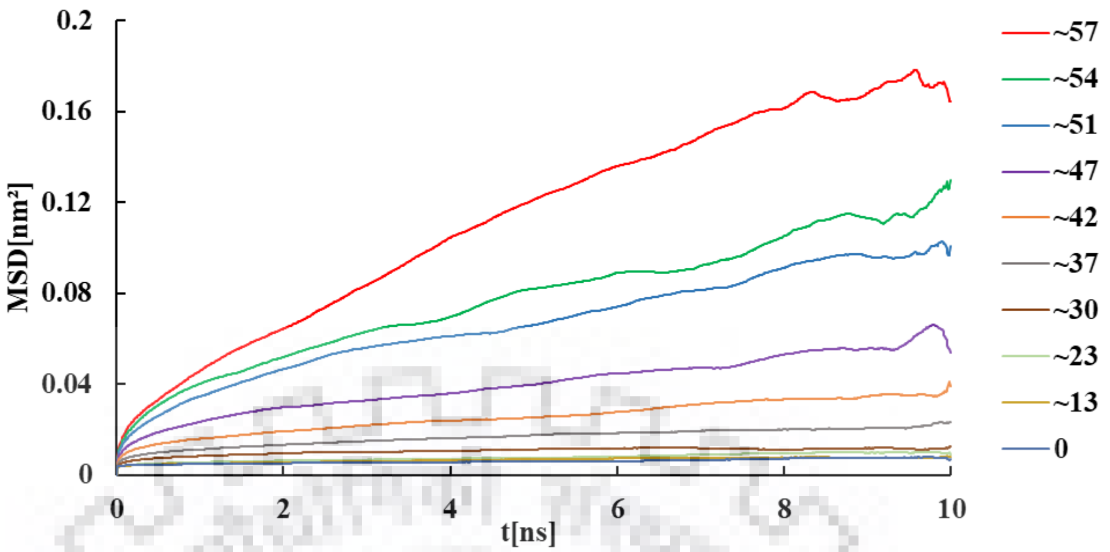

Figure 6.3 Mean square displacement (MSD) of DOX w.r.t time for syndiotactic PAA20 of 0.123 M concentration $f = 0.60$ with random deprotonation and DOX concentration 0.384 M with different approximated water weight percent shows in solid line.

Although free energy calculations are more appropriate to determine the net effective PAA-DOX interaction, a crude measure of the changes in interaction energy upon dissolution can be obtained by observing the changes in various energy contributions in the simulations. Figure 6.4a shows the two major energy contributions responsible for PAA-DOX interactions, which is short-ranged part of the Coulomb interaction (Coul-SR) and short-ranged Lennard Jones (LJ-SR) interactions, which are added together to estimate the effective potential energy of interactions $U(w)$ (Potential). For these calculations, an additional 0.5 ps production run from the final configuration of the earlier production run was performed in the NVT ensemble with a sampling frequency of 50 fs. For obvious reasons, the Coul-SR energies in the higher deprotonation case ($f = 0.6$) are found to be more negative than LJ-SR energies. Both these energies are comparable for the f = 0.05 case, especially for larger w values. The change in potential energy on dissolution can be defined as $\Delta U(w) = U(w) - U(0)$ that shows power law dependence $\Delta U(w) = w^{\alpha}$ as shown in Figure 6.4b. Interestingly, the obtained exponent α is close to the exponent β in the functional form $A\,exp(Bw^{\beta})$ shown in Figure 6.2a for both $f = 0.05$ ($\alpha \approx 0.54, \beta \approx 0.53$) and $f = 0.6$ ($\alpha \approx 0.73, \beta \approx 0.9$) cases. We can therefore say that the diffusion coefficient follows an Arrhenius law dependence

$$\frac{\mathrm{D(w)}}{\mathrm{D(w=0)}} \propto \exp(\kappa \Delta \mathrm{U})$$

where κ is a constant. Note that this analysis ignores the effect of DOX-DOX and DOX-water interactions on DOX diffusion and is therefore only instructive.

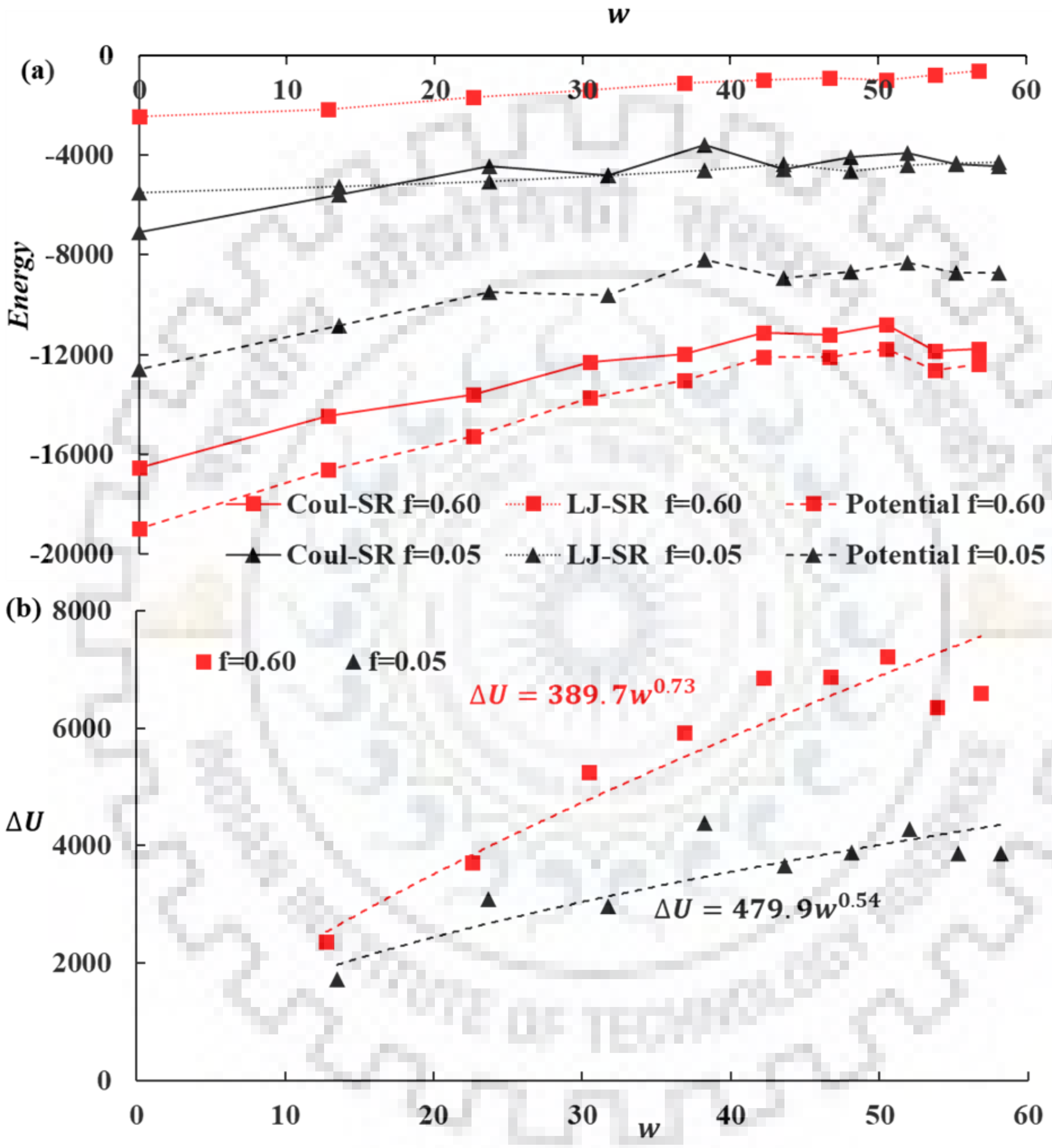

Figure 6.4 (a) Major energy contributions (kJ/mol) of PAA20-DOX interaction, (b) $\Delta U = U(w) - U(0)$ (kJ/mol) against wt. % water (w) for swellable matrix simulations.

Figure 6.5 shows the PAA20-DOX and DOX-DOX RDF for $f = 0.05$ and $f = 0.6$. Since the amount of water is changing for different cases, we multiply the RDF by

$$V_{pd} = \frac{molecules\ of\ water}{volume\ of\ box} \times (molecules\ of\ PAA + DOX)$$

The final plateau values of the normalized RDFs decrease with increase in water weight % that indicates that both the PAA20-DOX and DOX-DOX interactions become weaker with dissolution. The first and second peak of the PAA20-DOX RDF occurring around 0.16 and 0.26 nm in Figure 6.5a exhibit the same trend, since the intermolecular hydrogen bonding decreases between $COOH$ and COO^- groups in PAA20 or $COOH$ of PAA20 and NH_3^+ group in DOX with increasing water weight, as shown in Table 6.1. The second peak at 0.26 nm is absent for the $f = 0.05$ case, because the number of COO^- groups are fewer than $f = 0.6$ case. We also observe a decrease in intermolecular PAA20-PAA20 hydrogen bonding and intermolecular DOX-DOX hydrogen bonding with increase in water weight % (Table 6.1), which implies that both PAA20 and DOX aggregates dissolve with water uptake, thus resulting in an increase in DOX diffusivity as shown in Figure 6.2.

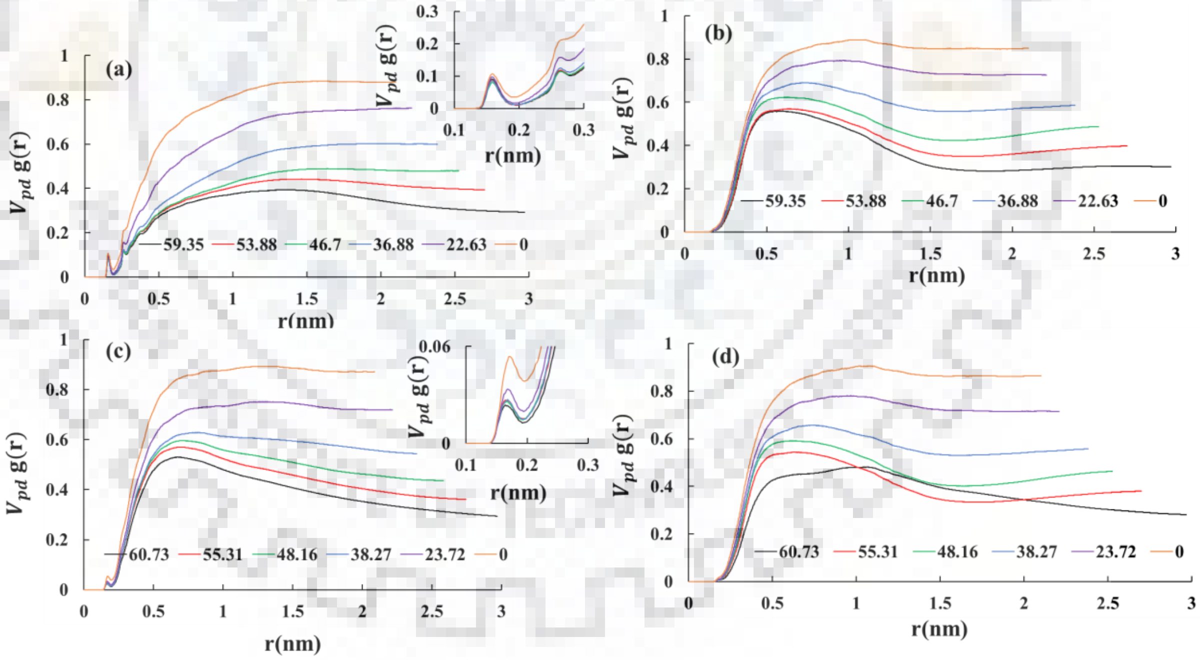

Figure 6.5 Intermolecular (a) PAA20-DOX, (b) DOX-DOX RDF for $f = 0.60$ and (c) PAA20-DOX, (d) DOX-DOX RDF for $f = 0.05$ syndiotactic PAA20 of 0.123 M concentration with random deprotonation and DOX concentration of 0.384 M, with different weight percent water shown in legend. $g(r)$ for small values of r are shown in the inset.

Table 6.1 Hydrogen bonding syndiotactic PAA20 concentration 0.123 M for f = 0.60 and f = 0.05 with random deprotonation and DOX concentration 0.384 M with different weight % water. The values in brackets indicate the standard deviation of the last digit in decimals, e.g., 0.79(4) is equivalent to 0.79 ± 0.04.

Wt. % water at f=0.60	**PAA20-PAA20 HB per DOX at f=0.60**	**PAA20 (COOH and COO$^-$) and DOX NH3 HB per DOX at f=0.60**	**DOX-DOX HB per DOX at f=0.60**	**Wt. % water at f=0.05**	**PAA20-PAA20 HB per DOX at f=0.05**	**PAA20 (COOH and COO$^-$) and DOX NH3 HB per DOX at f=0.05**	**DOX-DOX HB per DOX at f=0.05**
56.79	0.79(4)	1.47(4)	2.68(9)	**58.20**	0.69(6)	0.45(4)	2.70(9)
53.88	0.78(5)	1.47(4)	2.69(9)	**55.31**	0.79(7)	0.46(3)	2.72(9)
50.55	0.79(3)	1.40(5)	2.70(1)	**52.00**	0.76(7)	0.46(4)	2.81(9)
46.70	0.80(5)	1.46(4)	2.75(9)	**48.16**	0.86(7)	0.46(4)	2.76(9)
42.21	0.85(4)	1.50(4)	2.69(9)	**43.64**	0.89(6)	0.51(6)	2.77(9)
36.88	0.88(3)	1.46(5)	2.70(9)	**38.27**	0.96(6)	0.41(4)	2.8(1)
30.48	0.99(4)	1.53(4)	2.80(9)	**31.76**	1.09(6)	0.58(5)	2.76(9)
22.63	1.07(4)	1.61(4)	2.81(8)	**23.72**	1.27(5)	0.56(5)	2.88(9)
12.78	1.22(3)	1.69(3)	2.93(8)	**13.53**	1.49(5)	0.69(4)	2.84(9)
0	1.55(4)	2.01(4)	3.05(9)	**0**	2.54(7)	0.93(4)	3.27(9)

6.3.2. PAA20 concentration effect on DOX

Figure 6.6 shows diffusion coefficient of DOX and water for different PAA20 concentration and constant DOX concentration for $f = 0.60$ and $f = 0.05$. This therefore mimics a situation when the PAA20 is eroding from the formulation, thus resulting in DOX release. As expected, DOX diffusivity increases with a decrease in PAA concentration. This is confirmed by slope of mean square displacement (MSD) increases with a decrease in PAA20 concentration (Figure 6.7). For larger PAA20 concentration (beyond 0.092 M in Figure 6.6a), DOX diffusivity is lower for $f = 0.6$ compared to $f = 0.05$, since the ionic complexation between PAA20 and DOX is higher for $f = 0.6$ case. This is however not true at lower concentrations of PAA20. One explanation for this discrepancy that PAA20 is able to effectively entrap drug only when the drug loading (PAA20 to drug ratio) is high. The water diffusivity monotonically increase with decrease in PAA20 concentration, but the difference in water diffusivity between $f = 0.05$ and $f = 0.6$ cases is larger at higher PAA20 concentration because of larger magnitude of PAA20-DOX complexation.

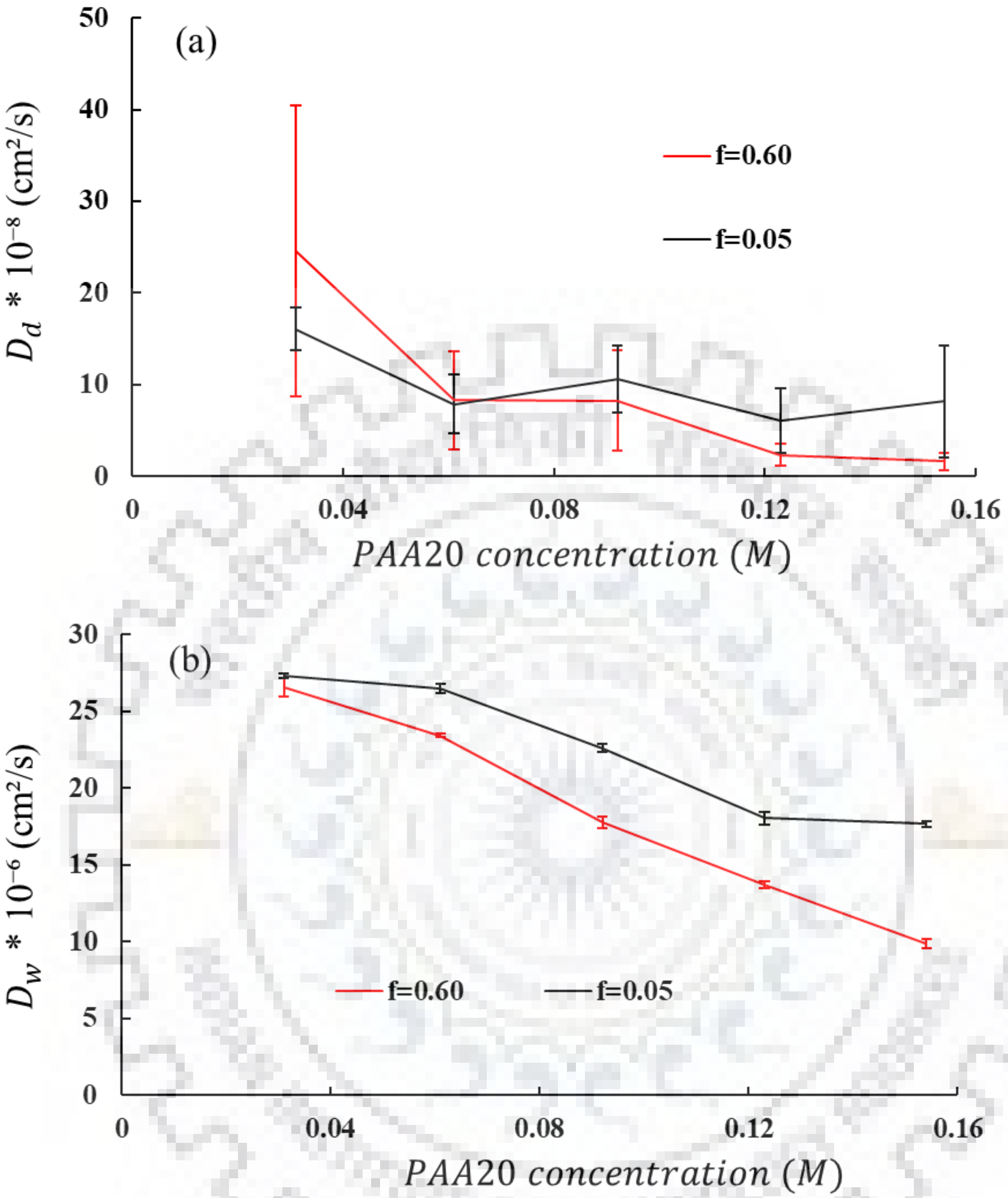

Figure 6.6 Diffusion coefficient of (a) DOX and (b) water after equilibration w.r.t different PAA20 concentration for $f = 0.05$ and $f = 0.60$ and DOX concentration 0.384 M.

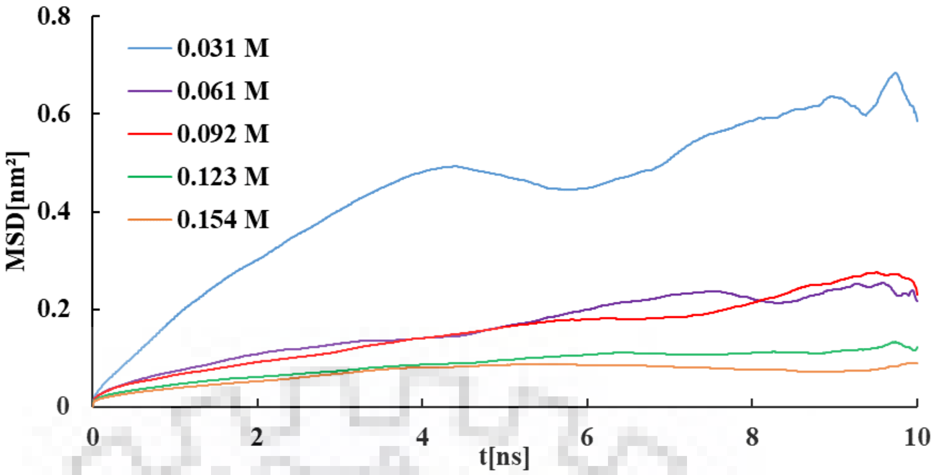

Figure 6.7 Mean square displacement (MSD) of DOX w.r.t time for different PAA20 concentration $f = 0.60$ and DOX concentration 0.384 M.

Figure 6.8 shows PAA20-DOX intermolecular RDF and DOX-DOX intermolecular RDF for different PAA20 concentration (C_p). The PAA20-DOX RDF in Figure 6.8a is normalized by C_p. The final plateau value of the PAA20-DOX normalized RDF decreases and that of DOX-DOX RDF increases with decrease in PAA20, which implies that the erosion of PAA20 will reduce the PAA20-DOX complexation and may result in an increase in DOX-DOX aggregation. Similar trend is observed in the inset of Figure 6.8a, in the peaks corresponding to intermolecular hydrogen bonding. Further insights into the changes in hydrogen bonding behaviour with PAA20 erosion can be attained from Table 6.2. As expected, the intermolecular PAA20-PAA20 hydrogen bonding reduces with a decrease in PAA20 concentration. However, similar trend cannot be established for PAA20-DOX and DOX-DOX intermolecular hydrogen bonding, which may again be attributed to the fact that the PAA20 does not efficiently entrap DOX at lower drug loading.

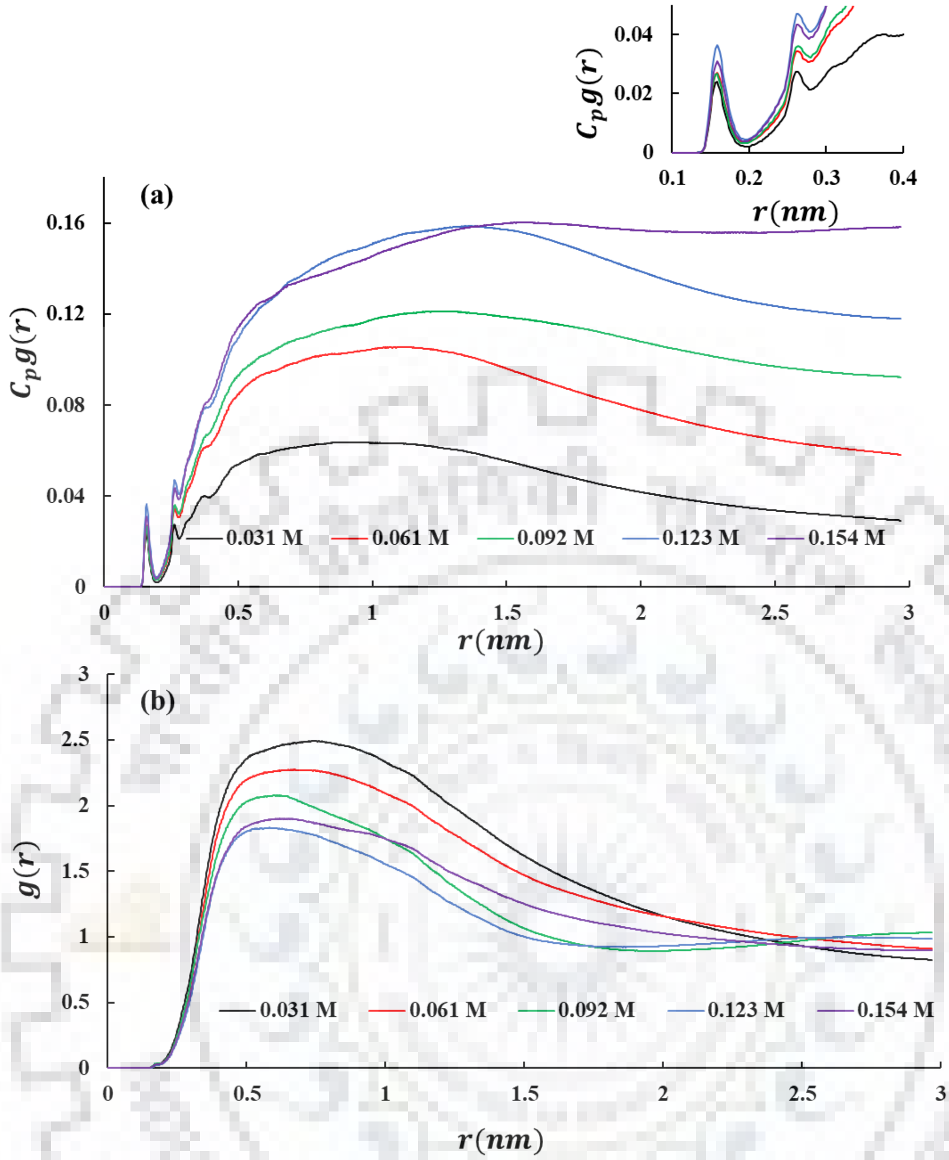

Figure 6.8 Intermolecular (a) PAA20-DOX and (b) DOX-DOX RDF of different PAA20 concentration with $f = 0.60$ and DOX concentration 0.384 M. $C_pg(r)$ for small values of r are shown in the inset.

Table 6.2 Hydrogen bonding different PAA20 concentration with $f = 0.60$ and $f = 0.05$ and DOX concentration 0.384 M. The values in brackets are the standard deviation of the last decimal.

PAA20 concentration (M)	**PAA-PAA HB per DOX at $f = 0.60$**	**PAA20 ($COOH$ and COO^-) and DOX NH_3^+ HB per DOX at $f = 0.60$**	**DOX-DOX HB per DOX at $f = 0.60$**	**PAA-PAA HB per DOX at $f = 0.05$**	**PAA20 ($COOH$ and COO^-) and DOX NH_3^+ HB per DOX at $f = 0.05$**	**DOX-DOX HB per DOX at $f = 0.05$**
0.031	0.07(1)	1.01(3)	2.88(9)	0.13(2)	0.20(3)	2.93(9)
0.061	0.38(2)	1.20(3)	2.75(9)	0.30(4)	0.34(4)	2.73(9)
0.092	0.61(4)	1.15(4)	2.85(9)	0.51(9)	0.41(4)	2.98(8)
0.123	0.75(4)	1.59(5)	2.76(9)	0.78(7)	0.45(4)	2.78(9)
0.154	1.25(6)	1.22(5)	2.78(9)	1.19(8)	0.48(4)	2.75(9)

6.3.3. DOX concentration effect on PAA20

We have also performed studies on variation of DOX concentration for a given PAA20 concentration. This might correspond to a case of non-swellable fixed carrier. As shown in Figure 6.9, DOX diffusivity increase with a decrease in DOX concentration, especially for DOX concentrations beyond 0.23 M. As earlier, the DOX diffusivity is lower for $f = 0.6$ case when compared to $f = 0.05$ case, due to higher magnitude of PAA20-DOX complexation. The water diffusivity increases with decrease in DOX concentration. As shown in Table 6.3, with a decrease in DOX concentration, PAA-DOX hydrogen bonding decreases and PAA-PAA hydrogen bonding increases. This is because COO^- groups on PAA20 that were earlier forming complex with NH_3^+ will form hydrogen bonds with $COOH$ on PAA20, when the DOX concentration reduces. DOX-DOX intermolecular hydrogen bonding also reduces with a decrease in DOX concentration.

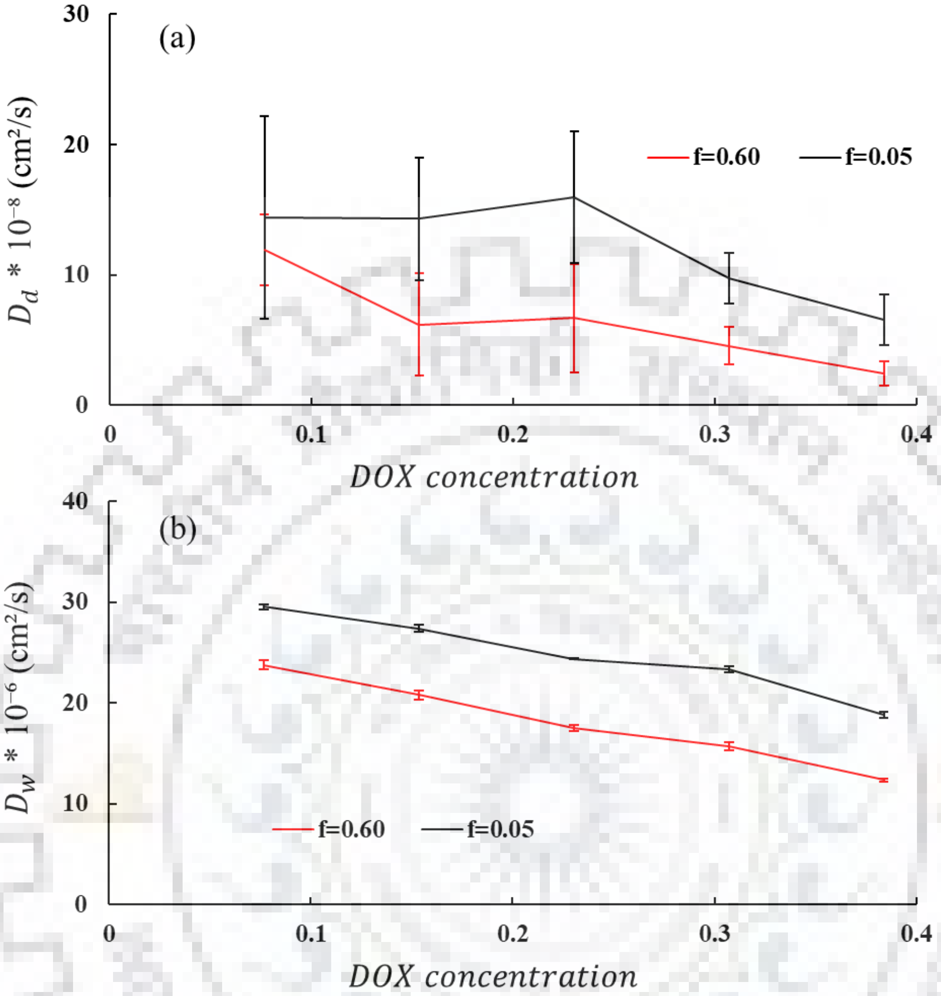

Figure 6.9 Diffusion coefficient of (a) DOX and (b) water after equilibration w.r.t DOX concentration, and constant PAA20 concentration 0.123 M for $f = 0.60$ and $f = 0.05$.

Table 6.3 Hydrogen bonding different concentration of DOX, and constant syndiotactic PAA20 concentration 0.123 M for $f = 0.60$ and $f = 0.05$. The values in brackets indicate the standard deviation of the last digit in decimals, e.g., $5.2(3)$ is equivalent to 5.2 ± 0.3.

DOX concentration (M)	**PAA-PAA HB per DOX at $f = 0.60$**	**PAA20 ($COOH$ and COO^-) and DOX NH_3^+ HB per DOX at $f = 0.60$**	**DOX-DOX HB per DOX at $f = 0.60$**	**PAA-PAA HB per DOX at $f = 0.05$**	**PAA20 ($COOH$ and COO^-) and DOX NH_3^+ HB per DOX at $f = 0.05$**	**DOX-DOX HB per DOX at $f = 0.05$**
0.0768	5.2(3)	1.7(1)	2.6(2)	6.8(5)	0.3(2)	2.6(2)
0.1536	2.9(2)	1.30(8)	2.7(1)	2.6(3)	0.76(9)	2.7(1)
0.2304	1.46(6)	1.61(8)	2.7(1)	1.5(1)	0.48(6)	2.8(1)
0.3072	1.10(5)	1.23(5)	2.7(1)	1.2(1)	0.55(5)	2.83(9)
0.3840	0.89(8)	1.33(4)	2.8(1)	0.51(8)	0.53(4)	2.74(9)

6.3.4. PAA20 chain length variations

Finally, we look at the dependence on PAA chain length, which will correspond to the dependence of polymer molecular weight in experiments. As shown in Figure 6.10, DOX diffusivity decreases with an increase in PAA chain length. However, the fluctuations in DOX diffusivity are much higher for PAA5 case, as the molecule is too small to provide drug entrapment.

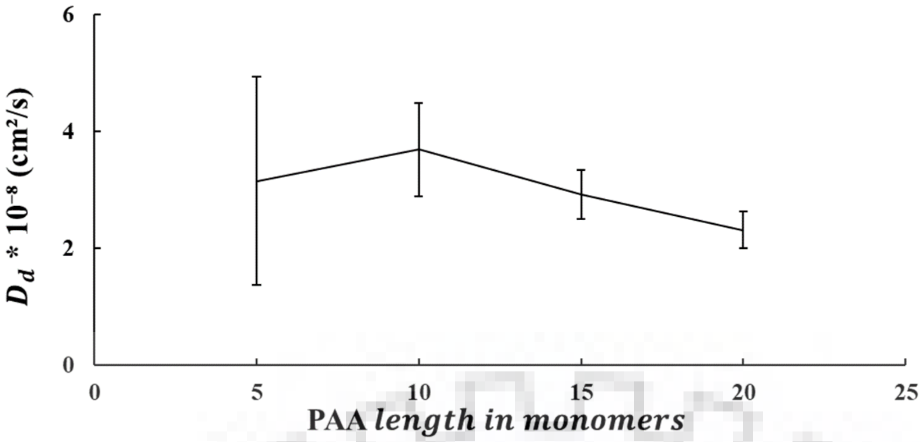

Figure 6.10 Diffusion coefficient of DOX after equilibration w.r.t syndiotactic PAA at different length in monomers of concentration 0.123 M for $f = 0.60$ with random deprotonation and DOX concentration 0.384 M.

6.4. SUMMARY

Atomistic simulations presented in this chapter mimics the dissolution behaviour of polymer-drug formulations for the cases of (a) drug release from swellable matrix, (b) drug release from eroding matrix, (c) drug release from fixed carrier. The diffusion coefficients of water and drug obtained from the simulations can be used in diffusion models to obtain the drug release in realistic situations.

CHAPTER 7

CONCLUSIONS AND RECOMMENDATION

7.1. CONCLUSIONS

Our rationale behind this study was to demonstrate the potential of atomistic molecular dynamics (MD) simulations in the design of pH-responsive carriers for drug delivery. Although the MD simulations do include the detailed chemistry of molecules and thus can be used prior to synthesis, these are limited to small length and time scales. Despite this, as we demonstrate through several examples, we succeed in providing a molecular understanding that explains the experimental findings and also provide information not attainable from macroscopic models. Some of these salient findings include.

1. Size of PAA (polyacrylic acid) chains in aqueous solution increase with pH and varies with tacticity in the order syndiotactic > atactic > isotactic. However, tacticity does not much influence the PAA phase behavior in solution.
2. PAA aggregation increases with PAA concentration and with a decrease in pH, however the size of individual chains increase with increase in concentration. Water content of aggregates decrease with increase in concentration and a decrease in pH. When expressed in terms of solvent-accessible surface area, water content showed a 3-fold increase between the neutral and fully deprotonated limits.
3. PAA aggregation depends on the deprotonation pattern; end deprotonation and random deprotonation showed the formation of micelle-like and network-like aggregates, respectively. Interactions that were found relevant to the aggregation behavior included the hydrogen bonding between $COOH - COOH$ and $COO^{-} - COOH$ groups, electrostatic repulsion between COO^{-} groups, and counterion (Na^{+}) bridging between the COO^{-} groups.
4. We were able to simulate model compositions of simulated biological fluids (fed and fasted state gastric and intestinal fluid) and their interactions with PAA are determined. pH plays a major role in determining the PAA phase behavior in biological fluids.
5. In simulations of PAA and DOX (doxorubicin) in water at different pH, we observe that the diffusion coefficient of DOX decreases with increase in pH of the solution, as the hydrogen bonding between PAA (COOH and $\mathrm{COO^{-}}$) and DOX ($\mathrm{NH_3^{+}}$) increases.

6. Dissolution behavior of polymer-drug formulations for both swellable and fixed carrier matrices and also the eroding matrices are understood using MD simulations. Here, MD may provide an understanding of molecular changes associated with dissolution and also provide scaling laws of diffusivities that can be incorporated into pharmacokinetic models or verified by experiments.

7.2. RECOMMENDATION

Several important aspects studied in this thesis require further investigation. First and foremost, our simulations are limited to model oligomers of PAA containing 20 monomers. Studying the effect of chain flexibility on the aggregation behavior will require the simulations of much longer chains, well beyond current computational limitations of atomistic simulations. A useful compromise can be made using a systematic coarse-grained model parametrized using the atomistic simulation results described here (as discussed in Chapter 2 of this thesis), which may then be applied to study longer realistic chains. Second, conventional MD simulations employed in this study assume a fixed deprotonation patterns and does not consider dynamic changes associated with protonation-deprotonation equilibrium. Constant-pH simulations can address these challenges that allow for these changes during the simulations, but are not well developed (as elaborated in Chapter 3 of this thesis). Third, the results of the study can be incorporated into pharmacokinetic models of dissolution.

Though we succeed in our objective of demonstrating the potential of atomistic MD simulations to polymeric drug delivery, we have chosen rather simplified systems in this study (Chapters 4-6 of this thesis). Application of these methods to realistic drug chemistries and in general, to a range of chemistries require the development of in silico screening tools based on these approaches. Such in silico tools should couple atomistic simulations with systematic coarse-graining and macroscopic pharmacokinetic modeling to predict the behavior for realistic length and time scales.

APPENDIX A

This appendix describes the basis equations of molecular dynamics simulations and data analysis employed in this thesis.

A.1. COMPUTATIONAL SIMULATION DETAILS

A.1.1. Newton's equation of motion

Molecular dynamics simulations are based on solving Newton's equation of motion

$$m_i \frac{d^2\vec{r_i}}{dt^2} = \vec{F_i}(t), i = 1,2, \dots\dots\dots, N, \tag{A.1}$$

for all particles in a system, where m_i and $\vec{r_i}$ are the mass and the coordinates of i^{th} particles and $\vec{F_i}(t)$ is the force acting on i^{th} particle at time t.

The force on a particle i is the negative gradient of the interaction potential energy

$$\vec{F_i}(t) = -\frac{\partial U(\vec{r}_{1,}\vec{r}_{2,\dots\dots\dots}\ \vec{r}_N)}{\partial \vec{r}_i} \tag{A.2}$$

A.1.2. The potential energy

The potential energy $U(\vec{r}_{1,}\vec{r}_{2,\dots\dots\dots}\ \vec{r}_N)$ of the system in the CHARMM27 force field includes both bonded and non-bonded contributions. Bonded contributions are of the form:

$$\sum_i^{bonds} k_{bi}\left(b_i - b_{0,i}\right)^2 + \sum_i^{angles} k_{\theta i}\left(\theta_i - \theta_{0,i}\right)^2 + \sum_i^{dihedrals} k_{\phi i}\left[1 + \cos(n_i\phi_i - \delta_i)\right] + \sum_i^{impropers} k_{\varphi i}\left(\varphi_i - \varphi_{0,i}\right)^2, \tag{A.3}$$

i.e., contains bond stretching, angle bending, proper dihedrals, and improper dihedral energies, summed over all possible bonds, angles, proper dihedral, and improper dihedrals of PAA chains and water molecules. Values of force constants ($k_{b,i}, k_{\theta,i}, k_{\phi,i}, k_{\varphi,i}$), multiplicities ($n_i$) and phase shifts ($\delta_i$), and equilibrium values of bond distances ($b_{0,i}$), angles ($\theta_{0,i}$), and out-of-plane angle ($\varphi_{0,i}$) are provided in the topology file. All the above quantities remain constant throughout the simulations. However, magnitudes of the bond distances b_i, angles θ_i, dihedral angle ϕ_i, and out-of-plane angle φ_i are computed on-the-fly during simulations and vary with time. Nonbonded contributions to the potential energy are of the form:

$$\sum_i^{atoms}\sum_{j>i}^{atoms}\epsilon_{ij}\left[\left(\frac{r_{min,ij}}{r_{ij}}\right)^{12}-2\left(\frac{r_{min,ij}}{r_{ij}}\right)^{6}\right]+\frac{1}{4\pi\varepsilon_0}\sum_i^{atoms}\sum_{j>i}^{atoms}\frac{q_iq_j}{r_{ij}}, \qquad \text{(A.4)}$$

and apply between all pairs of atoms in the simulation box, excluding pairs of atoms on the same chain separated by less than three bonds. The first term is the van der Waals contribution represented using a 6-12 Lennard Jones (LJ) potential, where energy well depth ϵ_{ij} and "minimum distance" $r_{min,ij}$ (defined as the finite distance at which LJ potential is zero) values of all pairs are provided in the input topology and remain constant throughout the simulation. The distance between pairs, r_{ij}, vary in the course of the simulation. The second term is the electrostatic energy of pairs of atoms of partial charges q_i and q_j at distance r_{ij}, where ε_0 is vacuum permittivity. Intramolecular 1-4 interactions are the LJ interactions between the pairs of atoms separated by three bonds, which have separate force field parameters than other LJ interactions in the system.

The generated topology file classifies atoms present in the molecule in terms of atom types. All atoms of a given atom type have same magnitude of force field constants except the partial charge. σ_{ij} and ϵ_{ij} are obtained using the mixing rules,

$$\sigma_{ij}=\frac{\sigma_{ii}+\sigma_{jj}}{2}$$

and

$$\epsilon_{ij}=\sqrt{\epsilon_{ii}\epsilon_{jj}}$$

A.1.3. The integration algorithm

To integrate the equation of motion A.1, GROMACS uses the leapfrog algorithm for trajectory writing, which is more generic form of Verlet method. In the leapfrog algorithm, velocity and coordinates are computed from the following equation:

$$\vec{v}_i\left(t+\frac{1}{2}\delta t\right) = \vec{v}_i\left(t-\frac{1}{2}\delta t\right) + \delta t\, \vec{a}_i(t), \tag{A.5}$$

$$\vec{r}_i(t+\delta t) = \vec{r}_i(t) + \delta t\, \vec{v}_i\left(t+\frac{1}{2}\delta t\right), \tag{A.6}$$

Where $\vec{a}_i = \frac{\vec{F}_i}{\vec{m}_i}$ is the acceleration of i^{th} particle and $\vec{v}_i$ and $\vec{r}_i$ are the velocity and position of the i^{th} particle, respectively. Figure A.1 explains the algorithm.

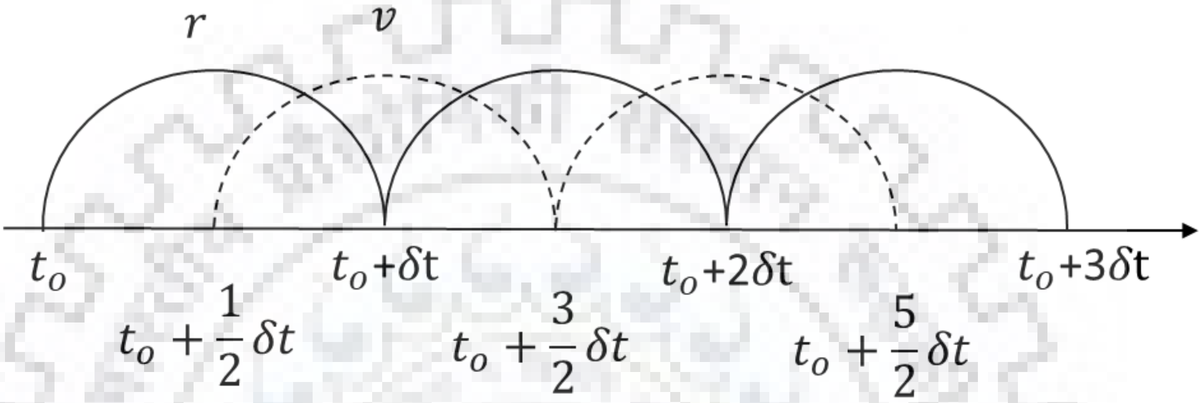
r
v
t_o
t_o+δt
t_o+2δt
t_o+3δt
$t_o + \frac{1}{2}\delta t$
$t_o + \frac{3}{2}\delta t$
$t_o + \frac{5}{2}\delta t$

Figure A.1: Schematic illustration of the leapfrog algorithm: the coordinates $\vec{r}_i$ are calculated at every time step (bold line), velocity $\vec{v}_i$ are calculated at half time steps (dashed line).

A.1.4. Radius of gyration (R_g)

Root mean square radius of gyration R_g (or simply R_g) is defined as the mean square distance between the atoms and center of mass of atoms.

$$R_g^2 = \frac{1}{N+1}\sum_{i=0}^{N}\langle (r_i - r_G)^2\rangle \tag{A.7}$$

Center of mass r_G of polymer chain is average position of all the atoms of the system, weighted according to their atomic masses. If the atomic masses are equal, for example, in the case of bead-spring model shown in Figure A.2.

$$r_G = \frac{1}{N+1}\sum_{i=0}^{N} r_i \tag{A.8}$$

R_g signifies the space occupied by the polymer chain in Figure A.2 and can be thought of as the radius of an equivalent sphere of the same volume as the polymer chain (ignoring a geometric factor).

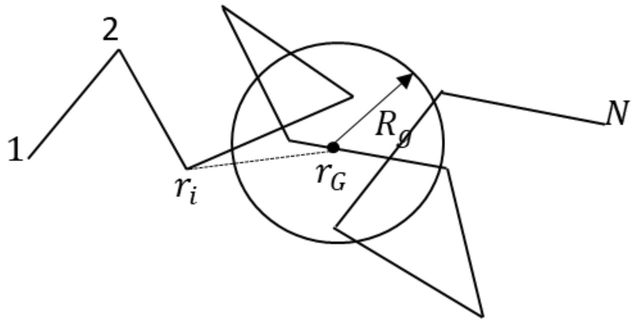

Figure A.2: Radius of gyration R_g and center of mass r_G in a bead spring model

A.1.5. Radial distribution function (RDF)

The radial distribution function (RDF) is a normalized probability distribution function, which represents the probability of an atom to be found at another atom at a separation r. That is,

$$g_{XY}(r) = \frac{\langle \rho_Y(r) \rangle_{local}}{\langle \rho_Y \rangle}$$

$$g_{XY}(r) = \frac{1}{\langle \rho_Y \rangle} \frac{1}{N_X} \sum_{i \in N_X}^{N_X} \sum_{i \in N_Y}^{N_Y} \frac{\delta(r_{ij} - r)}{4\pi r^2} \tag{A.9}$$

where $\langle \rho_Y(r) \rangle_{local}$ is the density of type Y atoms at a distance r around X, and $\langle \rho_Y \rangle$ is the average density of type Y atoms in the simulation box.

A.1.6. Diffusion coefficient

Diffusion coefficient of molecule is calculated by using the Einstein relation, i.e., as the ratio of mean square displacement to the time divided by six for three dimensions.

$$D = \frac{\langle [r(t) - r(0)]^2 \rangle}{6t} \tag{A.10}$$

APPENDIX B

Molecular Topology, Validation Simulations, and force field

In this appendix, we include the structure of PAA chains simulated in the thesis, the results of single chain simulations of PAA performed for validation purposes and force filed parameters

Table B.1 20 monomer atactic PAA chain with random deprotonation, chain 1

Monomer	Tacticity	Charge density					
		f=0	f=0.2	f=0.4	f=0.6	f=0.8	f=1
1	Up	COOH	COOH	COO^-	COO^-	COO^-	COO^-
2	Up	COOH	COO^-	COOH	COOH	COO^-	COO^-
3	Down	COOH	COOH	COOH	COO^-	COO^-	COO^-
4	Down	COOH	COOH	COOH	COO^-	COO^-	COO^-
5	Up	COOH	COOH	COO^-	COOH	COOH	COO^-
6	Down	COOH	COO^-	COO^-	COO^-	COO^-	COO^-
7	Up	COOH	COOH	COOH	COO^-	COO^-	COO^-
8	Down	COOH	COOH	COOH	COO^-	COO^-	COO^-
9	Up	COOH	COOH	COO^-	COOH	COO^-	COO^-
10	Down	COOH	COO^-	COOH	COOH	COOH	COO^-
11	Down	COOH	COOH	COOH	COO^-	COO^-	COO^-
12	Up	COOH	COOH	COO^-	COOH	COO^-	COO^-
13	Up	COOH	COOH	COO^-	COO^-	COO^-	COO^-
14	Up	COOH	COOH	COO^-	COO^-	COO^-	COO^-
15	Down	COOH	COOH	COO^-	COO^-	COO^-	COO^-
16	Up	COOH	COOH	COOH	COOH	COOH	COO^-
17	Down	COOH	COO^-	COOH	COOH	COO^-	COO^-
18	Up	COOH	COOH	COOH	COOH	COOH	COO^-
19	Up	COOH	COOH	COOH	COO^-	COO^-	COO^-
20	Down	COOH	COOH	COOH	COO^-	COO^-	COO^-

Table B.2 20 monomer atactic PAA chain with random deprotonation, chain 2

Monomer	Tacticity	Charge density					
		f=0	f=0.2	f=0.4	f=0.6	f=0.8	f=1
1	Up	COOH	COOH	COOH	COOH	COOH	COO^-
2	Down	COOH	COO^-	COO^-	COO^-	COO^-	COO^-
3	Up	COOH	COOH	COOH	COO^-	COO^-	COO^-
4	Down	COOH	COOH	COO^-	COO^-	COO^-	COO^-
5	Down	COOH	COOH	COOH	COO^-	COO^-	COO^-
6	Up	COOH	COOH	COOH	COOH	COO^-	COO^-
7	Up	COOH	COOH	COOH	COOH	COOH	COO^-
8	Up	COOH	COOH	COOH	COOH	COO^-	COO^-
9	Down	COOH	COO^-	COO^-	COO^-	COO^-	COO^-
10	Up	COOH	COOH	COOH	COOH	COO^-	COO^-
11	Up	COOH	COOH	COOH	COO^-	COO^-	COO^-
12	Down	COOH	COOH	COOH	COOH	COOH	COO^-
13	Down	COOH	COOH	COO^-	COO^-	COO^-	COO^-
14	Down	COOH	COOH	COOH	COOH	COO^-	COO^-
15	Up	COOH	COOH	COOH	COOH	COOH	COO^-
16	Down	COOH	COOH	COOH	COO^-	COO^-	COO^-
17	Up	COOH	COOH	COO^-	COO^-	COO^-	COO^-
18	Up	COOH	COO^-	COO^-	COO^-	COO^-	COO^-
19	Down	COOH	COO^-	COO^-	COO^-	COO^-	COO^-
20	Down	COOH	COOH	COO^-	COO^-	COO^-	COO^-

Table B.3 20 monomer atactic PAA chain with random deprotonation, chain 3

Monomer	Tacticity	Charge density					
		f=0	f=0.2	f=0.4	f=0.6	f=0.8	f=1
1	Up	COOH	COOH	COO^-	COO^-	COO^-	COO^-
2	Up	COOH	COOH	COO^-	COO^-	COO^-	COO^-
3	Up	COOH	COOH	COO^-	COO^-	COO^-	COO^-
4	Down	COOH	COOH	COO^-	COO^-	COO^-	COO^-
5	Up	COOH	COO^-	COOH	COOH	COOH	COO^-
6	Down	COOH	COOH	COOH	COO^-	COO^-	COO^-
7	Up	COOH	COOH	COOH	COOH	COO^-	COO^-
8	Up	COOH	COOH	COO^-	COO^-	COO^-	COO^-
9	Up	COOH	COOH	COOH	COO^-	COO^-	COO^-
10	Up	COOH	COOH	COOH	COOH	COO^-	COO^-
11	Down	COOH	COO^-	COOH	COOH	COOH	COO^-
12	Down	COOH	COOH	COOH	COO^-	COO^-	COO^-
13	Up	COOH	COOH	COOH	COOH	COO^-	COO^-
14	Down	COOH	COOH	COO^-	COO^-	COO^-	COO^-
15	Up	COOH	COOH	COOH	COO^-	COO^-	COO^-
16	Up	COOH	COOH	COOH	COOH	COO^-	COO^-
17	Down	COOH	COOH	COO^-	COO^-	COO^-	COO^-
18	Down	COOH	COO^-	COOH	COOH	COOH	COO^-
19	Down	COOH	COOH	COO^-	COO^-	COO^-	COO^-
20	Up	COOH	COO^-	COOH	COOH	COOH	COO^-

Table B.4 20 monomer syndiotactic PAA chain with random deprotonation

Monomer	Tacticity	Charge density					
		f=0	f=0.2	f=0.4	f=0.6	f=0.8	f=1
1	Up	COOH	COOH	COO$^-$	COO$^-$	COO$^-$	COO$^-$
2	Down	COOH	COOH	COOH	COOH	COO$^-$	COO$^-$
3	Up	COOH	COOH	COOH	COO$^-$	COO$^-$	COO$^-$
4	Down	COOH	COOH	COOH	COO$^-$	COO$^-$	COO$^-$
5	Up	COOH	COO$^-$	COO$^-$	COOH	COOH	COO$^-$
6	Down	COOH	COOH	COO$^-$	COO$^-$	COO$^-$	COO$^-$
7	Up	COOH	COOH	COOH	COO$^-$	COO$^-$	COO$^-$
8	Down	COOH	COOH	COOH	COO$^-$	COO$^-$	COO$^-$
9	Up	COOH	COOH	COO$^-$	COOH	COO$^-$	COO$^-$
10	Down	COOH	COOH	COOH	COOH	COOH	COO$^-$
11	Up	COOH	COO$^-$	COOH	COO$^-$	COO$^-$	COO$^-$
12	Down	COOH	COOH	COO$^-$	COOH	COO$^-$	COO$^-$
13	Up	COOH	COOH	COO$^-$	COO$^-$	COO$^-$	COO$^-$
14	Down	COOH	COOH	COO$^-$	COO$^-$	COO$^-$	COO$^-$
15	Up	COOH	COOH	COO$^-$	COO$^-$	COO$^-$	COO$^-$
16	Down	COOH	COOH	COOH	COOH	COOH	COO$^-$
17	Up	COOH	COOH	COOH	COOH	COO$^-$	COO$^-$
18	Down	COOH	COO$^-$	COOH	COOH	COOH	COO$^-$
19	Up	COOH	COOH	COOH	COO$^-$	COO$^-$	COO$^-$
20	Down	COOH	COO$^-$	COOH	COO$^-$	COO$^-$	COO$^-$

Table B.5 20 monomer syndiotactic PAA chain with end deprotonation

Monomer	Tacticity	Charge density					
		f=0	f=0.2	f=0.4	f=0.6	f=0.8	f=1
1	Up	COOH	COOH	COOH	COOH	COOH	COO^-
2	Down	COOH	COOH	COOH	COOH	COOH	COO^-
3	Up	COOH	COOH	COOH	COOH	COOH	COO^-
4	Down	COOH	COOH	COOH	COOH	COOH	COO^-
5	Up	COOH	COOH	COOH	COOH	COO^-	COO^-
6	Down	COOH	COOH	COOH	COOH	COO^-	COO^-
7	Up	COOH	COOH	COOH	COOH	COO^-	COO^-
8	Down	COOH	COOH	COOH	COOH	COO^-	COO^-
9	Up	COOH	COOH	COOH	COO^-	COO^-	COO^-
10	Down	COOH	COOH	COOH	COO^-	COO^-	COO^-
11	Up	COOH	COOH	COOH	COO^-	COO^-	COO^-
12	Down	COOH	COOH	COOH	COO^-	COO^-	COO^-
13	Up	COOH	COOH	COO^-	COO^-	COO^-	COO^-
14	Down	COOH	COOH	COO^-	COO^-	COO^-	COO^-
15	Up	COOH	COOH	COO^-	COO^-	COO^-	COO^-
16	Down	COOH	COOH	COO^-	COO^-	COO^-	COO^-
17	Up	COOH	COO^-	COO^-	COO^-	COO^-	COO^-
18	Down	COOH	COO^-	COO^-	COO^-	COO^-	COO^-
19	Up	COOH	COO^-	COO^-	COO^-	COO^-	COO^-
20	Down	COOH	COO^-	COO^-	COO^-	COO^-	COO^-

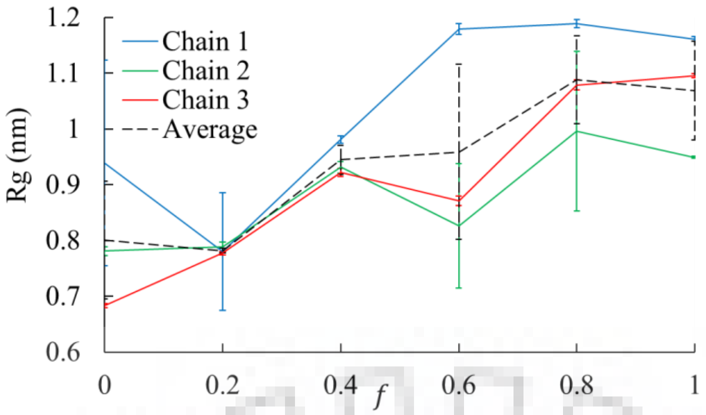

Figure B.1 Comparison of the R_g values against degree of deprotonation for three chains with different random deprotonation (Table B.1, B.2 and B.3) and their average values.

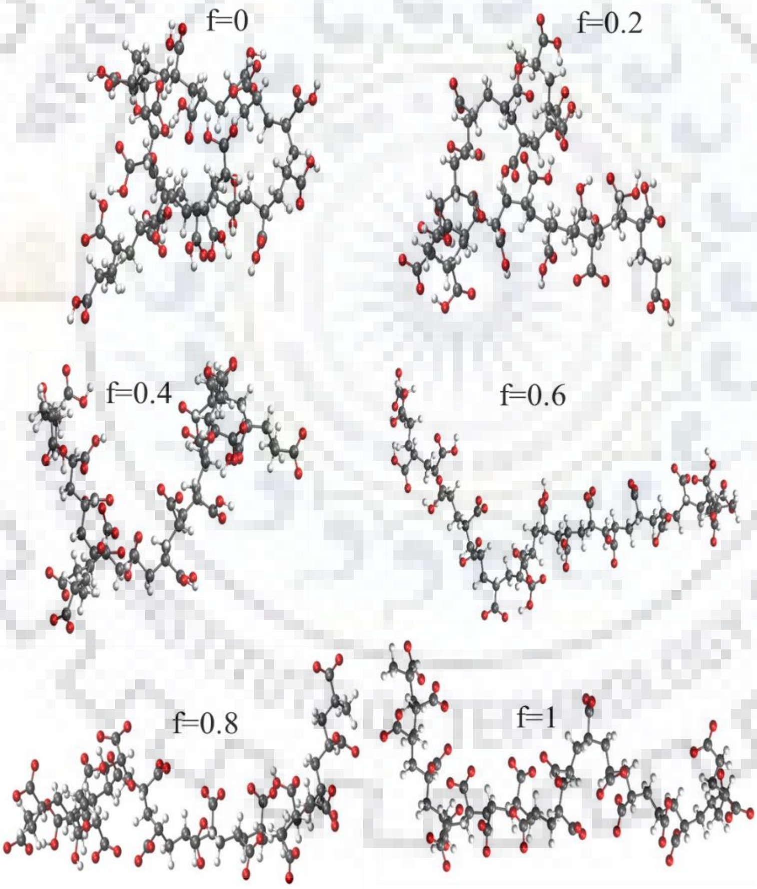

Figure B.2 Typical chain conformations of PAA at various degrees of deprotonation. Water molecules and counter ion are not shown here; aliphatic backbone carbon gray, hydrogen white, oxygen red color atoms are shown

B.1. PAA20 force-field

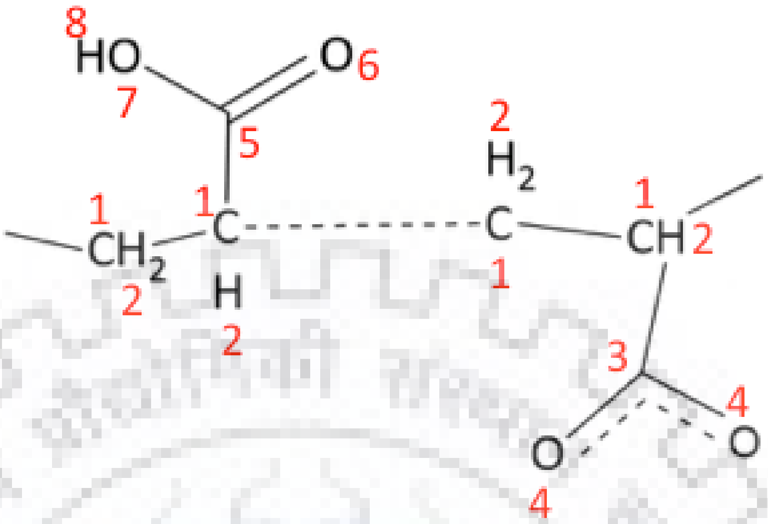

Figure B.3 Protonated (left) and deprotonated (right) repeating units in PAA20 with atom types shown in red color

Table B.6 Atom types in PAA20

Serial Number	Atom description	Atom type	Mass (amu)	σ_{ii} (nm)	ϵ_{ii} (kJ/mol)
1	Alkane Carbon	CR	12.011	0.387541	0.23012
2	Alkane Hydrogen	HCMM	1.0079	0.235197	0.092048
3	Carbon in COO^-	CO2M	12.011	0.356359	0.29288
4	Oxygen in COO^-	O2CM	15.9994	0.302905	0.50208
5	Carbon in C=O	C=O	12.011	0.356359	0.46024
6	Oxygen in C=O	O=C	15.9994	0.302905	0.50208
7	Oxygen in OH	OR	15.9994	0.315378	0.636386
8	Hydrogen in COOH	HOCO	1.0079	0.040001	0.192464

Table B.7 Pair types for intramolecular 1-4 interactions in PAA20

Atom type 1	Atom type 2	σ_{1-4} (nm)	ϵ_{1-4} (kJ/mol)
CR	CR	0.338541	0.04184
CR	HCMM	0.286869	0.062059
CR	CO2M	0.34745	0.110698
CR	O2CM	0.320723	0.144938
CR	C=O	0.34745	0.138768
CR	O=C	0.293997	0.144938
CR	OR	0.32696	0.163176
CR	HOCO	0.189271	0.089737
O=C	HCMM	0.242324	0.214978
O=C	CO2M	0.302905	0.38347
O=C	O2CM	0.276179	0.50208
O=C	C=O	0.302905	0.480705
O=C	O=C	0.249452	0.50208
O=C	OR	0.282415	0.565258
O=C	HOCO	0.144726	0.310857

Table B.8 Bond Energy Parameter for PAA20

Atom type 1	Atom type 2	$b_0\ (nm)$	$k_b (kJ\ mol^{-1}\ nm^{-2})$
CR	HCMM	0.1093	287014.9
CR	CR	0.1508	256422.3
CR	CO2M	0.151	230648
CR	C=O	0.1492	252327.8
CO2M	O2CM	0.1261	587519.8
C=O	O=C	0.1222	779866.6
C=O	OR	0.1355	349343.9
OR	HOCO	0.0981	445818.6

Table B.9 Angle Energy Parameters for PAA20

Atom type 1	Atom type 2	Atom type 3	θ_0(deg)	$k_\theta(kJ\ mol^{-1}\ rad^{-2})$
HCMM	CR	CR	110.549	383
HCMM	CR	CO2M	108.904	316.16
CR	CR	CR	109.608	512.48
CR	CR	CO2M	98.422	198.73
HCMM	CR	HCMM	108.836	310.74
CR	CR	C=O	107.517	467.91
HCMM	CR	C=O	108.385	391.44
O2CM	CO2M	O2CM	130.6	711.2
CR	CO2M	O2CM	114.689	728.07
CR	C=O	O=C	124.41	564.87
CR	C=O	OR	109.716	628.1
O=C	C=O	OR	124.425	695.55
C=O	OR	HOCO	111.948	351.09

Table B.10 Proper dihedral energy parameters for PAA20

Atom type 1	Atom type 2	Atom type 3	Atom type 4	ϕ_s(deg)	$k_\phi(kJmol^{-1})$	Multiplicity (n)
CR	CR	CR	HCMM	0	1.3389	1
CR	CR	CR	HCMM	180	-1.318	2
CR	CR	CR	HCMM	0	0.5523	3
CR	CR	CR	CR	0	0.2134	1
CR	CR	CR	CR	180	1.4267	2
CR	CR	CR	CR	0	0.6945	3
CR	CR	CR	CO2M	0	0.6276	3
HCMM	CR	CR	HCMM	0	0.5941	1
HCMM	CR	CR	HCMM	180	-2.8995	2
HCMM	CR	CR	HCMM	0	0.6569	3
HCMM	CR	CO2M	O2CM	0	-0.2218	3
CR	CR	CO2M	O2CM	180	2.6401	2

HCMM	CR	CR	CO2M	0	-0.2929	3
CR	CR	CR	C=O	0	0.1381	1
CR	CR	CR	C=O	180	-0.3264	2
CR	CR	CR	C=O	0	0.2971	3
CR	CR	C=O	O=C	0	1.7238	1
CR	CR	C=O	O=C	180	0.2929	2
CR	CR	C=O	O=C	0	0.682	3
CR	CR	C=O	OR	0	-0.2469	1
CR	CR	C=O	OR	180	-0.6987	2
CR	CR	C=O	OR	0	0.4226	3
HCMM	CR	CR	C=O	0	-0.5356	1
HCMM	CR	CR	C=O	180	0.1213	2
CR	C=O	OR	HOCO	0	-2.4393	1
CR	C=O	OR	HOCO	180	10.6232	2
CR	C=O	OR	HOCO	0	-1.1422	3
HCMM	CR	C=O	O=C	0	1.3807	1
HCMM	CR	C=O	O=C	180	-2.9455	2
HCMM	CR	C=O	O=C	0	0.6443	3
HCMM	CR	C=O	OR	180	-1.3054	2
HCMM	CR	C=O	OR	0	0.6904	3
O=C	C=O	OR	HOCO	0	3.4769	1
O=C	C=O	OR	HOCO	180	12.87	2
O=C	C=O	OR	HOCO	0	-0.1213	3

Table B.11 Improper dihedral energy parameters for PAA20

Atom type 1	Atom type 2	Atom type 3	Atom type 4	$\varphi_0(deg)$	$k_\varphi(kJmol^{-1}rad^{-2})$
CO2M	O2CM	CR	O2CM	0	107.1941
C=O	OR	CR	O=C	0	84.9101

B.2. DOX force-field

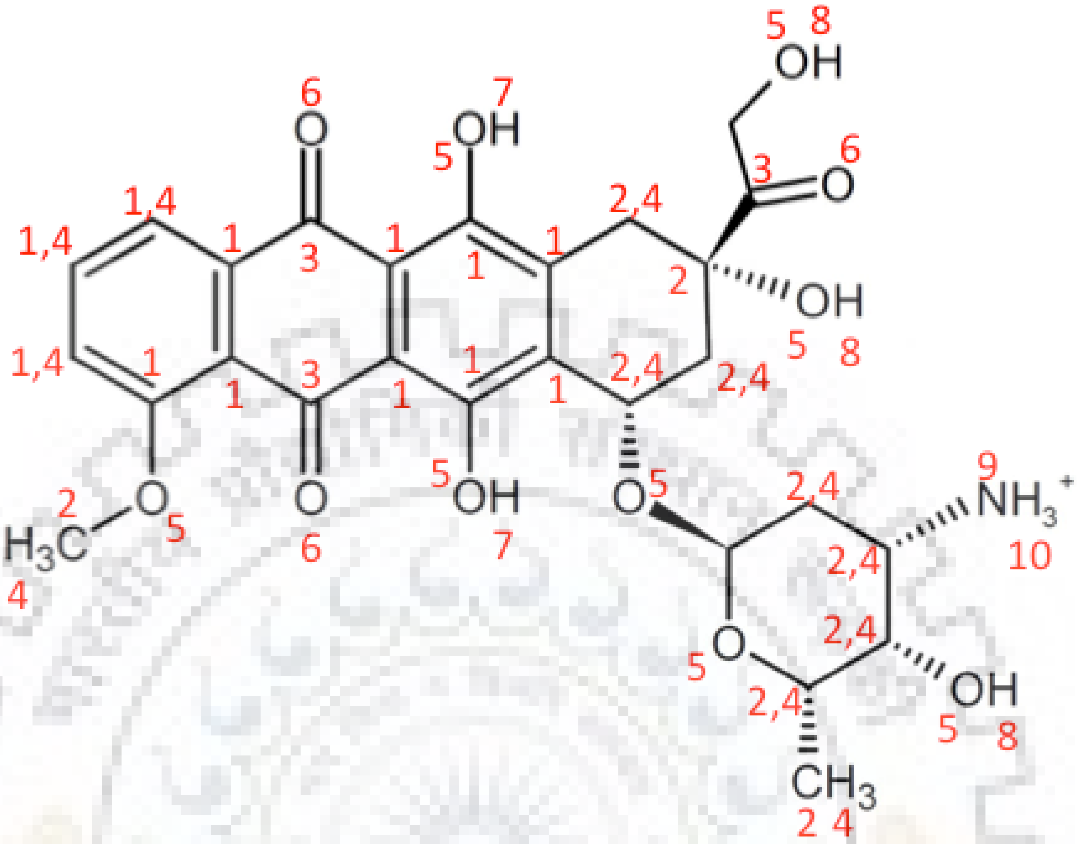
5 8
OH
6
O
7
OH
5
3
6
O
1,4
2,4
1,4
1
3
1
1
1
2
OH
5 8
1,4
1
3
1
1
2,4
2,4
1
1
1
2
O
5
H_3C
4
O
6
5
OH
7
O
5
2,4
9
NH_3^+
10
2,4
2,4
O
5
2,4
OH
5 8
CH_3
2 4

Figure B.4 Structure of cationic anticancer drug doxorubicin (DOX) with atom types shown in red color

Table B.12 Atom types for DOX

Serial Number	Atom name	Atom type	Mass (amu)	σ_{ii} (nm)	ϵ_{ii} (kJ/mol)
1	Benzene carbon	CB	12.011	0.355005	0.29288
2	Alkane carbon	CR	12.011	0.387541	0.23012
3	Carbon in C=O	C=O	12.011	0.356359	0.46024
4	Alkane Hydrogen	HCMM	1.0079	0.235197	0.092048
5	Oxygen in OH	OR	15.9994	0.315378	0.636386
6	Oxygen in C=O	O=C	15.9994	0.302905	0.50208
7	Hydrogen in OH linked to benzene	HOCC	1.0079	0.040001	0.192464

8	Hydrogen in OH	HOR	1.0079	0.040001	0.192464
9	Nitrogen in NH_3^+	NRP	14.0067	0.329632	0.8368
10	Hydrogen in NH_3^+	HNRP	1.0079	0.040001	0.192464

Table B.13 Pair types for intramolecular 1-4 interactions in DOX

Atom type 1	Atom type 2	σ_{1-4} (nm)	ϵ_{1-4} (kJ/mol)
CR	CB	0.346773	0.110698
CR	CR	0.338541	0.04184
CR	C=O	0.34745	0.138768
CR	HCMM	0.286869	0.062059
CR	OR	0.32696	0.163176
CR	O=C	0.293997	0.144938
CR	HOCC	0.189271	0.089737
CR	HOR	0.189271	0.089737
CR	NRP	0.334087	0.187114
CR	HNRP	0.189271	0.089737
O=C	CB	0.302228	0.38347
O=C	C=O	0.302905	0.480705
O=C	HCMM	0.242324	0.214978
O=C	OR	0.282415	0.565258
O=C	O=C	0.249452	0.50208
O=C	HOCC	0.144726	0.310857
O=C	HOR	0.144726	0.310857
O=C	NRP	0.289542	0.648182
O=C	HNRP	0.144726	0.310857

Table B.14 Bond energy parameters for DOX

Atom type 1	Atom type 2	b_0 (nm)	$k_b(kJ\ mol^{-1}\ nm^{-2})$
CR	CR	0.1508	256422.3
CR	HCMM	0.1093	287014.9
CR	CB	0.1486	298517.5
CR	OR	0.1418	303937.5
CB	CB	0.1374	335613.7
CR	C=O	0.1492	252327.8
CB	OR	0.1376	338083.1
CB	C=O	0.1457	270273.8
C=O	O=C	0.1222	779866.6
CB	HCMM	0.1084	319534.6
OR	HOCC	0.0973	472074.9
OR	HOR	0.0972	469365.3
CR	NRP	0.148	231490.7
NRP	HNRP	0.1028	371144.2

Table B.15 Angle energy parameters for DOX

Atom type 1	Atom type 2	Atom type 3	θ_0(deg)	$k_\theta(kJ\ mol^{-1}\ rad^{-2})$
CB	CB	CB	119.977	402.88
CB	CB	CR	120.419	483.57
CB	CB	OR	116.495	582.94
CB	CB	C=O	114.475	480.57
CB	CB	HCMM	120.571	339.05
CR	CR	CR	109.608	512.48
CR	CR	HCMM	110.549	383
HCMM	CR	HCMM	108.836	310.74
CB	CR	CR	108.617	455.27
CB	CR	HCMM	109.491	377.58
CB	CR	OR	107.978	528.74
CR	CR	OR	108.133	597.39

HCMM	CR	OR	108.577	470.32
CR	CR	C=O	107.517	467.91
OR	CR	C=O	104.112	317.97
CB	C=O	CB	115.566	561.86
CB	C=O	O=C	119.968	442.02
CB	OR	CR	102.846	647.37
CB	OR	HOCC	105.409	437.2
CR	OR	HOR	106.503	477.55
CR	C=O	O=C	124.41	564.87
CR	C=O	CR	118.016	693.14
C=O	CR	HCMM	108.385	391.44
CR	OR	CR	106.926	720.84
OR	CR	OR	111.368	696.15
CR	CR	NRP	106.493	710.01
NRP	CR	HCMM	106.224	525.13
CR	NRP	HNRP	111.206	346.87
HNRP	NRP	HNRP	107.787	348.08

Table B.16 Proper dihedral energy parameters for DOX

Atom type 1	Atom type 2	Atom type 3	Atom type 4	ϕ_s(deg)	$k_\phi(kJmol^{-1})$	Multiplicity (n)
CB	CB	CB	OR	180	14.644	2
CB	CB	CR	CR	180	0.9414	2
CB	CB	CR	HCMM	180	-0.8786	2
CB	CB	CR	HCMM	0	0.8201	3
CB	CB	OR	HOCC	180	5.8618	2
CB	CR	CR	CR	0	0.6276	3
CB	CR	CR	HCMM	0	0.8159	3
CB	CR	OR	CR	0	0.4184	3
CB	CB	CR	OR	0	0.3138	3
CB	CB	C=O	CB	180	5.23	2

CB	CB	C=O	O=C	180	4.7196	2
CB	CB	OR	CR	180	9.1671	2
CB	OR	CR	HCMM	0	0.2218	3
CR	CR	OR	CR	0	-1.4267	1
CR	CR	OR	CR	180	1.5816	2
CR	CR	OR	CR	0	1.5816	3
CR	CR	CR	HCMM	0	1.3389	1
CR	CR	CR	HCMM	180	-1.318	2
CR	CR	CR	HCMM	0	0.5523	3
CR	CR	OR	HOR	180	0.5648	2
CR	CR	OR	HOR	0	0.4937	3
CR	CR	C=O	O=C	0	1.7238	1
CR	CR	C=O	O=C	180	0.2929	2
CR	CR	C=O	O=C	0	0.682	3
CR	CR	C=O	CR	0	0.2134	1
CR	CR	C=O	CR	180	0.3682	2
CR	CR	C=O	CR	0	1.1422	3
CR	CR	CR	CR	0	0.6945	3
CR	CR	CR	OR	0	-1.4393	1
CR	CR	CR	OR	180	3.6777	2
CR	CR	CR	OR	0	0.9958	3
CR	CR	CR	C=O	0	0.1381	1
CR	CR	CR	C=O	180	-0.3264	2
CR	CR	CR	C=O	0	0.2971	3
CR	OR	CR	CR	180	1.5816	2
CR	OR	CR	CR	0	1.5816	3
CR	OR	CR	OR	0	0.4812	1
CR	OR	CR	OR	180	-1.4853	2
CR	OR	CR	OR	0	1.5104	3
CR	OR	CR	HCMM	0	1.1924	1
CR	OR	CR	HCMM	180	0.6694	2

CR	OR	CR	HCMM	0	1.1924	3
CR	C=O	CR	HCMM	0	-0.1506	1
CR	C=O	CR	HCMM	180	0.1799	2
CR	C=O	CR	HCMM	0	1.1129	3
CR	C=O	CR	OR	0	1.1506	3
C=O	CB	CB	OR	180	4.184	2
HCMM	CR	CR	HCMM	0	0.5941	1
HCMM	CR	CR	HCMM	180	-2.8995	2
HCMM	CR	CR	HCMM	0	0.6569	3
HCMM	CR	CR	OR	0	-1.3682	1
HCMM	CR	CR	OR	180	2.2426	2
HCMM	CR	CR	OR	0	0.5858	3
HCMM	CR	CR	C=O	0	-0.5356	1
HCMM	CR	CR	C=O	180	0.1213	2
OR	CR	C=O	O=C	0	-0.8284	1
OR	CR	C=O	O=C	180	1.5272	2
OR	CR	C=O	O=C	0	-0.2929	3
HOR	OR	CR	C=O	0	-3.456	1
HOR	OR	CR	C=O	180	-3.4727	2
HOR	OR	CR	C=O	0	0.5899	3
O=C	C=O	CR	HCMM	0	1.3807	1
O=C	C=O	CR	HCMM	180	-2.9455	2
O=C	C=O	CR	HCMM	0	0.6443	3
HCMM	CR	OR	HOR	0	1.2468	1
HCMM	CR	OR	HOR	180	-0.5774	2
HCMM	CR	OR	HOR	0	0.7238	3
CR	CR	CR	CR	180	1.4267	2
CR	CR	CR	CR	0	0.6945	3
CR	CR	CR	NRP	0	-1.3556	1
CR	CR	CR	NRP	180	1.1506	2
CR	CR	CR	NRP	0	1.2343	3

CR	CR	NRP	HNRP	0	0.3891	3
HCMM	CR	CR	NRP	0	1.4477	1
HCMM	CR	CR	NRP	180	-1.1088	2
HCMM	CR	CR	NRP	0	0.5816	3
OR	CR	CR	OR	0	0.8535	1
OR	CR	CR	OR	180	2.9246	2
OR	CR	CR	OR	0	2.0083	3
HNRP	NRP	CR	HCMM	0	0.5439	3

Table B.17 Improper dihedral energy parameters for DOX

Atom type 1	Atom type 2	Atom type 3	Atom type 4	$\varphi_0(deg)$	$k_\varphi(kJmol^{-1}rad^{-2})$
CB	CB	CB	CR	0	24.0915
CB	CB	CB	OR	0	28.9031
C=O	CB	CB	O=C	0	78.291
CB	CB	C=O	CB	0	16.259
CB	CB	CB	HCMM	0	9.0291
C=O	CR	CR	O=C	0	87.9226

B.3. Water (SPC216) force-field

Table B.18 Atom types for water

Atom name	Atom type	Mass (amu)	Charge
Water oxygen	OW	15.9994	-0.82
Hydrogen	HW	1.008	0.41

Table B.19 Bond energy parameters for water

Atom type 1	Atom type 2	$b_0\ (nm)$	$k_b(kJ\ mol^{-1}\ nm^{-2})$
OW	HW	0.1	345000

Table B.20 Angle energy parameters for water

Atom type 1	Atom type 2	Atom type 3	θ_0(deg)	$k_\theta(kJ\ mol^{-1}\ rad^{-2})$
HW	OW	HW	109.47	383

B.4. Ions force-field

Table B.21 Atom types of ions

Atom name	Atom type	Mass (amu)	Charge
Sodium	NA+	22.9898	+1
Chlorine	CL-	35.453	-1

B.5. Acetate force-field

Table B.22 Atom Types in acetate

Serial Number	Atom description	Atom type	Mass (amu)	σ_{ii} (nm)	ϵ_{ii} (kJ/mol)
1	Alkane Carbon	CR	12.011	0.387541	0.23012
2	Alkane Hydrogen	HCMM	1.0079	0.235197	0.092048
3	Carbon in COO^-	CO2M	12.011	0.356359	0.29288
4	Oxygen in COO^-	O2CM	15.9994	0.302905	0.50208

Table B.23 Pair types for intramolecular 1-4 interactions in acetate

Atom type 1	Atom type 2	σ_{1-4} (nm)	ϵ_{1-4} (kJ/mol)
CR	CR	0.338541	0.04184
CR	HCMM	0.286869	0.062059
CR	CO2M	0.34745	0.110698
CR	O2CM	0.320723	0.144938

Table B.24 Bond Energy Parameter for acetate

Atom type 1	Atom type 2	$b_0\ (nm)$	$k_b(kJ\ mol^{-1}\ nm^{-2})$
CR	HCMM	0.1093	287014.9
CR	CO2M	0.151	230648
CO2M	O2CM	0.1261	587519.8

Table B.25 Angle Energy Parameters for acetate

Atom type 1	Atom type 2	Atom type 3	θ_0(deg)	$k_\theta(kJ\ mol^{-1}\ rad^{-2})$
HCMM	CR	CO2M	108.904	316.16
HCMM	CR	HCMM	108.836	310.74
O2CM	CO2M	O2CM	130.6	711.2
CR	CO2M	O2CM	114.689	728.07

Table B.26 Proper dihedral energy parameters for acetate

Atom type 1	Atom type 2	Atom type 3	Atom type 4	ϕ_s(deg)	$k_\phi(kJmol^{-1})$	Multiplicity (n)
O2CM	CO2M	CR	HCMM	0	-0.2218	3

Table B. 27 Improper dihedral energy parameters for acetate

Atom type 1	Atom type 2	Atom type 3	Atom type 4	$\varphi_0(deg)$	$k_\varphi(kJmol^{-1}rad^{-2})$
CO2M	O2CM	CR	O2CM	0	107.1941

B.6. Acetic acid force-field

Table B.28 Atom Types in acetic acid

Serial Number	Atom description	Atom type	Mass (amu)	σ_{ii} (nm)	ϵ_{ii} (kJ/mol)
1	Alkane Carbon	CR	12.011	0.387541	0.23012
2	Alkane Hydrogen	HCMM	1.0079	0.235197	0.092048
3	Carbon in C=O	C=O	12.011	0.356359	0.46024
4	Oxygen in C=O	O=C	15.9994	0.302905	0.50208
5	Oxygen in OH	OR	15.9994	0.315378	0.636386
6	Hydrogen in COOH	HOCO	1.0079	0.040001	0.192464

Table B.29 Pair types for intramolecular 1-4 interactions in acetic acid

Atom type 1	Atom type 2	σ_{1-4} (nm)	ϵ_{1-4} (kJ/mol)
CR	CR	0.338541	0.04184
CR	HCMM	0.286869	0.062059
CR	C=O	0.34745	0.138768
CR	O=C	0.293997	0.144938
CR	OR	0.32696	0.163176
CR	HOCO	0.189271	0.089737
O=C	HCMM	0.242324	0.214978
O=C	C=O	0.302905	0.480705
O=C	O=C	0.249452	0.50208
O=C	OR	0.282415	0.565258
O=C	HOCO	0.144726	0.310857

Table B.30 Bond Energy Parameter for acetic acid

Atom type 1	Atom type 2	$b_0\ (nm)$	$k_b(kJ\ mol^{-1}\ nm^{-2})$
CR	HCMM	0.1093	287014.9
CR	C=O	0.1492	252327.8
C=O	O=C	0.1222	779866.6

C=O	OR	0.1355	349343.9
OR	HOCO	0.0981	445818.6

Table B.31 Angle Energy Parameters for acetic acid

Atom type 1	Atom type 2	Atom type 3	θ_0(deg)	$k_\theta(kJ\ mol^{-1}\ rad^{-2})$
HCMM	CR	HCMM	108.836	310.74
HCMM	CR	C=O	108.385	391.44
CR	C=O	O=C	124.41	564.87
CR	C=O	OR	109.716	628.1
O=C	C=O	OR	124.425	695.55
C=O	OR	HOCO	111.948	351.09

Table B.32 Proper dihedral energy parameters for acetic acid

Atom type 1	Atom type 2	Atom type 3	Atom type 4	ϕ_s(deg)	$k_\phi(kJmol^{-1})$	Multiplicity (n)
CR	C=O	OR	HOCO	0	-2.4393	1
CR	C=O	OR	HOCO	180	10.6232	2
CR	C=O	OR	HOCO	0	-1.1422	3
HCMM	CR	C=O	O=C	0	1.3807	1
HCMM	CR	C=O	O=C	180	-2.9455	2
HCMM	CR	C=O	O=C	0	0.6443	3
HCMM	CR	C=O	OR	180	-1.3054	2
HCMM	CR	C=O	OR	0	0.6904	3
O=C	C=O	OR	HOCO	0	3.4769	1
O=C	C=O	OR	HOCO	180	12.87	2
O=C	C=O	OR	HOCO	0	-0.1213	3

Table B.33 Improper dihedral energy parameters for acetic acid

Atom type 1	Atom type 2	Atom type 3	Atom type 4	$\varphi_0 (deg)$	$k_\varphi (kJmol^{-1}rad^{-2})$
C=O	O=C	OR	CR	0	84.9101

B.7. Maleic acid force-field

Table B.34 Atom Types in maleic acid

Serial Number	Atom description	Atom type	Mass (amu)	σ_{ii} (nm)	ϵ_{ii} (kJ/mol)
1	Alkene Carbon	C=C	12.011	0.372396	0.284512
2	Alkane Hydrogen	HCMM	1.0079	0.235197	0.092048
3	Carbon in C=O	C=O	12.011	0.356359	0.46024
4	Oxygen in C=O	O=C	15.9994	0.302905	0.50208
5	Oxygen in OH	OR	15.9994	0.315378	0.636386
6	Hydrogen in COOH	HOCO	1.0079	0.040001	0.192464

Table B.35 Pair types for intramolecular 1-4 interactions in maleic acid

Atom type 1	Atom type 2	σ_{1-4} (nm)	ϵ_{1-4} (kJ/mol)
O=C	C=C	0.310924	0.377952
O=C	HCMM	0.242324	0.214978
O=C	C=O	0.302905	0.480705
O=C	O=C	0.249452	0.50208
O=C	OR	0.282415	0.565258
O=C	HOCO	0.144726	0.310857

Table B.36 Bond Energy Parameter for maleic acid

Atom type 1	Atom type 2	$b_0\ (nm)$	$k_b (kJ\ mol^{-1}\ nm^{-2})$
C=C	HCMM	0.1083	311344.8
C=C	C=C	0.1333	572403.8

C=C	C=O	0.1468	274910.6
C=O	O=C	0.1222	779866.6
C=O	OR	0.1355	349343.9
OR	HOCO	0.0981	445818.6

Table B.37 Angle Energy Parameters for maleic acid

Atom type 1	Atom type 2	Atom type 3	θ_0(deg)	$k_\theta(kJ\ mol^{-1}\ rad^{-2})$
HCMM	C=C	HCMM	121.004	322.18
HCMM	C=C	C=O	117.291	293.27
C=C	C=C	C=O	111.297	328.2
C=C	C=O	O=C	122.623	122.623
C=C	C=O	OR	106.51	106.51
O=C	C=O	OR	124.425	124.425
C=O	OR	HOCO	111.948	111.948

Table B.38 Proper dihedral energy parameters for maleic acid

Atom type 1	Atom type 2	Atom type 3	Atom type 4	ϕ_s(deg)	$k_\phi(kJmol^{-1})$	Multiplicity (n)
C=C	C=C	C=O	O=C	0	0.7573	1
C=C	C=C	C=O	O=C	180	4.138	2
C=C	C=C	C=O	OR	0	-0.2971	1
C=C	C=C	C=O	OR	180	3.0669	2
C=C	C=O	OR	HOCO	0	0.5356	1
C=C	C=O	OR	HOCO	180	9.4558	2
C=C	C=O	OR	HOCO	0	0.5397	3
HCMM	C=C	C=C	HCMM	180	25.104	2
HCMM	C=C	C=O	O=C	180	4.2802	2
HCMM	C=C	C=O	OR	0	0.7489	1
HCMM	C=C	C=O	OR	180	3.2217	2
HCMM	C=C	C=O	OR	0	0.4058	3

C=O	C=C	C=C	C=O	180	3.7656	2
O=C	C=O	OR	HOCO	0	3.4769	1
O=C	C=O	OR	HOCO	180	12.87	2
O=C	C=O	OR	HOCO	0	-0.1213	3

Table B.39 Improper dihedral energy parameters for maleic acid

Atom type 1	Atom type 2	Atom type 3	Atom type 4	$\varphi_0(deg)$	$k_\varphi(kJmol^{-1}rad^{-2})$
C=C	C=O	C=C	HCMM	0	7.23
C=O	OR	C=C	O=C	0	76.4835

B.8. Oleate force-field

Table B.40 Atom Types in oleate

Serial Number	Atom description	Atom type	Mass (amu)	σ_{ii} (nm)	ϵ_{ii} (kJ/mol)
1	Alkane Carbon	CR	12.011	0.387541	0.23012
2	Alkane Hydrogen	HCMM	1.0079	0.235197	0.092048
3	Alkene Carbon	C=C	12.011	0.372396	0.284512
4	Carbon in COO^-	CO2M	12.011	0.356359	0.29288
5	Oxygen in COO^-	O2CM	15.9994	0.302905	0.50208

Table B.41 Pair types for intramolecular 1-4 interactions in oleate

Atom type 1	Atom type 2	σ_{1-4} (nm)	ϵ_{1-4} (kJ/mol)
CR	CR	0.338541	0.04184
CR	HCMM	0.286869	0.062059
CR	C=C	0.355469	0.109105
CR	CO2M	0.34745	0.110698
CR	O2CM	0.320723	0.144938

Table B.42 Bond Energy Parameter for oleate

Atom type 1	Atom type 2	$b_0\ (nm)$	$k_b (kJ\ mol^{-1}\ nm^{-2})$
CR	HCMM	0.1093	287014.9
CR	CO2M	0.151	230648
CO2M	O2CM	0.1261	587519.8
CR	CR	0.1508	256422.3
CR	C=C	0.1482	273344.9
C=C	HCMM	0.1083	311344.8
C=C	C=C	0.1333	572403.8

Table B.43 Angle Energy Parameters for oleate

Atom type 1	Atom type 2	Atom type 3	θ_0(deg)	$k_\theta (kJ\ mol^{-1}\ rad^{-2})$
HCMM	CR	CO2M	108.904	316.16
HCMM	CR	HCMM	108.836	310.74
O2CM	CO2M	O2CM	130.6	711.2
CR	CO2M	O2CM	114.689	728.07
HCMM	CR	CR	110.549	383
CR	CR	CR	109.608	512.48
C=C	CR	CR	109.445	443.23
C=C	CR	HCMM	110.292	380.59
CR	C=C	HCMM	120.108	268.59
CR	C=C	C=C	122.141	404.68
HCMM	C=C	C=C	121.004	322.18
CR	CR	CO2M	98.422	198.73

Table B.44 Proper dihedral energy parameters for oleate

Atom type 1	Atom type 2	Atom type 3	Atom type 4	ϕ_s(deg)	$k_\phi (kJmol^{-1})$	Multiplicity (n)
CR	CR	CR	HCMM	0	1.3389	1
CR	CR	CR	HCMM	180	-1.318	2
CR	CR	CR	HCMM	0	0.5523	3
CR	CR	CR	CR	0	0.2134	1
CR	CR	CR	CR	180	1.4267	2
CR	CR	CR	CR	0	0.6945	3
HCMM	CR	CR	HCMM	0	0.5941	1
HCMM	CR	CR	HCMM	180	-2.8995	2
HCMM	CR	CR	HCMM	0	0.6569	3
CR	CR	CR	C=C	0	-0.615	1
CR	CR	CR	C=C	180	0.9163	2
CR	CR	CR	C=C	0	1.2217	3
CR	CR	C=C	HCMM	0	0.1548	1
CR	CR	C=C	HCMM	0	0.7489	3
CR	CR	C=C	C=C	0	-1.0334	1
CR	CR	C=C	C=C	180	0.5732	2
HCMM	CR	CR	C=C	0	0.6736	1
HCMM	CR	CR	C=C	180	-0.8577	2
HCMM	CR	CR	C=C	0	0.3012	3
CR	C=C	C=C	CR	0	-0.8452	1
CR	C=C	C=C	CR	180	25.104	2
HCMM	CR	C=C	HCMM	0	-1.0962	1
HCMM	CR	C=C	HCMM	180	-0.477	2
HCMM	CR	C=C	HCMM	0	0.4351	3
HCMM	CR	C=C	C=C	0	1.0502	1
HCMM	CR	C=C	C=C	180	-0.8577	2
HCMM	CR	C=C	C=C	0	-1.1213	3
CR	CR	CR	CO2M	0	0.6276	3

CR	CR	CO2M	O2CM	180	2.6401	2
HCMM	CR	CR	CO2M	0	-0.2929	3
HCMM	CR	CO2M	O2CM	0	-0.2218	3

Table B. 45 Improper dihedral energy parameters for oleate

Atom type 1	Atom type 2	Atom type 3	Atom type 4	$\varphi_0(deg)$	$k_\varphi(kJmol^{-1}rad^{-2})$
CO2M	O2CM	CR	O2CM	0	107.1941
C=C	C=C	CR	HCMM	0	7.8324

REFERENCES

Abdel-Halim, Heba, Daniela Traini, David Hibbs, Simon Gaisford, and Paul Young. 2011. “Modelling of Molecular Phase Transitions in Pharmaceutical Inhalation Compounds: An in Silico Approach.” *European Journal of Pharmaceutics and Biopharmaceutics*.

Accelrys Inc. 2017. “BIOVIA Materials Studio.” *Http://Accelrys.Com/*.

Adnan, Ashfaq, Robert Lam, Hanning Chen, Jessica Lee, Daniel J. Schaffer, Amanda S. Barnard, George C. Schatz, Dean Ho, and Wing Kam Liu. 2011. “Atomistic Simulation and Measurement of PH Dependent Cancer Therapeutic Interactions with Nanodiamond Carrier.” *Molecular Pharmaceutics* 8(2):368–74.

Ajay and Mark A. Murcko. 1995. “Computational Methods to Predict Binding Free Energy in Ligand-Receptor Complexes.” *Journal of Medicinal Chemistry* 38(26):4953–67.

Alarcón, F., G. Pérez-Hernández, E. Pérez, and A. Gama Goicochea. 2013. “Coarse-Grained Simulations of the Salt Dependence of the Radius of Gyration of Polyelectrolytes as Models for Biomolecules in Aqueous Solution.” *European Biophysics Journal* 42(9):661–72.

Allen, Mike P. and Dominic J. Tildesley. 1989. *Computer Simulation of Liquids*. New York, USA: Oxford university press.

Almeida, Hugo, Maria Helena Amaral, and Paulo Lobão. 2012. “Temperature and PH Stimuli-Responsive Polymers and Their Applications in Controlled and Selfregulated Drug Delivery.” *Journal of Applied Pharmaceutical Science* 2(6):01–10.

Alper, Howard E. and Terry R. Stouch. 1995. “Orientation and Diffusion of a Drug Analog in Biomembranes: Molecular Dynamics Simulations.” *The Journal of Physical Chemistry* 99(15):5724–31.

Arnarez, Clément, Jaakko J. Uusitalo, Marcelo F. Masman, Helgi I. Ingólfsson, Djurre H. De Jong, Manuel N. Melo, Xavier Periole, Alex H. De Vries, and Siewert J. Marrink. 2015. “Dry Martini, a Coarse-Grained Force Field for Lipid Membrane Simulations with Implicit Solvent.” *Journal of Chemical Theory and Computation* 11(1):260–75.

Athawale, Manoj V., Gaurav Goel, Tuhin Ghosh, Thomas M. Truskett, and Shekhar Garde. 2007. “Effects of Lengthscales and Attractions on the Collapse of Hydrophobic Polymers in Water.” *Proceedings of the National Academy of Sciences* 104(3):733–38.

Atkins, P. W. and Julio. De Paula. 2011. *Physical Chemistry for the Life Sciences*. New York: W.H. Freeman and Co.

Ayappa, K. G., Ateeque Malani, Patil Kalyan, and Foram Thakkar. 2007. “Molecular Simulations: Probing Systems from the Nanoscale to Mesoscale.” *Journal of the Indian Institute of Science* 87(1):35–60.

Bag, Dibyendu S. and K. U. Bhasker Rao. 2006. “Smart Polymers and Their Applications.” *Journal of Polymer Materials* 23(3):225–48.

Baginski, M., H. Resat, and J. A. McCammon. 1997. “Molecular Properties of Amphotericin B Membrane Channel: A Molecular Dynamics Simulation.” *Molecular Pharmacology* 52(4):560–70.

Barducci, Alessandro, Giovanni Bussi, and Michele Parrinello. 2008. “Well-Tempered Metadynamics: A Smoothly Converging and Tunable Free-Energy Method.” *Physical Review Letters* 100(2):020603.

Barton, Allan F. M. 1991. *CRC Handbook of Solubility Parameters and Other Cohesion Parameters*. 2nd ed. Boca Raton, Florida: CRC press.

Bemporad, D., C. Luttmann, and J. W. Essex. 2005. “Behaviour of Small Solutes and Large Drugs in a Lipid Bilayer from Computer Simulations.” *Biochimica et Biophysica Acta - Biomembranes* 1718(1–2):1–21.

Berghold, Gerd, Paul van der Schoot, and Christian Seidel. 1997. “Equilibrium Charge Distribution on Weak Polyelectrolytes.” *The Journal of Chemical Physics* 107(19):8083–88.

Bernini, María C., David Fairen-Jimenez, Marcelo Pasinetti, Antonio J. Ramirez-Pastor, and Randall Q. Snurr. 2014. “Screening of Bio-Compatible Metal–Organic Frameworks as Potential Drug Carriers Using Monte Carlo Simulations.” *Journal of Materials Chemistry B* 2(7):766–74.

Beveridge, D. L. and F. M. DiCapua. 1989. “Free Energy Via Molecular Simulation: Applications to Chemical and Biomolecular Systems.” *Annual Review of Biophysics and Biophysical Chemistry* 18(1):431–92.

Birru, Woldeamanuel A., Dallas B. Warren, Sifei Han, Hassan Benameur, Christopher J. H. Porter, Colin W. Pouton, and David K. Chalmers. 2017. "Computational Models of the Gastrointestinal Environment. 2. Phase Behavior and Drug Solubilization Capacity of a Type I Lipid-Based Drug Formulation after Digestion." *Molecular Pharmaceutics* 14(3):580–92.

Birru, Woldeamanuel A., Dallas B. Warren, Stephen J. Headey, Hassan Benameur, Christopher J. H. Porter, Colin W. Pouton, and David K. Chalmers. 2017. "Computational Models of the Gastrointestinal Environment. 1. The Effect of Digestion on the Phase Behavior of Intestinal Fluids." *Molecular Pharmaceutics* 14(3):566–79.

Boggara, Mohan Babu and Ramanan Krishnamoorti. 2010. "Partitioning of Nonsteroidal Antiinflammatory Drugs in Lipid Membranes: A Molecular Dynamics Simulation Study." *Biophysical Journal* 98(4):586–95.

Börjesson, U. and P. H. Hünenberger. 2001. "Explicit-Solvent Molecular Dynamics Simulation at Constant PH: Methodology and Application to Small Amines." *Journal of Chemical Physics* 114(22):9706–19.

Bulo, Rosa E., Davide Donadio, Alessandro Laio, Ferenc Molnar, Jens Rieger, and Michele Parrinello. 2007. "'Site Binding' of Ca2+ Ions to Polyacrylates in Water: A Molecular Dynamics Study of Coiling and Aggregation." *Macromolecules* 40:3437–42.

Carpenter, Timothy S., Daniel A. Kirshner, Edmond Y. Lau, Sergio E. Wong, Jerome P. Nilmeier, and Felice C. Lightstone. 2014. "A Method to Predict Blood-Brain Barrier Permeability of Drug-Like Compounds Using Molecular Dynamics Simulations." *Biophysical Journal* 107(3):630–41.

Chen, Ting, Suzanne M. D'Addio, Michael T. Kennedy, Aleksander Swietlow, Ioannis G. Kevrekidis, Athanassios Z. Panagiotopoulos, and Robert K. Prud'homme. 2009. "Protected Peptide Nanoparticles: Experiments and Brownian Dynamics Simulations of the Energetics of Assembly." *Nano Letters* 9(6):2218–22.

Cherkasov, Artem, Eugene N. Muratov, Denis Fourches, Alexandre Varnek, Igor I. Baskin, Mark Cronin, John Dearden, Paola Gramatica, Yvonne C. Martin, Roberto Todeschini, Viviana Consonni, Victor E. Kuz'min, Richard Cramer, Romualdo Benigni, Chihae Yang, James Rathman, Lothar Terfloth, Johann Gasteiger, Ann Richard, and Alexander Tropsha. 2014.

"QSAR Modeling: Where Have You Been? Where Are You Going To?" *Journal of Medicinal Chemistry* 57(12):4977–5010.

Cho, K. and J. D. Joannopoulos. 1992. "Ergodicity and Dynamical Properties of Constant-Temperature Molecular Dynamics." *Physical Review A* 45(10):7089–97.

Chockalingam, Rajalakshmi and Upendra Natarajan. 2015. "Self-Association Behaviour of *Atactic* Polymethacrylic Acid in Aqueous Solution Investigated by Atomistic Molecular Dynamics Simulations." *Molecular Simulation* 41(13):1110–21.

Cohen Stuart, Martien A., Bas Hofs, Ilja K. Voets, and Arie de Keizer. 2005. "Assembly of Polyelectrolyte-Containing Block Copolymers in Aqueous Media." *Current Opinion in Colloid & Interface Science* 10(1):30–36.

Coimbra, P., P. Ferreira, H. C. de Sousa, P. Batista, M. A. Rodrigues, I. J. Correia, and M. H. Gil. 2011. "Preparation and Chemical and Biological Characterization of a Pectin/Chitosan Polyelectrolyte Complex Scaffold for Possible Bone Tissue Engineering Applications." *International Journal of Biological Macromolecules* 48(1):112–18.

Csizmadia, Péter. 2019. "MarvinSketch and MarvinView: Molecule Applets for the World Wide Web."

Cunningham, Alexander J., Mattieu Robinson, Xavier Banquy, Jeanne Leblond, and X. X. Zhu. 2018. "Bile Acid-Based Drug Delivery Systems for Enhanced Doxorubicin Encapsulation: Comparing Hydrophobic and Ionic Interactions in Drug Loading and Release." *Molecular Pharmaceutics* 15(3):1266–76.

Dadsetan, Mahrokh, K. Efua Taylor, Chun Yong, Željko Bajzer, Lichun Lu, and Michael J. Yaszemski. 2013. "Controlled Release of Doxorubicin from PH-Responsive Microgels." *Acta Biomaterialia* 9(3):5438–46.

Dennington, Roy, Todd Keith, and John Millam. 2016. "Gaussview, Version 5." *Semichem Inc. , Shawnee Mission, KS.*

Dickson, Alex, Pratyush Tiwary, and Harish Vashisth. 2017. "Kinetics of Ligand Binding Through Advanced Computational Approaches: A Review." *Current Topics in Medicinal Chemistry* 17(23):2626–41.

Dobrynin, Andrey V. 2008. “Theory and Simulations of Charged Polymers: From Solution Properties to Polymeric Nanomaterials.” *Current Opinion in Colloid and Interface Science* 13(6):376–88.

Dobrynin, Andrey V. and Michael Rubinstein. 2005. “Theory of Polyelectrolytes in Solutions and at Surfaces.” *Progress in Polymer Science (Oxford)* 30(11):1049–1118.

Donnini, Serena, Florian Tegeler, Gerrit Groenhof, and Helmut Grubmüller. 2011. “Constant PH Molecular Dynamics in Explicit Solvent with λ-Dynamics.” *Journal of Chemical Theory and Computation* 7(6):1962–78.

Dror, Ron O., Robert M. Dirks, J. P. Grossman, Huafeng Xu, and David E. Shaw. 2012. “Biomolecular Simulation: A Computational Microscope for Molecular Biology.” *Annual Review of Biophysics* 41(1):429–52.

Eisenhaber, Frank, Philip Lijnzaad, Patrick Argos, Chris Sander, and Michael Scharf. 1995. “The Double Cubic Lattice Method: Efficient Approaches to Numerical Integration of Surface Area and Volume and to Dot Surface Contouring of Molecular Assemblies.” *Journal of Computational Chemistry* 16(3):273–84.

Everaers, Ralf, Sathish K. Sukumaran, Gary S. Grest, Carsten Svaneborg, Arvind Sivasubramanian, and Kurt Kremer. 2004. “Rheology and Microscopic Topology of Entangled Polymeric Liquids.” *Science* 303(5659):823–26.

Fedors, Robert F. 1974. “A Method for Estimating Both the Solubility Parameters and Molar Volumes of Liquids.” *Polymer Engineering and Science* 14(2):147–54.

Filion, L., M. Hermes, R. Ni, and M. Dijkstra. 2010. “Crystal Nucleation of Hard Spheres Using Molecular Dynamics, Umbrella Sampling, and Forward Flux Sampling: A Comparison of Simulation Techniques.” *Journal of Chemical Physics* 133(24).

Fredrickson, Glenn H., Venkat Ganesan, and François Drolet. 2002. “Field-Theoretic Computer Simulation Methods for Polymers and Complex Fluids.” *Macromolecules* 35(1):16–39.

Frenkel and Smit. 2002. *Understanding Molecular Simulation*. Vol. 11. AIP Publishing.

Ganesan, Aravindhan, Michelle L. Coote, and Khaled Barakat. 2017. “Molecular Dynamics-Driven Drug Discovery: Leaping Forward with Confidence.” *Drug Discovery Today* 22(2):249–69.

Ganesan, Venkat and Arthi Jayaraman. 2014. “Theory and Simulation Studies of Effective Interactions, Phase Behavior and Morphology in Polymer Nanocomposites.” *Soft Matter* 10(1):13–38.

Gao, Yi and Kenneth W. Olsen. 2013. “Molecular Dynamics of Drug Crystal Dissolution: Simulation of Acetaminophen Form I in Water.” *Molecular Pharmaceutics* 10(3):905–17.

Goel, Gaurav, Manoj V. Athawale, Shekhar Garde, and Thomas M. Truskett. 2008. “Attractions, Water Structure, and Thermodynamics of Hydrophobic Polymer Collapse.” *Journal of Physical Chemistry B* 112(42):13193–96.

Greiner, Maximilian, Ekaterina Elts, and Heiko Briesen. 2014a. “Insights into Pharmaceutical Nanocrystal Dissolution: A Molecular Dynamics Simulation Study on Aspirin.” *Molecular Pharmaceutics* 11(9):3009–16.

Greiner, Maximilian, Ekaterina Elts, and Heiko Briesen. 2014b. “Insights into Pharmaceutical Nanocrystal Dissolution: A Molecular Dynamics Simulation Study on Aspirin.” *Molecular Pharmaceutics* 11(9):3009–16.

Gubbins, K. E. and J. D. Moore. 2010. “Molecular Modeling of Mater: Impact and Prospects in Engineering.” *Industrial & Engineering Chemistry Research* 49(7):3026–46.

Gucht, Jasper van der, Evan Spruijt, Marc Lemmers, and Martien A. Cohen Stuart. 2011. “Polyelectrolyte Complexes: Bulk Phases and Colloidal Systems.” *Journal of Colloid and Interface Science* 361(2):407–22.

Guo, X. D., L. J. Zhang, Z. M. Wu, and Y. Qian. 2010. “Dissipative Particle Dynamics Studies on Microstructure of PH-Sensitive Micelles for Sustained Drug Delivery.” *Macromolecules* 43(18):7839–44.

Guo, Xiaoxia, Jianhua Fang, Tatsuya Watari, Kazuhiro Tanaka, Hidetoshi Kita, and Ken Ichi Okamoto. 2002. “Novel Sulfonated Polyimides as Polyelectrolytes for Fuel Cell Application. 2. Synthesis and Proton Conductivity of Polyimides from 9,9-Bis(4-Aminophenyl)Fluorene-2,7-Disulfonic Acid.” *Macromolecules* 35(17):6707–13.

Gupta, Jasmine, Cletus Nunes, Shyam Vyas, and Sriramakamal Jonnalagadda. 2011. “Prediction of Solubility Parameters and Miscibility of Pharmaceutical Compounds by Molecular Dynamics Simulations.” *Journal of Physical Chemistry B* 115(9):2014–23.

Hamer, Matthew J., Balaji V. S. Iyer, Victor V. Yashin, Tomasz Kowalewski, Krzysztof Matyjaszewski, and Anna C. Balazs. 2014. “Modeling Polymer Grafted Nanoparticle Networks Reinforced by High-Strength Chains.” *Soft Matter* 10:1374–83.

Hancock, B. 1997. “The Use of Solubility Parameters in Pharmaceutical Dosage Form Design.” *International Journal of Pharmaceutics* 148(1):1–21.

Hansen, Charles M. 2007. *Hansen Solubility Parameters: A User’s Handbook*. 2nd ed. Boca Raton, Florida: CRC press.

Hoare, Todd R. and Daniel S. Kohane. 2008. “Hydrogels in Drug Delivery: Progress and Challenges.” *Polymer*.

Hoda, Nazish and Ronald G. Larson. 2009. “Explicit- and Implicit-Solvent Molecular Dynamics Simulations of Complex Formation between Polycations and Polyanions.” *Macromolecules* 42(22):8851–63.

Hoffman, Allan S. 2013. *Applications of “Smart Polymers” as Biomaterials*.

Holm, C., J. F. Joanny, K. Kremer, R. R. Netz, P. Reineker, C. Seidel, T. A. Vilgis, and R. G. Winkler. 2004. “Polyelectrolyte Theory.” *Advances in Polymer Science* 166:3–17.

Hoven, Corey V., Andres Garcia, Guillermo C. Bazan, and Thuc Quyen Nguyen. 2008. “Recent Applications of Conjugated Polyelectrolytes in Optoelectronic Devices.” *Advanced Materials* 20(20):3793–3810.

Hsiao, Kai Wen, Charles M. Schroeder, and Charles E. Sing. 2016. “Ring Polymer Dynamics Are Governed by a Coupling between Architecture and Hydrodynamic Interactions.” *Macromolecules* 49(5):1961–71.

Hsu, David D., Wenjie Xia, Steven G. Arturo, and Sinan Keten. 2014. “Systematic Method for Thermomechanically Consistent Coarse-Graining: A Universal Model for Methacrylate-Based Polymers.” *Journal of Chemical Theory and Computation* 10(6):2514–27.

Huang, Weili, Sau Lawrence Lee, and Lawrence X. Yu. 2009. “Mechanistic Approaches to Predicting Oral Drug Absorption.” *The AAPS Journal* 11(2):217–24.

Huang, Wenjun, Indranil S. Dalal, and Ronald G. Larson. 2014. “Analysis of Solvation and Gelation Behavior of Methylcellulose Using Atomistic Molecular Dynamics Simulations.” *Journal of Physical Chemistry B* 118(48):13992–8.

Huang, Wenjun, Taraknath Mandal, and Ronald G. Larson. 2017. “Computational Modeling of Hydroxypropyl-Methylcellulose Acetate Succinate (HPMCAS) and Phenytoin Interactions: A Systematic Coarse-Graining Approach.” *Molecular Pharmaceutics* 14(3):733–45.

Huang, Wenjun, Rahul Ramesh, Prateek K. Jha, and Ronald G. Larson. 2016a. “A Systematic Coarse-Grained Model for Methylcellulose Polymers: Spontaneous Ring Formation at Elevated Temperature.” *Macromolecules* 49(4):1490–1503.

Huang, Wenjun, Rahul Ramesh, Prateek K. Jha, and Ronald G. Larson. 2016b. “A Systematic Coarse-Grained Model for Methylcellulose Polymers: Spontaneous Ring Formation at Elevated Temperature.” *Macromolecules* acs.macromol.5b02373.

Huynh, Loan, Justin Grant, Jean Christophe Leroux, Pascal Delmas, and Christine Allen. 2008. “Predicting the Solubility of the Anti-Cancer Agent Docetaxel in Small Molecule Excipients Using Computational Methods.” *Pharmaceutical Research* 25(1):147–57.

Iyer, Balaji V. S., Ashish K. Lele, and Sachin Shanbhag. 2007. “What Is the Size of a Ring Polymer in a Ring-Linear Blend?” *Macromolecules* 40(16):5995–6000.

Izvekov, Sergei and Gregory A. Voth. 2005. “A Multiscale Coarse-Graining Method for Biomolecular Systems.” *Journal of Physical Chemistry B* 109(7):2469–73.

Jämbeck, Joakim P. M., Emma S. E. Eriksson, Aatto Laaksonen, Alexander P. Lyubartsev, and Leif A. Eriksson. 2014. “Molecular Dynamics Studies of Liposomes as Carriers for Photosensitizing Drugs: Development, Validation, and Simulations with a Coarse-Grained Model.” *Journal of Chemical Theory and Computation* 10(1):5–13.

Jha, Prateek K., Priyanka S. Desai, Jingyi Li, and Ronald G. Larson. 2014. “PH and Salt Effects on the Associative Phase Separation of Oppositely Charged Polyelectrolytes.” *Polymers* 6(5):1414–36.

Jha, Prateek K., Vladimir Kuzovkov, and Monica Olvera de la Cruz. 2012a. “Dynamic Self-Assembly of Photo-Switchable Nanoparticles.” *Soft Matter* 8(1):227–34.

Jha, Prateek K., Vladimir Kuzovkov, and Monica Olvera de la Cruz. 2012b. “Kinetic Monte Carlo Simulations of Flow-Assisted Polymerization.” *ACS Macro Letters* 1(12):1393–97.

Jha, Prateek K. and Ronald G. Larson. 2014. “Assessing the Efficiency of Polymeric Excipients by Atomistic Molecular Dynamics Simulations.” *Molecular Pharmaceutics* 11(5):1676–86.

Jorgensen, William L. 1989. “Free Energy Calculations: A Breakthrough for Modeling Organic Chemistry in Solution.” *Accounts of Chemical Research* 22(5):184–89.

Jorgensen, William L. 2009. “Effcient Drug Lead Discovery and Optimization.” *Accounts of Chemical Research* 42(6):724–33.

Kanamala, Manju, William R. Wilson, Mimi Yang, Brian D. Palmer, and Zimei Wu. 2016. “Mechanisms and Biomaterials in PH-Responsive Tumour Targeted Drug Delivery: A Review.” *Biomaterials* 85:152–67.

Kataoka, Kazunori, Atsushi Harada, and Yukio Nagasaki. 2012. “Block Copolymer Micelles for Drug Delivery: Design, Characterization and Biological Significance.” *Advanced Drug Delivery Reviews*.

Katiyar, Ratna S. and Prateek K. Jha. 2018. “Molecular Insights into the Effects of Media-Drug and Carrier-Drug Interactions on PH-Responsive Drug Carriers.” *Molecular Pharmaceutics* 15(6):2479–83.

Kim, Jong Oh, Alexander V. Kabanov, and Tatiana K. Bronich. 2009. “Polymer Micelles with Cross-Linked Polyanion Core for Delivery of a Cationic Drug Doxorubicin.” *Journal of Controlled Release*.

Kizilay, Ebru, A. Basak Kayitmazer, and Paul L. Dubin. 2011. “Complexation and Coacervation of Polyelectrolytes with Oppositely Charged Colloids.” *Advances in Colloid and Interface Science* 167(1–2):24–37.

Kocak, G., C. Tuncer, and V. Bütün. 2017. “PH-Responsive Polymers.” *Polym. Chem.* 8(1):144–76.

Kollman, Peter. 1993. “Free Energy Calculations: Applications to Chemical and Biochemical Phenomena.” *Chemical Reviews* 93(7):2395–2417.

Krarup, Lene Hjorth, Inge thager Christensen, Lars Hovgaad, and Sven Frokjaer. 1998. “Predicting Drug Absorption from Molecular Surface Properties Based on Molecular Dynamics Simulations.” *Pharmacetical Research* 15(7):972–78.

Van Krevelen, D. W. and K. Te Nijenhuis. 2009. *Limiting Viscosity Number (Intrinsic Viscosity) and Related Properties of Very Dilute Solutions*.

Kudlay, Alexander, Alexander V. Ermoshkin, and Monica Olvera De La Cruz. 2004. “Complexation of Oppositely Charged Polyelectrolytes: Effect of Ion Pair Formation.” *Macromolecules* 37(24):9231–41.

Kudlay, Alexander and Monica Olvera de la Cruz. 2004. “Precipitation of Oppositely Charged Polyelectrolytes in Salt Solutions.” *Journal of Chemical Physics* 120(1):404–12.

Kundagrami, Arindam and M. Muthukumar. 2008. “Theory of Competitive Counterion Adsorption on Flexible Polyelectrolytes: Divalent Salts.” *Journal of Chemical Physics* 128(24):244901.

de la Cruz, M. O., L. Belloni, M. Delsanti, J. P. Dalbiez, O. Spalla, and M. Drifford. 1995. “Precipitation of Highly-Charged Polyelectrolyte Solutions in the Presence of Multivalent Salts.” *J. Chem. Phys.* 103(October):5781–91.

Laguecir, Abohachem, Serge Ulrich, Jérôme Labille, Nicolas Fatin-Rouge, Serge Stoll, and Jacques Buffle. 2006. “Size and PH Effect on Electrical and Conformational Behavior of Poly(Acrylic Acid): Simulation and Experiment.” *European Polymer Journal* 42(5):1135–44.

Larson, Ronald, Prateek K. Jha, Robert Schmitt, and William Porter III. 2014. “Methods, Systems, and Devices for Designing Molecules.”

Leach, Andrew R. 2001. *Molecular Modelling: Principles and Applications*. 2nd ed. Essex, UK: Pearson Education Limited.

Lee, Anthony, Christopher Yau, Michael B. Giles, Arnaud Doucet, and Christopher C. Holmes. 2010. “On the Utility of Graphics Cards to Perform Massively Parallel Simulation of Advanced Monte Carlo Methods.” *Journal of Computational and Graphical Statistics* 19(4):769–89.

Liang, Lijun, Jia Wei Shen, and Qi Wang. 2017. “Molecular Dynamics Study on DNA Nanotubes as Drug Delivery Vehicle for Anticancer Drugs.” *Colloids and Surfaces B: Biointerfaces* 153:168–73.

Liao, Qi, Andrey V. Dobrynin, and Michael Rubinstein. 2003. “Molecular Dynamics Simulations of Polyelectrolyte Solutions: Nonuniform Stretching of Chains and Scaling Behavior.” *Macromolecules* 36:3386–98.

Lindahl, Erik, Pär Bjelkmar, Per Larsson, Michel A. Cuendet, and Berk Hess. 2010. “Implementation of the Charmm Force Field in GROMACS: Analysis of Protein Stability Effects from Correction Maps, Virtual Interaction Sites, and Water Models.” *Journal of Chemical Theory and Computation* 6(2):459–66.

Lipinski, Christopher A., Franco Lombardo, Beryl W. Dominy, and Paul J. Feeney. 2012. “Experimental and Computational Approaches to Estimate Solubility and Permeability in Drug Discovery and Development Settings I.” *Advanced Drug Delivery Reviews* 64:4–17.

Liu, S. and M. Muthukumar. 2002. “Langevin Dynamics Simulation of Counterion Distribution around Isolated Flexible Polyelectrolyte Chains.” *The Journal of Chemical Physics* 116(22):9975.

Liu, Xuewei, Danfeng Shi, Shuangyan Zhou, Hongli Liu, Huanxiang Liu, and Xiaojun Yao. 2018. “Molecular Dynamics Simulations and Novel Drug Discovery.” *Expert Opinion on Drug Discovery* 13(1):23–37.

Liu, Yi, Vyacheslav S. Bryantsev, Mamadou S. Diallo, and William A. Goddard III. 2009. “PAMAM Dendrimers Undergo PH Responsive Conformational Changes without Swelling.” *Journal of American Chemical Society Communications* 131:2798–99.

Löbenberg, Raimar and Gordon L. Amidon. 2000. “Modern Bioavailability, Bioequivalence and Biopharmaceutics Classification System. New Scientific Approaches to International Regulatory Standards.” *European Journal of Pharmaceutics and Biopharmaceutics* 50(1):3–12.

Lu, Xue mei, Bing Yuan, Xian ren Zhang, Kai Yang, and Yu qiang Ma. 2017. “Molecular Modeling of Transmembrane Delivery of Paclitaxel by Shock Waves with Nanobubbles.” *Applied Physics Letters* 110(2).

Luo, Zhonglin and Jianwen Jiang. 2012a. “PH-Sensitive Drug Loading/Releasing in Amphiphilic Copolymer PAE-PEG: Integrating Molecular Dynamics and Dissipative Particle Dynamics Simulations.” *Journal of Controlled Release* 162(1):185–93.

Luo, Zhonglin and Jianwen Jiang. 2012b. “PH-Sensitive Drug Loading/Releasing in Amphiphilic Copolymer PAE-PEG: Integrating Molecular Dynamics and Dissipative Particle Dynamics Simulations.” *Journal of Controlled Release* 162(1):185–93.

Luzar, Alenka and David Chandler. 1993. “Structure and Hydrogen Bond Dynamics of Water–Dimethyl Sulfoxide Mixtures by Computer Simulations.” *The Journal of Chemical Physics* 98(10):8160–73.

Mahdavi, Mina, Farzin Rahmani, and Sasan Nouranian. 2016. “Molecular Simulation of PH-Dependent Diffusion, Loading, and Release of Doxorubicin in Graphene and Graphene Oxide Drug Delivery Systems.” *J. Mater. Chem. B* 4(46):7441–51.

Maiti, Prabal K., Youyong Li, Tahir Cagin, and William A. Goddard. 2009. “Structure of Polyamidoamide Dendrimers up to Limiting Generations: A Mesoscale Description.” *Journal of Chemical Physics* 130(14).

Malani, Ateeque, K. G. Ayappa, and Sohail Murad. 2009. “Influence of Hydrophilic Surface Specificity on the Structural Properties of Confined Water.” *Journal of Physical Chemistry B* 113(42):13825–39.

Manallack, David T., Richard J. Prankerd, Elizabeth Yuriev, Tudor I. Oprea, and David K. Chalmers. 2013. “The Significance of Acid/Base Properties in Drug Discovery.” *Chem. Soc. Rev.* 42(2):485–96.

Mandal, Taraknath, Ryan L. Marson, and Ronald G. Larson. 2016. “Coarse-Grained Modeling of Crystal Growth and Polymorphism of a Model Pharmaceutical Molecule.” *Soft Matter* 12(39):8246–55.

Manga, Ramya D. and Prateek K. Jha. 2017. “Mathematical Models for Controlled Drug Release Through PH-Responsive Polymeric Hydrogels.” *Journal of Pharmaceutical Sciences* 106(2):629–38.

Manning, Gerald S. 1969. “Limiting Laws and Counterion Condensation in Polyelectrolyte Solutions I. Colligative Properties.” *The Journal of Chemical Physics* 51(3):924.

Manning, Gerald S. 1969. “Limiting Laws and Counterion Condensation in Polyelectroyte Solutions. I. Colligative Properties.” *Journal of Chemical Physics* 51(3):924–33.

Marques, Margareth R. C., Raimar Loebenberg, and May Almukainzi. 2011. “Simulated Biological Fluids with Possible Application in Dissolution Testing.” *Dissolution Technologies* 18(3):15–28.

Marrink, Siewert J., H. Jelger Risselada, Serge Yefimov, D. Peter Tieleman, and Alex H. De Vries. 2007. “The MARTINI Force Field: Coarse Grained Model for Biomolecular Simulations.” *Journal of Physical Chemistry B* 111(27):7812–24.

Marsac, Patrick J., Sheri L. Shamblin, and Lynne S. Taylor. 2006. “Theoretical and Practical Approaches for Prediction of Drug–Polymer Miscibility and Solubility.” *Pharmaceutical Research* 23(10):2417–26.

Martínez, Lizbeth, Rafael Villalobos, Marisol Sánchez, Jeny Cruz, Adriana Ganem, and Luz María Melgoza. 2009. “Monte Carlo Simulations for the Study of Drug Release from Cylindrical Matrix Systems with an Inert Nucleus.” *International Journal of Pharmaceutics* 369(1–2):38–46.

Melchior, Andrea, Marilena Tolazzi, José Manuel Martínez, Rafael R. Pappalardo, and Enrique Sánchez Marcos. 2015. “Hydration of Two Cisplatin Aqua-Derivatives Studied by Quantum Mechanics and Molecular Dynamics Simulations.” *Journal of Chemical Theory and Computation* 11(4):1735–44.

Merz, Kenneth M. 2015. “Using Quantum Mechanical Approaches to Study Biological Systems.”

Meunier, M., A. Goupil, and P. Lienard. 2017. “Predicting Drug Loading in PLA-PEG Nanoparticles.” *International Journal of Pharmaceutics* 526(1–2):157–66.

Min, Sa Hoon, Sang Kyu Kwak, and Byeong-Su Kim. 2015. “Atomistic Simulation for Coil-to-Globule Transition of Poly(2-Dimethylaminoethyl Methacrylate).” *Soft Matter* 11(12):2423–33.

Missner, Andreas and Peter Pohl. 2009. “110 Years of the Meyer-Overton Rule: Predicting Membrane Permeability of Gases and Other Small Compounds.” *ChemPhysChem* 10(9–10):1405–14.

Moghadam, Soroush and Ronald G. Larson. 2017. “Assessing the Efficacy of Poly(N -Isopropylacrylamide) for Drug Delivery Applications Using Molecular Dynamics Simulations.” *Molecular Pharmaceutics* 14(2):478–91.

Mohanambe, L. and S. Vasudevan. 2005. “Anionic Clays Containing Anti-Inflammatory Drug Molecules : Comparison of Molecular Dynamics Simulation and Measurements.” *Journal of Physical Chemistry B* 109(32):15651–58.

Morrow, Brian H., Gregory F. Payne, and Jana Shen. 2015. “PH-Responsive Self-Assembly of Polysaccharide through a Rugged Energy Landscape.” *Journal of the American Chemical Society* 137(40):13024–30.

Mucs, Daniel and Richard A. Bryce. 2013. “The Application of Quantum Mechanics in Structure-Based Drug Design.” *Expert Opinion on Drug Discovery* 8(3):263–76.

Müller-Plathe, Florian. 2002. “Coarse-Graining in Polymer Simulation: From the Atomistic to the Mesoscopic Scale and Back.” *ChemPhysChem* 3(9):754–69.

Mura, Simona, Julien Nicolas, and Patrick Couvreur. 2013. “Stimuli-Responsive Nanocarriers for Drug Delivery.” *Nature Materials* 12(11):991–1003.

Muthukumar, M. 2004. “Theory of Counter-Ion Condensation on Flexible Polyelectrolytes: Adsorption Mechanism.” *The Journal of Chemical Physics* 120(19):9343.

Nič, Miloslav, Jiří Jirát, Bedřich Košata, Aubrey Jenkins, and Alan McNaught, eds. 2009. *IUPAC Compendium of Chemical Terminology*. Research Triagle Park, NC: IUPAC.

Nie, Shu Yu, Wen Jing Lin, Na Yao, Xin Dong Guo, and Li Juan Zhang. 2014. “Drug Release from PH-Sensitive Polymeric Micelles with Different Drug Distributions: Insight from Coarse-Grained Simulations.” *ACS Applied Materials & Interfaces* 6(20):17668–78.

Paloncýová, Markéta, Karel Berka, and Michal Otyepka. 2013. “Molecular Insight into Affinities of Drugs and Their Metabolites to Lipid Bilayers.” *The Journal of Physical Chemistry B* 117(8):2403–10.

Pan, Albert C., David W. Borhani, Ron O. Dror, and David E. Shaw. 2013. “Molecular Determinants of Drug–Receptor Binding Kinetics.” *Drug Discovery Today* 18(13–14):667–73.

Panagiotopoulos, Athanassios Z. 1987. “Direct Determination of Phase Coexistence Properties of Fluids by Monte Carlo Simulation in a New Ensemble.” *Molecular Physics* 61(4):813–26.

Panyukov, Sergei and Yitzhak Rabin. 1996. “Statistical Physics of Polymer Solutions.” *Physics Report* 269:1–131.

Patel, Sarthak K., Afsaneh Lavasanifar, and Phillip Choi. 2010. “Biomaterials Molecular Dynamics Study of the Encapsulation Capability of a PCL – PEO Based Block Copolymer for Hydrophobic Drugs with Different Spatial Distributions of Hydrogen Bond Donors and Acceptors." *Biomaterials* 31(7):1780–86.

Patel, Sarthak, Afsaneh Lavasanifar, and Phillip Choi. 2008. "Application of Molecular Dynamics Simulation To Predict the Compatability between Water-Insoluble Drugs and Self-Associating Poly(Ethylene Oxide)- *b* -Poly(ε-Caprolactone) Block Copolymers." *Biomacromolecules* 9(11):3014–23.

Patra, Tarak K. and Jayant K. Singh. 2013. "Coarse-Grain Molecular Dynamics Simulations of Nanoparticle-Polymer Melt: Dispersion vs. Agglomeration." *Journal of Chemical Physics* 138(14).

Peppas, Nicholas A. and Balaji Narasimhan. 2014. "Mathematical Models in Drug Delivery: How Modeling Has Shaped the Way We Design New Drug Delivery Systems." *Journal of Controlled Release* 190:75–81.

Peter, Christine and Kurt Kremer. 2009. "Multiscale Simulation of Soft Matter Systems – from the Atomistic to the Coarse-Grained Level and Back." *Soft Matter* 5(22):4357.

Petropoulos, John H., Kyriaki G. Papadokostaki, and Merope Sanopoulou. 2012. "Higuchi's Equation and beyond: Overview of the Formulation and Application of a Generalized Model of Drug Release from Polymeric Matrices." *International Journal of Pharmaceutics* 437(1–2):178–91.

Peyratout, Claire S. and Lars Dahne. 2004. "Tailor-Made Polyelectrolyte Microcapsules: From Multilayers to Smart Containers." *Angewandte Chemie - International Edition* 43(29):3762–83.

Pogodin, Sergey, Marco Werner, Jens-Uwe Sommer, and Vladimir A. Baulin. 2012. "Nanoparticle-Induced Permeability of Lipid Membranes." *ACS Nano* 6(12):10555–61.

Praprotnik, Matej, Luigi Delle Site, and Kurt Kremer. 2008. "Multiscale Simulation of Soft Matter: From Scale Bridging to Adaptive Resolution." *Annual Review of Physical Chemistry* 59(1):545–71.

Prates Ramalho, J. P., P. Gkeka, and L. Sarkisov. 2011. "Structure and Phase Transformations of DPPC Lipid Bilayers in the Presence of Nanoparticles: Insights from Coarse-Grained Molecular Dynamics Simulations." *Langmuir* 27(7):3723–30.

Priftis, Dimitrios and Matthew Tirrell. 2012. "Phase Behaviour and Complex Coacervation of

Aqueous Polypeptide Solutions." *Soft Matter* 8(36):9396–9405.

Pronk, Sander, Szilárd Páll, Roland Schulz, Per Larsson, Pär Bjelkmar, Rossen Apostolov, Michael R. Shirts, Jeremy C. Smith, Peter M. Kasson, David Van Der Spoel, Berk Hess, and Erik Lindahl. 2013. "GROMACS 4.5: A High-Throughput and Highly Parallel Open Source Molecular Simulation Toolkit." *Bioinformatics* 29(7):845–54.

Qiu, Li Yan and You Han Bae. 2006. "Polymer Architecture and Drug Delivery." *Pharmaceutical Research* 23(1):1–30.

Radhakrishna, Mithun, Kush Basu, Yalin Liu, Rasmia Shamsi, Sarah L. Perry, and Charles E. Sing. 2017. "Molecular Connectivity and Correlation Effects on Polymer Coacervation." *Macromolecules* 50(7):3030–37.

Raha, K., M. B. Peters, B. Wang, N. Yu, A. M. Wollacott, L. M. Westerhoff, K. M. Merz Jr., and K. M. Merz Jr. 2007. "The Role of Quantum Mechanics in Structure-Based Drug Design." *Drug Discov Today* 12(17–18):725–31.

Reith, Dirk, Beate Müller, Florian Müller-Plathe, and Simone Wiegand. 2002. "How Does the Chain Extension of Poly (Acrylic Acid) Scale in Aqueous Solution? A Combined Study with Light Scattering and Computer Simulation." *The Journal of Chemical Physics* 116(20):9100.

Sachan, Vinay K., Aruna Devi, Ratna S. Katiyar, Rajaram K. Nagarale, and Prashant K. Bhattacharya. 2014. "Proton Transport Properties of Sulphanilic Acid Tethered Poly(Methyl Vinyl Ether-Alt-Maleic Anhydride)-PVA Blend Membranes." *European Polymer Journal* 56(56):45–58.

Schmaljohann, Dirk. 2006. "Thermo- and PH-Responsive Polymers in Drug Delivery." *Advanced Drug Delivery Reviews* 58(15):1655–70.

Sevilla, Francisco J. and Mario Sandoval. 2015. "Smoluchowski Diffusion Equation for Active Brownian Swimmers." *Physical Review E - Statistical, Nonlinear, and Soft Matter Physics* E 91:052150–59.

Shaw, David E., Jack C. Chao, Michael P. Eastwood, Joseph Gagliardo, J. P. Grossman, C. Richard Ho, Douglas J. Lerardi, István Kolossváry, John L. Klepeis, Timothy Layman, Christine McLeavey, Martin M. Deneroff, Mark A. Moraes, Rolf Mueller, Edward C. Priest, Yibing Shan, Jochen Spengler, Michael Theobald, Brian Towles, Stanley C. Wang, Ron O.

Dror, Jeffrey S. Kuskin, Richard H. Larson, John K. Salmon, Cliff Young, Brannon Batson, and Kevin J. Bowers. 2008. “Anton, a Special-Purpose Machine for Molecular Dynamics Simulation.” *Communications of the ACM* 51(7):91.

Shaw, Vincent S., Hossein Mohammadiarani, Harish Vashisth, and Richard R. Neubig. 2018. “Differential Protein Dynamics of Regulators of G-Protein Signaling: Role in Specificity of Small-Molecule Inhibitors.” *Journal of the American Chemical Society* 140(9):3454–60.

Siepmann, J. and N. A. Peppas. 2012. “Modeling of Drug Release from Delivery Systems Based on Hydroxypropyl Methylcellulose (HPMC).” *Advanced Drug Delivery Reviews* 64(SUPPL.):163–74.

Siepmann, Jörn Ilja and Daan Frenkel. 1992. “Configurational Bias Monte Carlo: A New Sampling Scheme for Flexible Chains.” *Molecular Physics* 75(1):59–70.

Siepmann, Juergen and Nicholas A. Peppas. 2011. “Higuchi Equation: Derivation, Applications, Use and Misuse.” *International Journal of Pharmaceutics* 418(1):6–12.

Siepmann, Juergen and Florence Siepmann. 2012. “Modeling of Diffusion Controlled Drug Delivery.” *Journal of Controlled Release* 161(2):351–62.

Sing, Charles E., Jos W. Zwanikken, and Monica Olvera de la Cruz. 2013a. “Effect of Ion-Ion Correlations on Polyelectrolyte Gel Collapse and Reentrant Swelling.” *Macromolecules* 46(12):5053–65.

Sing, Charles E., Jos W. Zwanikken, and Monica Olvera de la Cruz. 2013b. “Ion Correlation-Induced Phase Separation in Polyelectrolyte Blends.” *ACS Macro Letters* 2(11):1042–46.

Spruijt, Evan, Martien A. Cohen Stuart, and Jasper Van Der Gucht. 2013. “Linear Viscoelasticity of Polyelectrolyte Complex Coacervates.” *Macromolecules* 46(4):1633–41.

Steuperaert, Margo, Giuseppe Falvo D’Urso Labate, Charlotte Debbaut, Olivier De Wever, Christian Vanhove, Wim Ceelen, and Patrick Segers. 2017. “Mathematical Modeling of Intraperitoneal Drug Delivery: Simulation of Drug Distribution in a Single Tumor Nodule.” *Drug Delivery* 24(1):491–501.

Subashini, M., Padma V Devarajan, Ganeshchandra S. Sonavane, and Mukesh Doble. 2011. “Molecular Dynamics Simulation of Drug Uptake by Polymer.” *Journal of Molecular Modeling* 17(5):1141–47.

Sulatha, Muralidharan S. and Upendra Natarajan. 2011. “Origin of the Difference in Structural Behavior of Poly(Acrylic Acid) and Poly(Methacrylic Acid) in Aqueous Solution Discerned by Explicit-Solvent Explicit-Ion MD Simulations.” *Industrial and Engineering Chemistry Research* 50(21):11785–96.

Suter, Ulrich W. and Peter Neuenschwander. 2005. “Epimerization of Vinyl Polymers to Stereochemical Equilibrium. 2. Polypropylene.” *Macromolecules* 14(3):528–32.

Tang, Pei and Yan Xu. 2002. “Large-Scale Molecular Dynamics Simulations of General Anesthetic Effects on the Ion Channel in the Fully Hydrated Membrane: The Implication of Molecular Mechanisms of General Anesthesia.” *Proceedings of the National Academy of Sciences* 99(25):16035–40.

Teraoka, Iwao. 2002. *Polymer Solutions: An Introduction to Physical Properties*. New York, USA: John Wiley & Sons, Inc.

Thota, Naresh, Zhongqiao Hu, and Jianwen Jiang. 2015. “Ibuprofen Loading and Release in Amphiphilic Peptide FA32 and Its Derivatives: A Coarse-Grained Molecular Dynamics Simulation Study.” *Molecular Simulation* 7022(February):1–9.

Tian, Y., L. Bromberg, S. N. Lin, T. Alan Hatton, and Kam C. Tam. 2007. “Complexation and Release of Doxorubicin from Its Complexes with Pluronic P85-b-Poly(Acrylic Acid) Block Copolymers.” *Journal of Controlled Release* 121(3):137–45.

Tian, Yuan, Palaniwasmy Ravi, Lev Bromberg, T. Alan Hatton, and Kam C. Tam. 2007. “Synthesis and Aggregation Behavior of Pluronic F87/Poly(Acrylic Acid) Block Copolymer in the Presence of Doxorubicin.” *Langmuir* 23(5):2638–46.

Tildesley, D. J. 1995. “Molecular Simulation: A View from the Bond.” *Faraday Discussions* 100:C29.

Uhrich, K. E., S. M. Cannizzaro, R. S. Langer, and K. M. Shakesheff. 1999. “Polymeric Systems for Controlled Drug Release.” *Chemical Reviews* 99:3181–98.

Valleau, John P. and L. Kenneth Cohen. 1980. “Primitive Model Electrolytes. I. Grand Canonical Monte Carlo Computations.” *The Journal of Chemical Physics* 72(11):5935–41.

Vashisth, Harish. 2015. *Theoretical and Computational Studies of Peptides and Receptors of the Insulin Family*. Vol. 5.

De Vivo, Marco, Matteo Masetti, Giovanni Bottegoni, and Andrea Cavalli. 2016. “Role of Molecular Dynamics and Related Methods in Drug Discovery.” *Journal of Medicinal Chemistry* 59(9):4035–61.

Vlugt-Wensink, Karin D. F., Thijs J. H. Vlugt, Wim Jiskoot, Daan J. A. Crommelin, Ruud Verrijk, and Wim E. Hennink. 2006. “Modeling the Release of Proteins from Degrading Crosslinked Dextran Microspheres Using Kinetic Monte Carlo Simulations.” *Journal of Controlled Release* 111(1–2):117–27.

Walsh, M. R., C. A. Koh, E. D. Sloan, A. K. Sum, and D. T. Wu. 2009. “Microsecond Simulations of Spontaneous Methane Hydrate Nucleation and Growth.” *Science* 326(5956):1095–98.

Wang, Huanjie, Xiaowen Ren, and Fancui Meng. 2015. “Molecular Dynamics Simulation of Six β-Blocker Drugs Passing across POPC Bilayer.” *Molecular Simulation* 7022(June):1–8.

Wang, Q., T. Taniguchi, and G. H. Fredrickson. 2004. “Self-Consistent Field Theory of Polyelectrolyte Systems.” *Journal of Physical Chemistry B* 108(21):6733–44.

Warren, Dallas B., Dylan King, Hassan Benameur, Colin W. Pouton, and David K. Chalmers. 2013. “Glyceride Lipid Formulations: Molecular Dynamics Modeling of Phase Behavior during Dispersion and Molecular Interactions between Drugs and Excipients.” *Pharmaceutical Research* 30(12):3238–53.

Warren, Dallas B., Dylan King, Hassan Benameur, Colin W Pouton, and David K. Chalmers. 2013. “Glyceride Lipid Formulations: Molecular Dynamics Modeling of Phase Behavior during Dispersion and Molecular Interactions between Drugs and Excipients.” *Pharmaceutical Research* 30(12):3238–53.

Worth Longest, P. and Michael Hindle. 2010. “CFD Simulations of Enhanced Condensational Growth (ECG) Applied to Respiratory Drug Delivery with Comparisons to in Vitro Data.” *Journal of Aerosol Science* 41(8):805–20.

Xiang, Tian Xiang and Bradley D. Anderson. 2017. “Molecular Dynamics Simulation of Amorphous Hydroxypropylmethylcellulose and Its Mixtures With Felodipine and Water.” *Journal of Pharmaceutical Sciences* 106(3):803–16.

Yan, Qiliang and Juan J. de Pablo. 2003. “Monte Carlo Simulation of a Coarse-Grained Model of Polyelectrolyte Networks.” *Physical Review Letters* 91(July):018301.

Yeh, In Chul and Gerhard Hummer. 2004. "System-Size Dependence of Diffusion Coefficients and Viscosities from Molecular Dynamics Simulations with Periodic Boundary Conditions." *Journal of Physical Chemistry B* 108(40):15873–79.

Yousefpour, Abbas, Hamid Modarress, Fatemeh Goharpey, and Sepideh Amjad-iranagh. 2015. "Biochimica et Biophysica Acta Interaction of PEGylated Anti-Hypertensive Drugs , Amlodipine , Atenolol and Lisinopril with Lipid Bilayer Membrane : A Molecular Dynamics Simulation Study." *BBA - Biomembranes* 1848(8):1687–98.

Yu, Lawrence X., John R. Crison, and Gordon L. Amidon. 1996. "Compartmental Transit and Dispersion Model Analysis of Small Intestinal Transit Flow in Humans." *International Journal of Pharmaceutics* 140(1):111–18.

Yuriev, Elizabeth, Mark Agostino, and Paul A. Ramsland. 2011. "Challenges and Advances in Computational Docking: 2009 in Review." *Journal of Molecular Recognition* 24(2):149–64.

Zeng, H. M., K. I. Jacob, and V. Tikare. 2004. "Numerical Simulations of Crystal Growth in a Transdermal Drug Delivery System." *Journal of Crystal Growth* 262(1–4):602–11.

Zhang, L., F. X. Gu, J. M. Chan, A. Z. Wang, R. S. Langer, and O. C. Farokhzad. 2008. "Nanoparticles in Medicine: Therapeutic Applications and Developments." *Clinical Pharmacology and Therapeutics* 83(5):761–69.

Zhao, Hongtao and Amedeo Caflisch. 2015. "Molecular Dynamics in Drug Design." *European Journal of Medicinal Chemistry* 91:4–14.

Zhu, Wusheng, Francis S. Romanski, Sameer V. Dalvi, Rajesh N. Dave, and M. Silvina Tomassone. 2012. "Atomistic Simulations of Aqueous Griseofulvin Crystals in the Presence of Individual and Multiple Additives." *Chemical Engineering Science* 73(January 2016):218–30.

Zoete, Vincent, Michel A. Cuendet, Aurélien Grosdidier, and Olivier Michielin. 2011. "SwissParam: A Fast Force Field Generation Tool for Small Organic Molecules." *Journal of Computational Chemistry* 32(11):2359–68.